EXPLICIT AND IMPLICIT CALCULATIONS OF TURBULENT CAVITY FLOWS WITH AND WITHOUT YAW ANGLE

by

Guan-Wei Yen

B.E. June 1984, Aeronautical Engineering Department

National Cheng-Kung University, Taiwan, R.O.C.

MASTER OF SCIENCE

MECHANICAL ENGINEERING AND MECHANICS

OLD DOMINION UNIVERSITY

August, 1989

Approved by:

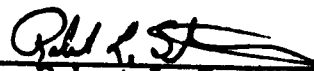_Oktay Baysal (Advisor)_

Oktay Baysal (Advisor)

Robert L. Ash

Robert L. Ash

Robert L. Stallings, Jr.

Robert L. Stallings, Jr.

ABSTRACT

EXPLICIT AND IMPLICIT CALCULATIONS OF TURBULENT CAVITY FLOWS WITH AND WITHOUT YAW ANGLE

Guan-Wei Yen
Old Dominion University
Advisor: Dr. Oktay Baysal

Computations have been performed to simulate turbulent supersonic flows past three-dimensional deep cavities with and without yaw. Simulation of these self-sustained oscillatory flows have been generated through time accurate solutions of the Reynolds averaged complete Navier-Stokes equations using two different schemes: (1) MacCormack, finite-difference, (2) implicit, upwind, finite-volume schemes. The second scheme, which is approximately 30% faster, is found to produce better time accurate results. The Reynolds stresses have been modeled, using the Baldwin-Lomax algebraic turbulence model with certain modifications. The computational results include instantaneous and time averaged flow properties everywhere in the computational domain. Time series analyses have been performed for the instantaneous pressure values on the cavity floor. The time averaged computational results show good agreement with the experimental data along the cavity floor and walls. When the yaw angle is nonzero, there is no longer a single length scale (length-to-depth ratio) for the flow, as is the case for zero yaw angle flow. The dominant directions and inclinations of the vortices are dramatically different for this nonsymmetric flow. The vortex shedding from the cavity into the mainstream flow is captured computationally. This phenomenon, which is due to the oscillation of the shear layer, is confirmed by the solutions of both schemes.

ACKNOWLEDGEMENTS

TABLE OF CONTENTS

iv

LIST OF TABLES

v

LIST OF FIGURES

LIST OF SYMBOLS

a	speed of sound
C_f	skin friction coefficient
C_p	pressure coefficient
C_v	specific heat at constant volume
D	depth of the cavity
E	total energy per unit volume
e	internal energy per unit volume
F	floor
FF	front face
FP1	front flat plate
FP2	rear flat plate
FSW	front side wall
f	frequency
F, G, H	inviscid flux vectors
F_v, G_v, H_v	viscous flux vectors
J	Jacobian matrix
K	coefficient of thermal conductivity
k	Von Karman's constant, 0.4
L	length of the cavity
M	Mach number

P	static pressure
P_e	pressure at edge of boundary
P_r	Prandtl number
q	heat flux
R	universal gas constant
R_e	Reynolds number
RF	rear face
RSW	rear side wall
SFP	side flat plate
SW	side wall
T	static temperature
t	time
t_c	characteristic time
X, Y, Z	cartesian coordinates
W	width of the cavity
y	normal distance to a wall

GREEK

δ	boundary layer thickness
τ	stress
ξ, η, ζ	curvilinear coordinates
μ_e	effective viscosity $(\mu_l + \mu_t)$
μ_i	eddy viscosity of inner region
μ_l	molecular viscosity
μ_o	eddy viscosity of outer region

μ_t	eddy viscosity
γ	ratio of specific heat
ω	magnitude of vorticity
ρ	density

SUBSCRIPTS AND SUPERSCRIPTS

n	time level
w	solid wall
cr	critical value
∞	free stream

OPERATORS

d	total derivative
∂	partial derivative

Chapter 1

BACKGROUND

1.1 Objectives

It is often inevitable to have a cavity on an aerodynamic configuration, such as, a weapons bay, a landing gear, or similar recessed areas. Carrying weapons internally in high speed fighter-bomber aircraft (e.g. B-1, FB-111) offers many benefits, such as, greater maneuverability, longer combat range, reduction of weapon and landing gear aerothermal heating problems, and reduction of radar detection signature. However, a cavity flow at high speed may be a source of flow instability. The presence of a cavity flow structure may cause large fluctuations of pressure and velocity, which generate strong acoustic waves. This may damage the aircraft structure, the weapon devices, and affect the avionics on board.

Earlier reports in the literature (e.g. refs. 1, 2) have provided descriptions of cavity flows. Many investigations, both experimental and computational, have been conducted to study the flowfield inside two and three-dimensional rectangular cavities. Some examples of viscous calculations of cavity flows are given in refs. 3 - 5. The objectives of this research effort are focused on further understanding of the cavity flow phenomenon for deep cavities, and to analyze the pressure fluctuations within deep cavities. Furthermore, it is aimed to provide:

1. valid computational solutions for deep cavity flows at supersonic speeds,

2. qualitative understanding of three-dimensional cavity flows through enhanced computational graphics,

1

3. valid computational solutions for flow past a cavity at yaw,

4. comparison of the solutions for cavity flows from two different numerical schemes (explicit, finite-difference, MacCormack scheme and implicit, finite-volume, upwind scheme),

5. a study of three-dimensional unsteady flow separation,

6. a comparison of time averaged and instantaneous properties of the flow solution obtained computationally with the experimental data.

A literature survey on cavity flows are given in the next two sections. The physics of cavity flows and their classification are given in Chapter 2. The governing equations and the corresponding boundary conditions are detailed in Chapter 3. The solution algorithms and the grid generations are discussed in Chapter 4. The results are discussed in Chapter 5, and conclusions and recommendations are given in Chapter 6.

1.2 Experimental Literature on Cavity Flows

Roshko [2] studied the time-averaged effects of flows over various cavities at low Mach numbers. Pressure coefficients at various points on the cavity walls and floor were measured and friction coefficients were calculated. For a deep cavity, a single vortex was seen to exist inside, and smaller secondary vortices were also observed at the corners of the cavity. For a shallow cavity, the shear layer was seen to be attached to the floor of the cavity enclosing vortices on either side. Roshko concluded that the increased drag due to the cavity stemmed from the stagnation pressure on the downstream cavity wall as the shear layer impinged on it. Karamcheti [1] performed an extensive study of the sound radiated by flows over rectangular cavities using a flat plate with a cavity of variable length mounted in a blow down tunnel. The Mach number was varied from 0.25 to 1.5. Schlieren and interferometer techniques

were used to visualize the acoustic fluctuations and to get quantitative measures of the decibel level and directionality of the radiated sound. The boundary layer was changed between laminar and turbulent regimes using the flat plate angle of attack and a trip wire, and its characteristics were measured using hot wire anemometry. He observed that below a minimum cavity length, the shear layer jumped across the cavity without impinging on the downstream wall or generating acoustic oscillations. Above this length, the wavelength of the oscillations was proportional to the cavity length. When the boundary layer was turbulent, several harmonics were observed. However, the peak amplitudes observed were considerably less than in the case of the laminar boundary layer.

MacDearmon [6] has presented the results of systematic variations of depth, span, and upstream and downstream lip radii on the flow characteristics in a rectangular cavity on a flat plate at a Mach number of 3.55. Plumbee et al. [7] studied the acoustic response of large cavities in flows of Mach number 0.2 to 5.0. Both discrete tones and broadband noise generated by the cavity flow were observed. Rapid fluctuations occurred in the separated boundary layer, and depending on flow conditions, both expansion waves and shocks were observed at the separation point near the cavity. The static pressure in the cavity increased with increasing cavity depth. The deep cavities would resonate primarily in the depth modes, while longer cavities would show lengthwise modes and random buffeting. The most significant drawback of his theory was that shear layer turbulence was considered to be the driving mechanism for periodic oscillations, contrary to the observations of Karamcheti [1] and others that the oscillations were much stronger when the shear layer was laminar as opposed to turbulent.

East [8] observed that deep cavity resonance appeared to result from simultaneous doubly-tuned amplification of shear layer unsteadiness by both the shear layer edge tone

and the cavity enclosure acting as an acoustic resonator. Three-dimensional effects due to variations in the transverse dimension of the cavity did not appear to alter the unsteady effects. Rossiter [9] performed wind tunnel tests on subsonic and transonic flows (0.4 < M < 1.2) over shallow cavities. Cavities of L/D >10 were found to generate   smooth broadband pressure fluctuation spectra, as opposed to cavities at L/D of 1 and 2, which generated dominant periodic fluctuations. Higher harmonics of the discrete tones were attributed to the distorted wave formes of the oscillations. High speed shadowgraph motion pictures showed that the shear layer rolled up into discrete vortices, shed periodically from cavity leading edge.

Spee [10] observed periodic inflow and outflow of air close to the trailing edge, and an accompanying lateral displacement of the shear layer. Continuous production of vorticity occurred at the leading edge, as opposed to discrete vortex shedding. The "captive vortex" or recirculation zone in the cavity was seen to grow and shrink periodically. Root-mean-square pressure fluctuations reached 40% of dynamic pressure, which was too large to be explained by the linear acoustic theory. At low Mach numbers, the acoustic source exhibited monopole behavior. The radiated sound waves were sinusoidal initially, later becoming sawtoothed as they propagated into the far field.

McGregor and White [11] measured the drag of rectangular cavities in supersonic and subsonic flow (0.3 < M < 3.0), they also provided schlieren pictures. The pressure wave generated by the impact of the vortex at the trailing edge went upstream, and another vortex was shed. The steady-state drag of the cavity was attributed to the impact pressure at the downstream wall. When resonance occurred, a 250% increase 1 drag was observed, which was attributed to the large deflection of the shear layer and resultant loss of momentum. Heller, Holmes, and Covert [12] conducted wind tunnel tests on cavities with L/D ratios of 4 to 7 over a Mach number

range from 0.8 to 3, obtaining spectra of pressure fluctuations inside the cavity and under the approaching boundary layer. They also observed stronger spectral peaks when the boundary layer was laminar. Pressure fluctuations were seen to be highest near the trailing edge, falling off inversely with distance towards the leading edge.

Stallings and Wilcox [13] have measured flow past various cavities to obtain cavity pressure distributions for a wide range of supersonic Mach number. The test Mach number were varied from 1 5 to 1.86 for cavity depths and widths from 0.5 to 2.5 inches and cavity lengths from 0.5 to 1.2 inches. These pressure distributions together with Schlieren photographs were used to define the critical values of cavity length to depth ratio $(L/D)_{cr}$ that separate deep cavity flows from shallow cavity flows. It was further observed that a large improvement in the correlation of measured cavity centerline pressure distribution for cavities of various depths were obtained when both the cavity width to depth (W/D) ratio and length to depth (L/D) ratio were held constant rather than L/D alone. Decreasing cavity width resulted in a reduction in $(L/D)_{cr}$. Three-dimensional effects in the form of large lateral pressure gradients occurred on the rear face of the cavities that had closed cavity flow fields.

Heller and Bliss [14] conducted wind tunnel tests on cavities of L/D ratios from 2.3 to 5.5 and over a Mach number range of 0.8 to 2.0. Detailed information on the normalized levels of the first three resonant modes in the cavity for a range of cavity L/D and free-stream Mach numbers were obtained. It was shown that the cavity temperature was close to the stagnation value with recovery factors between 0.8 and 0.95. Shaw [15] performed wind tunnel tests on a cavity model with variable length to depth ratio. The test Mach numbers were 1.5 to 2.86 and Reynolds numbers from 1.0 to 4.0 million/foot. The model was tested at two angles of attack, two yaw angles and two cavity widths. Acoustic data were obtained for almost all combinations of the

test parameters. Sound pressure levels as high as 165dB were measured. Reynolds number was shown to strongly affect excitation of specific resonant modes.

1.3 Literature on Prediction Methods for Cavity Flows

Weiss and Florsheim [16] modeled a low Reynolds number flow in a deep cavity, neglecting convection of vorticity, and obtained results showing steady, double-celled recirculating flow inside the cavity. Pan and Acrivos [17] used a relaxation technique to obtain creeping-flow solutions for rectangular cavities of L/D ratios 0.2 to 4. According to their results, the steady flow in a cavity at high Reynolds number consisted of a single core of uniform vorticity, with viscous effects confined to their shear layers near the boundaries. For infinitely deep cavities, the viscous and inertial forces would be comparable at all Reynolds numbers.

Mehta and Lavan [18] calculated the flow in a two-dimensional channel with a rectangular cavity in the lower wall and the upper wall moving at uniform velocity. They solved the Navier-Stokes equations for a laminar incompressible flow. O'Brien [19] studied closed streamlines associated with the channel flow over a cavity. The viscous Stokes flow in a rectangular cavity with parallel shear flow was calculated by a direct finite difference technique. Nallaswamy and Krishnaprasad [20] studied steady cavity flows at high Reynolds numbers ($0 < Re < 50,000$). Three fully viscous eddies were found inside the cavity, and obtained velocity, temperature, vorticity, and heat flux profiles inside the cavity.

Bilanin and Covert [21] assumed that shear layer instability as well as interaction between the shear layer and the cavity trailing edge were required to sustain discrete frequency oscillations. They modeled the shear layer as a vortex sheet excited at the leading edge by a periodic pressure pulse, and the pressure fluctuation at the trailing edge as an acoustic monopole. They obtained quantitatively correct acoustic mode shapes and possible excitation frequencies for shallow cavities for $0.8 < M < 3.0$.

Smith and Shaw [22] developed empirical prediction methods for modal frequencies, modal amplitudes, broadband amplitudes, L/D effects, Mach number effects, and longitudinal distribution of fluctuating pressures.

Block [23] studied the noise response of cavities of varying dimensions at subsonic speeds. She included the effect of the L/D ratio in Rossiter's model for oscillation frequencies, and the maximum amplitude. Her formula for the maximum-amplitude Mach number was of the form:

$$M = (1/K)(L/D)/ \{4n[1 + A (L/D)^B - [(L/D) + 0.514]\} \qquad (1.1)$$

where K is the real part of the wave number of the disturbance traveling downstream, n is the mode number, and A and B are empirical constants. Interactions between the depth and length modes were found.

Hardin and Mason [24] developed a potential flow model of two-dimensional cavity flow in which the shear layer was represented by discrete rectilinear vortices in order to predict and explain the broadband noise generation phenomenon. The spectra and directivity of the quadrupole noise source determined by their theory were found to compare well with observed results for real aircraft. Borland [25] solved the two-dimensional Euler equations for the time-dependent inviscid compressible flow over a cavity. He modeled the shear layer oscillation and used a piston at the rear bulkhead to simulate the mass addition and removal at the trailing edge of the cavity.

Hankey and Shang [26] analyzed pressure oscillations in an open cavity using the unsteady Navier-Stokes equations. With supersonic flow outside the cavity, the Mach number inside the cavity was found to be 0.5. The sound inside the cavity propagated upstream at about half the freestream velocity. The shear layer was seen to be unstable for low frequencies such that

$$1/(4\pi) > fK/U \qquad (1.2)$$

where K is the boundary layer thickness, and U the freestream velocity. Short cavities

whose lengths were less than $2\pi K$ would not resonate. Above $M=2.5$, no Rayleigh instability was found for the shear layer. Peak amplification occurred at half the cut-off frequency, so that higher harmonics could exist. The maximum intensity of pressure oscillations occurred at about $M=1$.

Brandeis [27] studied the effects of altering the length and aspect ratio of rectangular cavities on the development of the shear layer. He used an interactive method which adapted the compressible boundary-layer model for the flow within the cavity. His results showed the location of the stagnation points to be sensitive primarily to span variation. Shaw et al [28] modified Rossiter's formula to improve correlation with measured data for cylindrical and rectangular cavities over the range $0.4 < M < 1.2$. Pathasaraty and Cho [29] developed empirical design equations for the dimensions, frequencies, and root-mean-square pressure amplitudes of cylindrical aerodynamic whistles.

Baysal and Stallings [30] performed calculations for two dimensional cavities over an L/D range of 6,12, and 16 at a Mach number of 1.5, and compared the computational and experimental pressure data. An upwind, finite-volume scheme was used to solve the complete Navier-Stokes equations. Rizzeta [31] presented a numerical solution for the unsteady flow over a three-dimensional cavity at a freestream Mach number of 1.5 and Reynolds number of 1.5 million. The self sustained oscillatory motion within the cavity was generated numerically by integration of the time-dependent compressible three-dimensional Navier-Stokes equations. Comparisons with experimental data were made in terms of the mean static pressure and overall acoustic sound pressure levels within the cavity.

Baysal, Srinivasan, and Stallings [32] performed calculations on three-dimensional deep and shallow cavities of L/D= 6, and 16 for supersonic flow. They used the MacCormack scheme to solve time-dependent complete Navier-Stokes equations.

Comparisons with experimental data were made in terms of SPL (sound pressure level) and time-averaged pressure coefficients. Computational pressure fluctuations were transferred from time domain to frequency domain using the Fourier transformation.

Suhs and Jordan |33| used the Chimera scheme to divide the computational domain into two overlapping grid regions, then used an implicit algorithm to solve the thin-layer Navier-Stokes equations. Numerical computations were performed at Mach numbers of 0.74, 0.95 and 1.5, and L/D ratios of 4.5 and 9.9. They have added consideration of acoustic suppression device(saw tooth fence) into their code and got the computational sound pressure level results.

Baysal and Srinivasan [34] presented a computational investigation of subsonic and transonic flows past 3-D deep and transitional cavities. Computational simulations of these self induced oscillatory flows have been generated through time-accurate solutions of the Reynolds averaged full Navier-Stokes equations, using the explicit MacCormack scheme. The computational results, which are compared with the experimental data, include instantaneous and time averaged flow properties everywhere in the computational zone. Time series analyses have been performed for the instantaneous pressure values on the cavity floor.

Om [35] conducted a numerical study of cavity-flow phenomenon on a modified Boeing 767. A two-dimensional Navier-Stokes code was used to simulate the flow field. The code employed the explicit MacCormack scheme. The investigation was aimed at examining the unsteadiness of the shear layer and obtaining details of the flowfield. Cavity flow was simulated for two different cavity sizes as well as for two different ramp shapes. The computational results indicated that the shear layer stability depends very strongly on the shape of the aft ramp, and the effect of cavity size was negligible on the shear layer stability.

Baysal and Srinivasan [36] performed numerical simulations of supersonic turbulent flows by solving the Reynolds-averaged full Navier-Stokes equations by an implicit finite-volume method. Several examples of two dimensional solutions are given to illustrate the k-ε turbulence model for wall and free turbulent shear flows.

CHAPTER 2

PHYSICAL DESCRIPTION

2.1 Types of Cavity Flows

A cavity in a flat plate changes the flow field and causes a significant increase in the fluid drag. The flow structure within a rectangular cavity is complex, vortical, three-dimensional and unsteady. According to the ratio of the cavity length to depth, the cavity can be classified as deep, transitional and shallow [13] as illustrated in Fig.2.1. A deep cavity is one for which L/D is less than 10, and cavities with L/D greater 13 are called shallow. When L/D is between 10 and 13, it is called a transitional cavity.

For a shallow cavity(L/D > 13), the flow is likely to reattach on the bottom of the cavity and thus form two recirculating regions. For a deep cavity(L/D < 10), a single vortex is observed; usually somewhat downstream of the middle of the cavity. Small secondary vortices rotating counter to the main vortex have been observed near the front corners. In very deep cavities, a second vortex is likely to form below the first one, forming a double-celled structure [37]. The resonant mode frequencies or deep cavities have been observed to change considerably with L/D.

The general flow structure of a deep cavity is shown in Fig. 2.2. After the initial expansion of the flow into the cavity, a shear layer is formed between the high-speed external flow and the slower internal flow. The water table simulation study of the deep cavities by Heller and Bliss [14] showed that unsteady motion of the shear layer

11

leads to mass being pumped in and out at the cavity trailing edge. This effect generates forward travelling waves in the cavity that reflect from the front bulkhead and become rearward traveling waves. The shear layer is pulled continuously into and then pushed out of the cavity due to the pressure oscillations inside the cavity. When the cavity pressure is lower than the freestream pressure, the shear layer is deflected downwards pumping mass and momentum into the cavity. This ingested mass is slowed down by various dissipative processes within the cavity, therefore increasing the cavity pressure above the freestream pressure. The shear layer is then deflected out of the cavity by the excess pressure and mass is pumped out of the cavity with low momentum. This oscillatory process extracts additional freestream momentum during the cycle. A series of sketches which shows the stages of such a cycle are shown in Fig.2.3. The choice of a starting point for the cycle is arbitrary, and it is necessary to review the entire process to understand completely the conditions at the beginning.

2.2 Flow in a Deep Cavity

Cavities with L/D < 10 exhibit open cavity flow structure. In the external flow, the wave patterns at the leading and trailing edges of the cavity depend on shear layer positions. A supersonic flow past a cavity is shown in Fig. 2.4. High pressure ahead of the rear face within the cavity, venting into the low pressure region downstream of the front face, cause the shear layer to flow over the cavity. The pressure coefficients over the cavity floor are slightly positive and relatively constant with the exception of a small adverse pressure gradient ahead of the rear face, that is associated with the shear layer impinging on the outer edge of the rear face.

In Fig. 2.4(a), a separated shear layer is shown to approach and flow over the trailing edge. Thereafter, the shear layer deflects down, thus exposing the trailing edge to the free stream, which causes a shock front to occur at the trailing edge.

Simultaneously, the downward motion of the shear layer causes a pressure wave to appear in the corner region of the trailing-edge bulkhead and the floor. This pressure wave moves toward the leading edge. The pressure wave also causes the shear layer above to bend outward into the free stream. This outward bend causes a shock front to propagate, along with the pressure wave, in the upstream direction.

When the shear layer is above the trailing edge (Fig. 2.4b), there seems to be no significant external wave system as a downstream wave is arriving. It must be recalled that the shear layer disturbance associated with this wave moves at a subsonic speed relative to the external flow.

At the leading edge (Fig. 2.4c and d), as an upstream wave approaches the leading edge, the shear layer is bent downward and there is an expansion wave at the edge as well as the upstream traveling compression wave. After the upstream wave is reflected to become a downstream traveling wave, the external portion trails away since the downstream wave is subsonic relative to the external flow. At this time, the shear layer is deflected upward and a leading-edge oblique shock occurs. This sequence of occurrences can be compared with observed radiation pattern to arrive at Fig. 2.5 for supersonic flow.

2.3 Flow in a Shallow Cavity

The basic flow field in the shallow cavity can be divided into two regions. The first half of the flow behaves like the flow over a rearward facing step and the latter half is similar to that of forward facing step flow, as illustrated in Fig 2.1a.

In an example of "Breakaway Separation" (wherein separation occurs on convex corners even through there is a favorable pressure gradient), the upstream boundary layer is unable negotiate the sharp corner and leaves the wall at the corner, splitting into two regions: (1) a slow recirculating separated region near the base, (2) a free

shear layer that is swept downstream and reattaches to the cavity floor. As the flow meets the 90 degree turn at the front face, it undergoes a rapid expansion. The pressure within the separated and recirculation region falls much below the free stream pressure. This effect and the pressure of the side wall enhance the cross flow which in turn affects the flow separation characteristics in this region. The separated shear layer curves downward and impinges on the cavity floor. The boundary layer grows from the reattachment point up to a certain extent when the adverse pressure gradient from the rear face causes separation close to rear face.

2.4 Unsteadiness and Acoustics of Cavity Flows

There are two different type of pressure fluctuations that can occur within cavities, a random pressure fluctuation and a strong periodic pressure fluctuation. Karamcheti [1] found that the periodic pressure fluctuations are accompanied by strong acoustic radiation from the cavity. The frequency of these pressure fluctuations was found to increase with airspeed and decrease as the cavity length was increased. In very deep cavities ($L/D = 1$ and 2), the pressure fluctuations are mainly periodic but as the cavity depth is decreased, the fluctuations become random in character. For the shallow cavity ($L/D > 10$), the spectrum is smooth and covers a broad band of frequencies showing that the pressure fluctuations are random in character. As the depth of the cavity is increased, peaks occur in the spectra indicating that periodic pressure fluctuations are superimposed upon the random levels. The random component is seen in cavities where $L/D > 4$ and the periodic component dominate in cavities where $L/D < 4$ [63]. The random component is most intense near the rear wall of the cavity, but for very shallow cavities a local region of intense pressure fluctuations occurs where the flow reattaches to the floor of the cavity.

Bilanin and Covert [21] analyzed a model of the excitation mechanism suggested by Rossiter [9]. They treated the pressure fluctuation at the trailing edge as an acoustic monopole. As indicated in Chapter 1, the mass addition and removal process at the cavity trailing edge is caused by unsteady motion of the shear layer. This process produces a piston-like effect at the rear bulkhead [Fig. 2.6], which sets up the internal wave structure that forces the shear layer.

In flow visualization photographs, the shear layer has been observed to roll up into vortices that travel rearward and impinge on the cavity trailing edge, that would cause the cavity oscillation mechanism. In supersonic flow experiments, discrete vortices are not usually seen, but an amplifying sinusoidal motion of the shear layer traveling toward the trailing edge is often evident. Perturbations to the shear layer indicate a varying vorticity distribution along its length. The apparent traveling wave motion along the shear layer is a result of the dominant amplification of the downstream traveling wave in the cavity. Heller and Bliss [14] proposed that the shear layer which is subjected to forcing by the cavity internal wave structure would roll up into downstream traveling vortices. Thus, the appearance of discrete vortices on the cavity shear layer is completely consistent with the oscillation mechanism. They conclude that "vortex shedding" is a manifestation of the oscillation process, but it is not essential to the underlying mechanism. Fig.2.7 shows the feedback loop responsible for cavity oscillations.
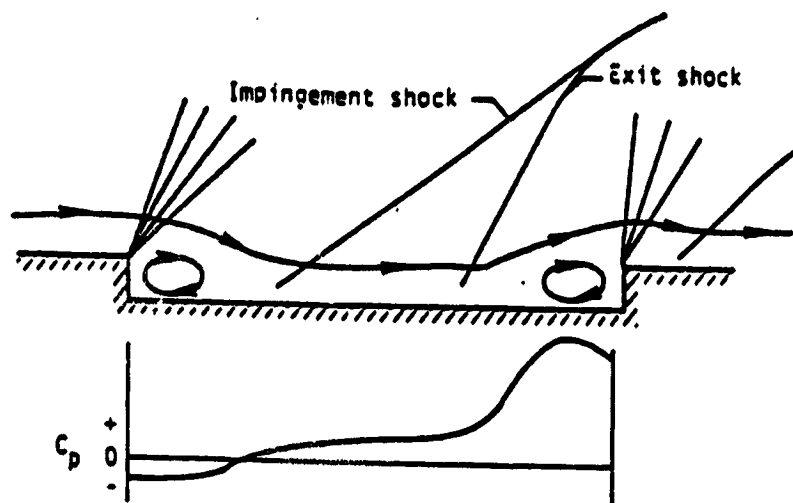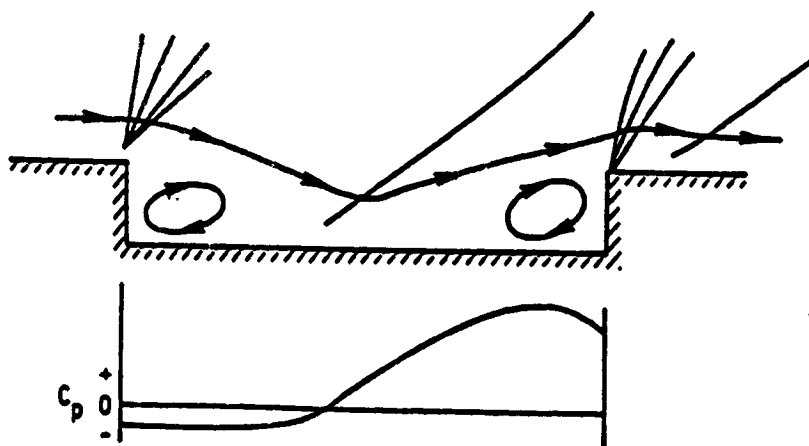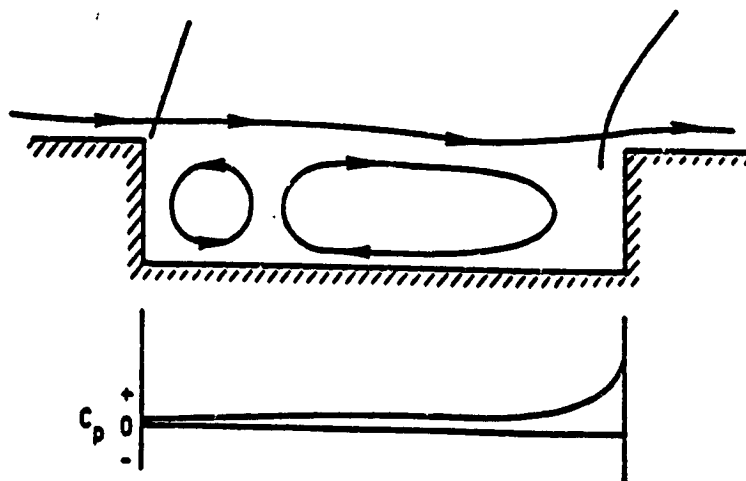
Fig. 2.1 Sketches of cavity flowfield models

δ :Boundary Layer Thickness

δs : Thickness of the Shear Layer

Δ : Shear Layer dips in and out distance

U^* : Shear Layer velocity
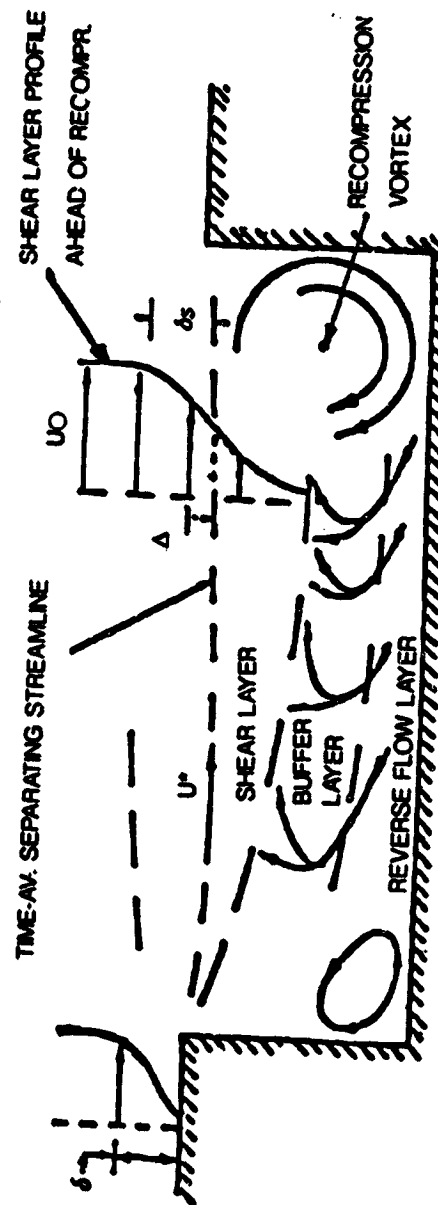
Fig. 2.2 Structure of the internal flow in a deep cavity
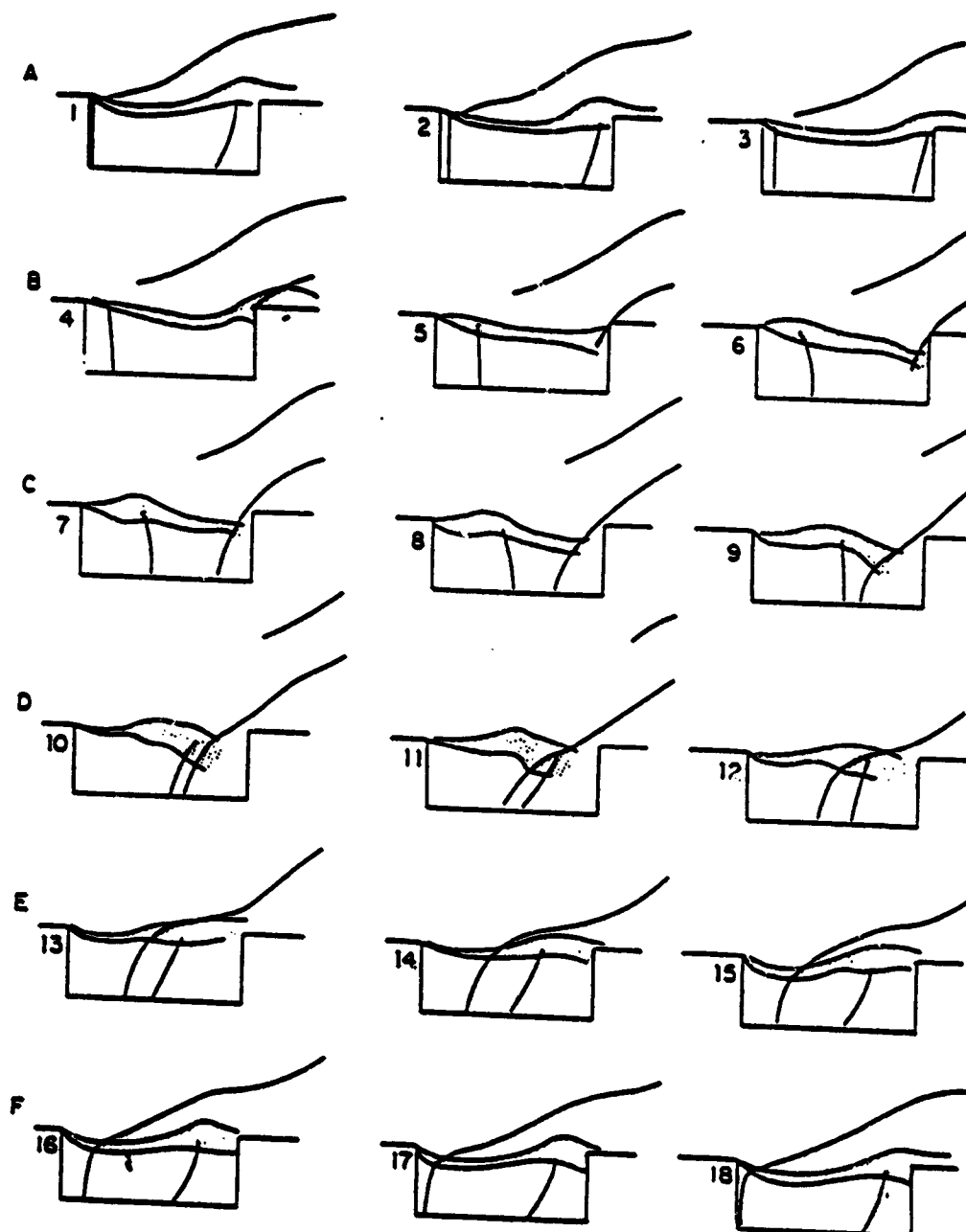
Fig.2.3 Typical pressure oscillation cycle.
        (3) Mass removal stops;
        (4) Mass addition starts;
        (12) Mass addition ends;
        (13) Mass removal starts.
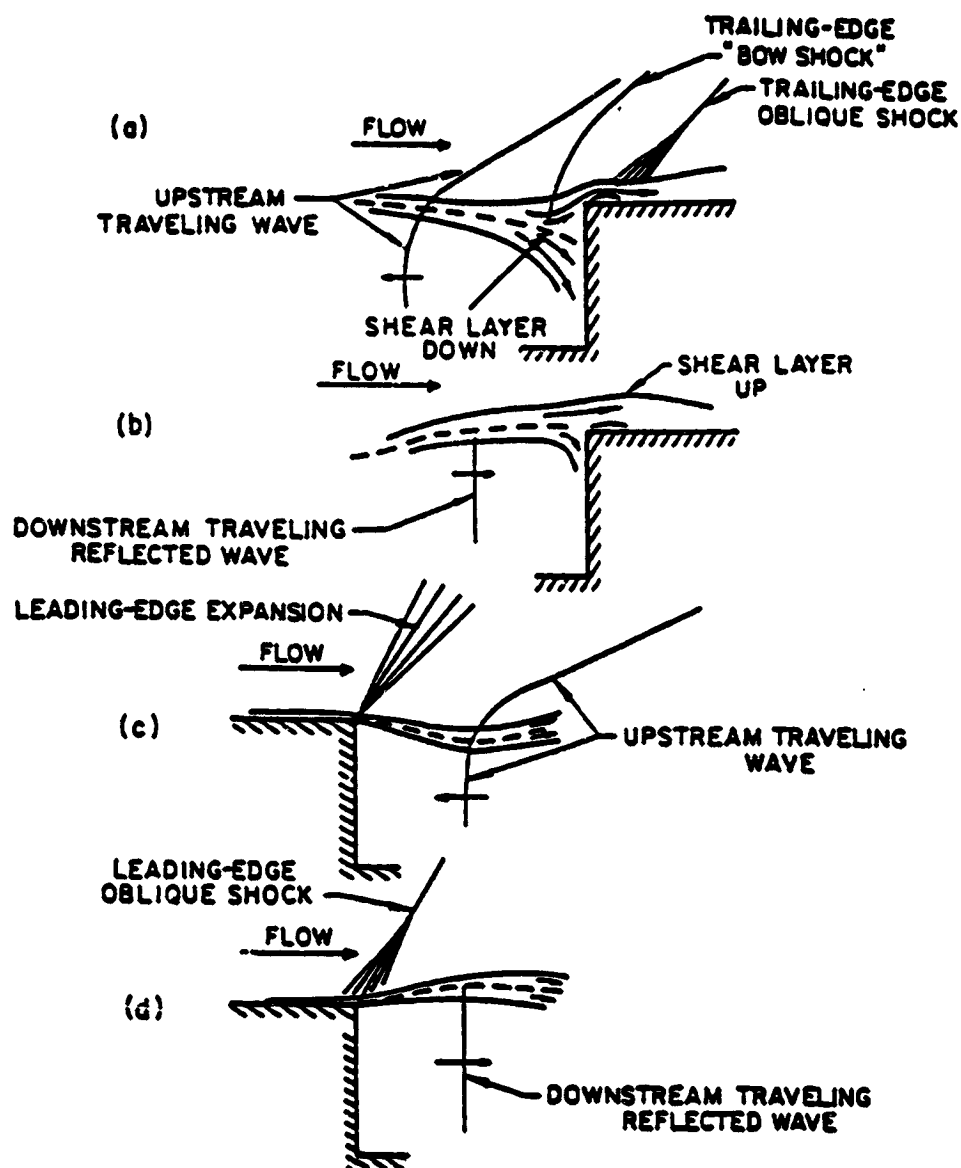
Fig.2.4 (a) and (b) Stages of trailing edge flow impingement,
       (c) and (d) leading edge flow separation within an
       oscillation cycle.

UPSTREAM TRAVELING WAVE

LEADING-EDGE
OBLIQUE SHOCK

M>1

TRAILING-EDGE
"BOW-WAVE" SHOCK

TRAILING-EDGE
OBLIQUE SHOCK

(a) EXTERNAL RADIATION
PATTERN IN SUPERSONIC FLOW
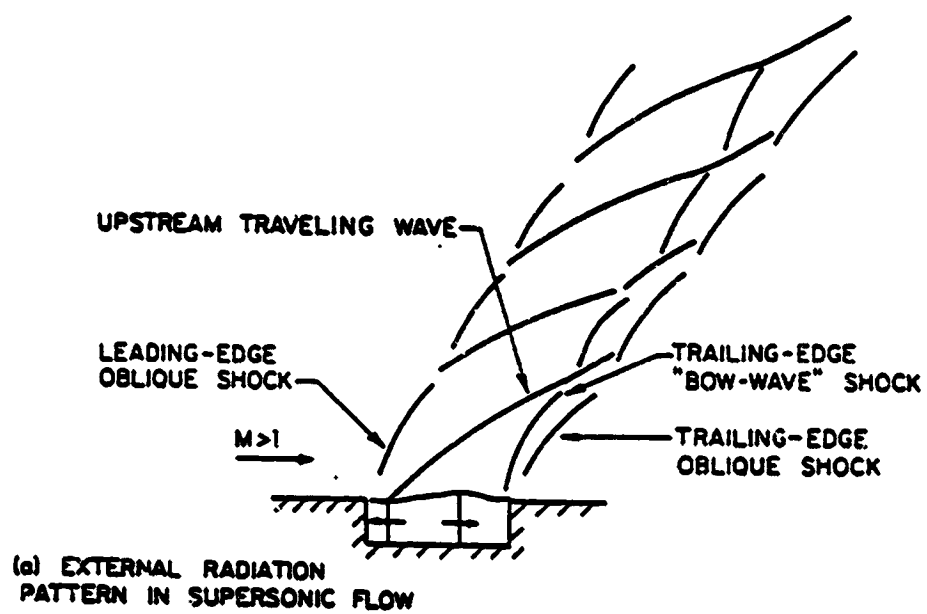
Fig. 2.5 Typical cavity external radiation patterns
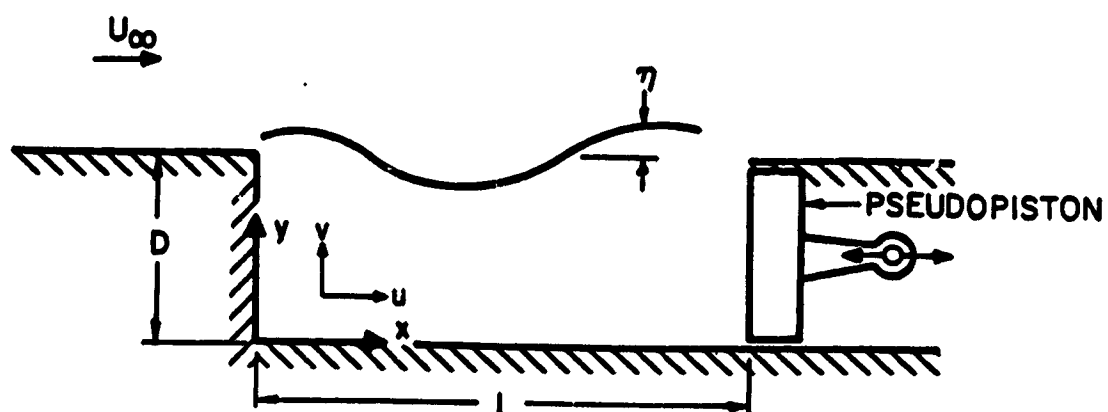
Fig. 2.6 Pseudopiston
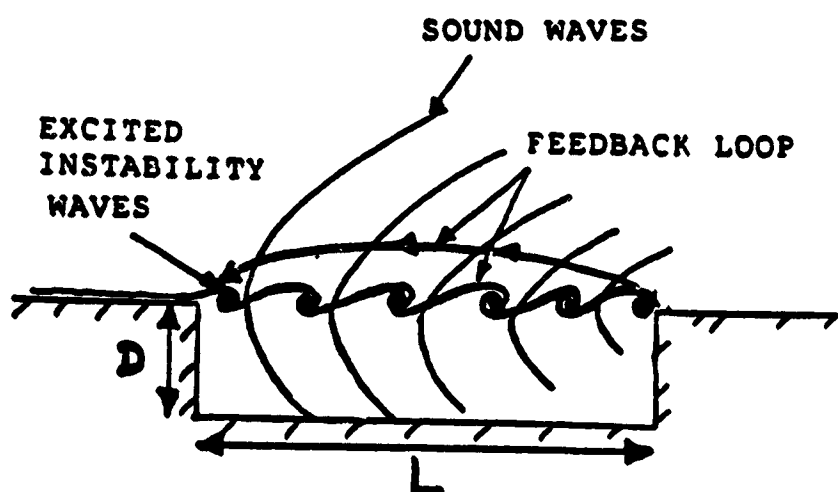
Fig. 2.7 Feedback loop responsible for cavity oscillations.

Chapter 3

MATHEMATICAL MODEL

3.1 Governing Equations

The governing equations are the three-dimensional, time dependent, compressible, complete Navier-Stokes equations in terms of Reynolds averaged variables. These equations are written in general coordinates and conservative form [38] as

$$\frac{\partial}{\partial t}U + \frac{\partial}{\partial \xi}(F \cdot F_v) + \frac{\partial}{\partial \eta}(G \cdot G_v) + \frac{\partial}{\partial \zeta}(H \cdot H_v) = 0 \quad . \tag{3.1}$$

where U is the vector of conserved variables,

$$U = \frac{1}{J}[\rho, \rho u, \rho v, \rho w, \rho E]^T$$

and F, G, H are the inviscid flux vectors,

$$F = 1/J \begin{bmatrix} \rho U_1 \\ \rho u U_1 + \partial_1 \xi^1 p \\ \rho v U_1 + \partial_2 \xi^1 p \\ \rho w U_1 + \partial_3 \xi^1 p \\ (E+p)U_1 \end{bmatrix}, \quad G = 1/J \begin{bmatrix} \rho U_2 \\ \rho u U_2 + \partial_1 \xi^2 p \\ \rho v U_2 + \partial_2 \xi^2 p \\ \rho w U_2 + \partial_3 \xi^2 p \\ (E+p)U_2 \end{bmatrix}, \quad H = 1/J \begin{bmatrix} \rho U_3 \\ \rho u U_3 + \partial_1 \xi^3 p \\ \rho v U_3 + \partial_2 \xi^3 p \\ \rho w U_3 + \partial_3 \xi^3 p \\ (E+p)U_3 \end{bmatrix} \tag{3.2}$$

and F_v, G_v, H_v are the viscous flux vectors,

$$G_v = 1/J \begin{bmatrix} 0 \\ \partial_k \xi^2 \tau_{k1} \\ \partial_k \xi^2 \tau_{k2} \\ \partial_k \xi^2 \tau_{k3} \\ \partial_k \xi^2 (u\tau_{k1} + v\tau_{k2} + w\tau_{k3} - q_k) \end{bmatrix} \quad F_v = 1/J \begin{bmatrix} 0 \\ \partial_k \xi^1 \tau_{k1} \\ \partial_k \xi^1 \tau_{k2} \\ \partial_k \xi^1 \tau_{k3} \\ \partial_k \xi^1 (u\tau_{k1} + v\tau_{k2} + w\tau_{k3} - q_k) \end{bmatrix} \tag{3.3}$$

22

$$Hv = 1/J \begin{bmatrix} 0 \\ \partial_k \xi^3 \tau_{k1} \\ \partial_k \xi^3 \tau_{k2} \\ \partial_k \xi^3 \tau_{k3} \\ \partial_k \xi^3 \left(u\tau_{k1} + v\tau_{k2} + w\tau_{k3} - q_k \right) \end{bmatrix}$$

The contravariant velocity components (U_1, U_2, U_3) are defined by

$$U_1 = \partial_1 \xi^1 u + \partial_2 \xi^1 v + \partial_3 \xi^1 w,$$

$$U_2 = \partial_1 \xi^2 u + \partial_2 \xi^2 v + \partial_3 \xi^2 w, \qquad (3.4)$$

$$U_3 = \partial_1 \xi^3 u + \partial_2 \xi^3 v + \partial_3 \xi^3 w.$$

The stress and heat flux terms used in the equations above are given by

$$\tau_{k1} = \left(\partial_1 \xi^n - \frac{2}{3} \delta_{k1} \partial_k \xi^n \right) \frac{\partial u_k}{\partial \xi^n} + \partial_k \xi^n \frac{\partial u_1}{\partial \xi^m} \qquad (3.5)$$

$$\tau_{k2} = \left(\partial_2 \xi^n - \frac{2}{3} \delta_{k2} \partial_k \xi^n \right) \frac{\partial u_k}{\partial \xi^n} + \partial_k \xi^n \frac{\partial u_2}{\partial \xi^m},$$

$$\tau_{k3} = \left(\partial_3 \xi^n - \frac{2}{3} \delta_{k3} \partial_k \xi^n \right) \frac{\partial u_k}{\partial \xi^n} + \partial_k \xi^n \frac{\partial u_2}{\partial \xi^m},$$

$$q_k = -k \frac{\partial T}{\partial \xi^m}.$$

where k, n, and m are dummy variables.

And $\partial_1 = \partial/\partial x$, $\partial_2 = \partial/\partial y$, $\partial_3 = \partial/\partial z$, $\xi^1 = \xi$, $\xi^2 = \eta$, and $\xi^3 = \zeta$.

The total energy, E, and the internal energy, e, are defined as follows,

$$E = e + 1/2(u^2 + v^2 + w^2) \qquad (3.6)$$

$$e = C_v T \qquad (3.7)$$

The perfect gas law

$$p = (\gamma - 1) \ e = \rho RT \qquad (3.8)$$

and Sutherland's laminar viscosity law have been used to complete the system of equations. For turbulent flow, the total viscosity μ, is defined as the sum of molecular viscosity (μ_l) and the turbulent eddy viscosity (μ_t). An algebraic turbulent model is used to calculate the eddy viscosity.

3.2 Turbulence Model

The effect of turbulence is accounted for through the concepts of an eddy viscosity, μ_t, and eddy conductivity. In the momentum equations, the molecular viscosity, μ_l, is replaced by an effective viscosity, μ_e:

$$\mu_e = \mu + \mu_t = \mu \ (1 + \mu_t/\mu) \qquad (3.9)$$

The study of the turbulent flow and adequate modeling of Reynolds stresses (here it will be referred to as turbulence modeling) are current subjects of research. They have not yet been fully understood, and up to now, we still cannot find a perfect and efficient model. The modeling of turbulence is complicated by the fact that several length scales exist which control the generation, transport and the dissipation of turbulent kinetic energy. A simple empirical model that can estimate compressible turbulent boundary layers with separated flow has been selected for this study. This bas two-layer algebraic turbulence model was proposed by Cebeci [39]. It is based on the Boussinesq approximation of modeling the general Reynolds stresses by an eddy viscosity, similar to molecular viscosity. This model was later modified by Baldwin and Lomax [40].

The mixing length model employed in the Baldwin-Lomax model divides the shear layer into an inner and outer region, and is patterned after a method developed for attached boundary layers by Cebeci [39]. It is a two-layer algebraic eddy viscosity

model in which μ_t is given by

$$\mu_t = \begin{cases} (\mu_t)_{inner} \ , & y < y_{crossover} \\ (\mu_t)_{outer} \ , & y_{crossover} < y \end{cases} \tag{3.10}$$

In the inner region, the eddy viscosity is given by the Prandtl-Van Driest formulation,

$$\mu_i = (kyD)^2 |\omega| \tag{3.11}$$

where

$$D = 1 - \exp(-y^+/A^+)$$

$$y^+ = \rho_w u_\tau y \Big/ \mu_w = \sqrt{\rho_w \tau_w} \ y \Big/ \mu_w \ .$$

In the outer region, Baldwin-Lomax model uses the Clauser formulation for the outer region,

$$\mu_o = KC_{cp} F_{wake} F_{KLEB}(y) \tag{3.12}$$

and

$$F_{WAKE} = \min \left[y_{max} F_{max}, \ C_{wk} y_{max} U^2_{dif}/F_{max} \right] \tag{3.13}$$

The quantities y_{max} and F_{max} are determined from the function:

$$F(y) = y|W|[1 - \exp(-y^+/A^+)]. \tag{3.14}$$

In wakes, the exponential term of above equation is set equal to zero. The quantity F_{max} is the maximum value of $F(y)$ that occurs in a profile and y_{max} is the value of y at which it occurs. The Klebanoff intermittency correction and U_{dif} are given by

$$F_{KLEB}(y) = [1 + 5.5(C_{KLEB}/y_{max})^6]^{-1} \tag{3.15}$$

$$U_{dif} = (u^2 + v^2 + w^2)^{0.5}_{max} - (u^2 + v^2 + w^2)^{0.5}_{min} \tag{3.16}$$

The second term in U_{dif} is taken to be zero (except in wakes). The values of the constants are:

$$A^+ = 26, \quad C_{cp} = 1.6, \quad C_{KLEB} = 0.3, \quad C_{wk} = 0.25,$$

$$P_r = 0.72, \quad P_{rt} = 0.9, \quad C_{MUTM} = 14.$$

The outer formulation can be used in wakes as well as in attached and separated boundary layers. The distribution of vorticity is used to determine length scales so that the necessity for finding the outer edge of the boundary layer (or wake) is removed.

The inner and the outer eddy viscosity models are combined to form the turbulent eddy viscosity μ_t in the following manner. First, profiles of μ_i and μ_o are obtained on each coordinate line emanating from the wall. The first point near the wall at which μ_i exceeds μ_o is denoted the "cross over point". The turbulent eddy viscosity μ_t is then equal to μ_i for all points between the wall and the cross-over point, and it is equal to μ_o for all points above and including the cross-over point.

Some modifications have been done to the model for all the points within and close to the cavity. These are Degani-Schiff modifications, the multiple-wall modification, and the wake modifications.

3.2.1 Degani-Schiff modifications [41]

The major difficulty encountered in applying the Baldwin-Lomax turbulence model to vortical flows is the evaluation of the length scale, y_{max}, and in turn determining $(\mu_t)_{outer}$ for boundary-layer profiles in the cross flow separation region. In Fig. 3.1a, a general $F(y)$ curve is shown. If there is a strong overlying vortex, then $F(y)$ curve may switch to Fig. 3.1b. In addition to a local peak in $F(y)$ in the attached boundary layer at $y = a$, the overlying vortex structure causes a larger peak in $F(y)$ at $y = b$. The choice of the peak at $y = b$ results in a value of F_{wake} and, in turn, a value of $(\mu_t)_{outer}$ which is much too high. Thus, in general, the computed eddy-viscosity coefficient in the cross flow separation region behind the primary separation point will be too high. This will cause the details of the computed flow to be distorted or washed out.

To eliminate these difficulties we have modified our implementation of the turbulence model. At each computational coordinate the code searches outward, sweeping

from wall to free stream, in order to find the first peak in F(y), and then cut off the search when the peak is reached. To prevent the selection of erroneous peaks which might be caused by a nonsmooth behavior in F(y), a peak is considered to have been found when the value of F(y) drops to 90% of the local maximum value.

For most cases, in the cross flow separation region, the two peaks in F(y) are spaced far enough apart that the logic described above will select the first peak. However, this is not true in the vicinity of the primary separation and immediately following the secondary separation Under these conditions the code would choose a value of y_{max} near the top edge of the cavity. Consequently, a cutoff distance is specified in terms of y_{max} from the previous value, i.e.,

$y_{cutoff} = C \, y_{max(previous)}$, where C is a constant chosen equal to 1.5.

3.2.2 Multiple-wall Modifications [4]

The second modification is the inclusion of multiple-wall effects for points in the proximity of concave edges and corners. Eddy viscosity values were computed using the vertical walls (FF, RF, SW) for such points, in addition to computing eddy viscosity values using the horizontal walls (FP1, F, FP2, SFP) for all the points in the computation zone. Then an effective eddy viscosity was computed through inverse averaging. For example, μ_t was computed as follows for a point near the corner of FF, SW and F:

$$\mu_t = \frac{(\mu/y^+)_F + (\mu/y^+)_{FF} + (\mu/y^+)_{SW}}{\sqrt{(y^+)^2_F + (y^+)^2_{FF} + (y^+)^2_{SW}}} \qquad (3.17)$$

which increased the influence of the wall with the lowest (y+) value.

3.2.3 Wake-model Modifications

The abrupt change in the eddy viscosity coefficient from the boundary layer to the wake is approximated using the concept of a relaxation eddy viscosity model to represent the different length scales in the problem.

For the cavity, the eddy viscosity is calculated by

$$\mu_t = \mu_{tu} + (\mu_u - \mu_{tu}) \, [1 - \exp(-x/10\,\delta)] \tag{3.18}$$

where

μ_{tu} : the value at the upstream lip,

μ_u : Baldwin-Lomax eddy viscosity value,

δ : instantaneous boundary layer thickness at upstream lip,

x : streamwise distance from the corner.

This modification is known as the relaxation model, which has been shown to work well for other numerical calculations [42]. It accounts for the history effects of the fluid. The eddy viscosity (μ_t) has been set to zero at all the solid surfaces.

3.3 Initial and Boundary Conditions

In computational fluid dynamics, the initial conditions usually correspond to a real situation for a transient problem. In practice, initial conditions are obtained from experiments, empirical relations, approximate theories, or previous computational results. An improper initial guess may result in solution failure. An important requirement for the initial condition is that they should be physically as close as possible to the actual nature of the flow field.

A reasonable approach has been to initialize the entire flow field above the cavity with the inflow conditions. Within the cavity region, depending on the type of cavity, the initial conditions are different. In deep cavities, the flow within the cavity is

subsonic which was known from experimental observations. Therefore the velocity inside the cavity has been arbitrarily specified as 10% of its free stream value. In shallow cavities, the shear layer impinges on the cavity floor. As a result, an approximate velocity profile close to the inflow velocity profile has been specified within the cavity. The pressure and temperature within the cavity has been set to the free stream value.

Correct boundary conditions are essential to the success of numerical calculations. Six faces require attention in the specification of boundary conditions. On solid surfaces, a no-slip boundary condition has been used so that all the velocity vectors vanish. In the test cases, the wall has been considered to be adiabatic. The pressure at the solid surfaces has been obtained by a zero-order extrapolation from the interior point value of pressure in a direction normal to the wall. The density is obtained from the state equation.

$$u = v = w = 0, \quad \partial p/\partial n = 0, \quad \partial T/\partial n = 0. \tag{3.19}$$

In the case of supersonic in flow (except in the subsonic portion of the boundary layer close to the wall), all flow characteristics point from the outside towards the inside of the computational domain. Therefore, all elements of the primitive variables (vector U in Eq. 3.1) have been specified by a profile generated using the two-dimensional compressible boundary-layer equations for perfect-gas flows (the governing equations are solved by an iterative three-point implicit finite-difference procedure) [43]. In the subsonic and transonic inflow, all flow characteristics, except one, point from outside towards the inside of the computational domain. Therefore, only the variables u, v, w, and T at the inflow are specified. The pressure has been extrapolated from the computational domain, to allow for the information to be propagated upstream. The pressure within the boundary layer is maintained at the value of boundary layer edge.

$$u = u_{(b.l.\ profile)}, \quad v = v_{(b.l.\ profile)}, \quad w = 0, \quad T = T_{(b.l.\ profile)}, \tag{3.20}$$

supersonic inflow: $P = P$,

subsonic inflow: $P_{1,j} = P_{2,j}$ (for j above the boundary layer),

$P_{1,j} = P_e$ (for j within the boundary layer),

P_e: value of pressure at the boundary layer edge.

When the outflow field is supersonic, the flow characteristics point from the inside of the computational domain to outside. Therefore, all variables at the outflow can be determined from the interior flow solution by a zero-order extrapolation. When the outflow field is subsonic, since there is only one incoming characteristic, only one analytic boundary condition is required. Therefore, we only specify static pressure, and other variables are obtained by a zero-order extrapolation,

$$\partial u/\partial s = 0, \quad \partial v/\partial s = 0, \quad \partial w/\partial s = 0, \quad \partial T/\partial s = 0, \tag{3.21}$$

$$\partial P/\partial s = 0, \text{ (supersonic outflow)}$$

$$P_{exit} = P_{back\ pressure}, \text{ (subsonic outflow)}.$$

where s indicates the streamwise coordinate.

The far field refers to the flow field at a distance away from the body which is greater than the reference length of the cavity. The boundary conditions are specified by zero-order extrapolation from inside the computational domain for outflow, and as free stream conditions for inflow. The pressure values are assumed to be free stream at this boundary.

$$\partial u/\partial n = 0, \quad \partial v/\partial n = 0, \quad \partial w/\partial n = 0, \tag{3.22}$$

$$\partial T/\partial n = 0, \quad P = P.$$

On the symmetry plane, the following boundary conditions are used:

$$\partial u/\partial n = 0, \quad \partial v/\partial n = 0, \quad w = -w, \tag{3.23}$$

$$\partial T/\partial n = 0, \quad \partial P/\partial n = 0.$$
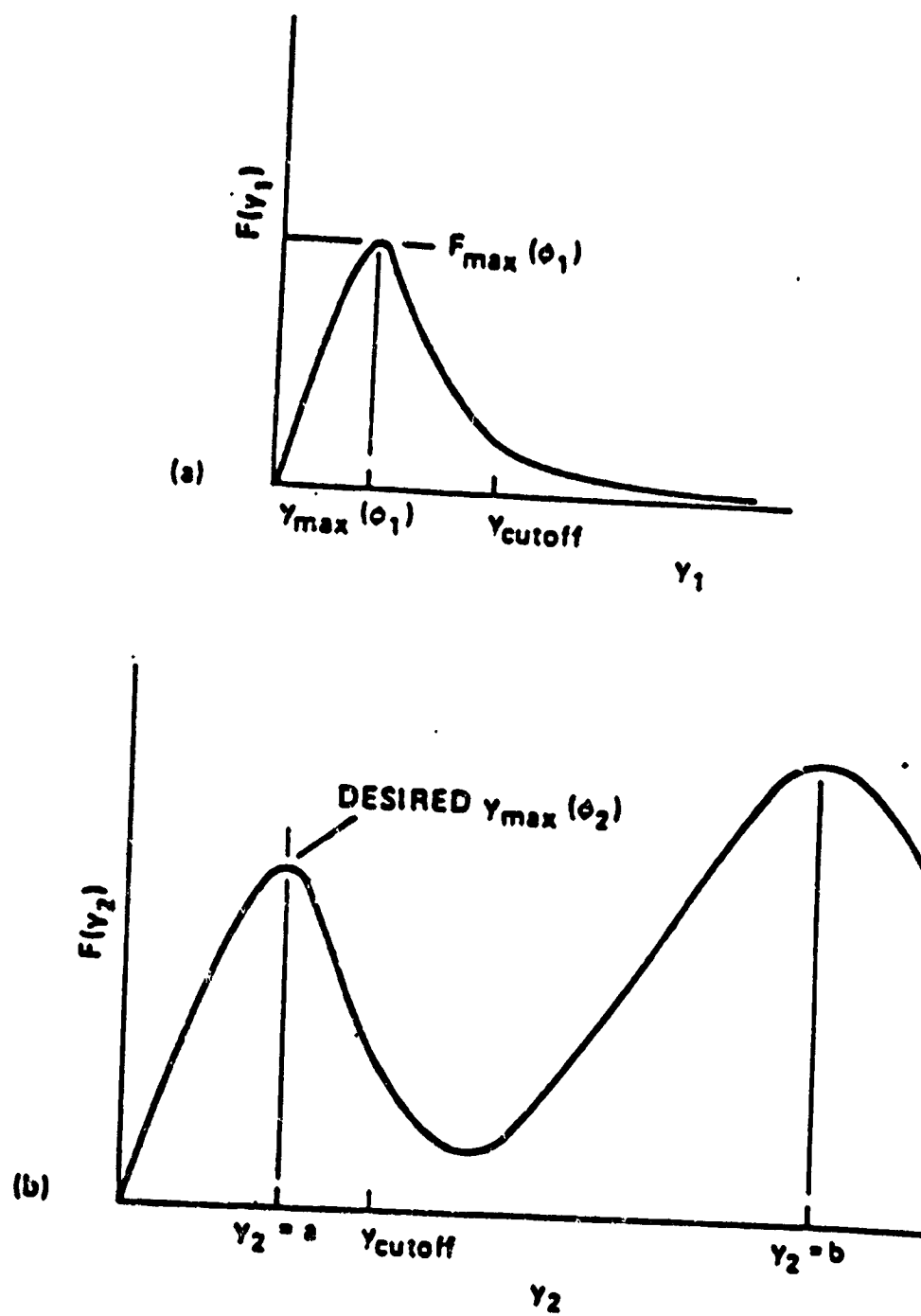
Fig. 3.1 Behavior of F(y)

Chapter 4

NUMERICAL PROCEDURE

A schematic of a cavity model is shown in Fig. 4.1a. It has been found from experimental observations, that cavity flows are almost symmetric about the cavity centerplane (streamwise direction). In order to reduce the computational time and memory a half span cavity has been modeled. One of the models is shown in Fig. 4.1b.

The next step is the grid generation, which depends upon the flow, the geometric configuration, computational resources, the required accuracy of the solution, the physical dimensions, and the boundary layer thickness. In the present analysis, three-dimensional cartesian grids are used because of the geometry. Stretched grids are needed in all of the three directions, so that the entire computational domain can be covered with a reasonable number of grid points. In regions which experience large gradients of the flow properties, such as, close to the solid walls, and shear layer region, the grid points are clustered.

The grids are generated algebraically. The cavity is divided into several zones. An exponential stretching function given below is used to cluster the grids in each zone:

$$y = y_{max} \left[\left(\exp(k\delta) - 1 \right) \Big/ \left(\exp(k) - 1 \right) \right] . \tag{4.1}$$

where, y_{max} is the maximum value of y in the computational zone. The value of k is chosen proportional to the clustering needed. The minimum spatial step size is of the order $10^{-5}D$, and the maximum cell aspect ratio is around 100.

4.1 Explicit, MacCormack, Finite-Difference Scheme (EMFD)

The MacCormack finite-difference method |44| is a variation of the two-step Lax-Wendroff scheme. This scheme is second order accurate in time and space. This explicit method has restrictions on the time step of integration as given by Courant-Freidrichs-Lewy |38|. It has been used to solve Euler and Navier-Stokes equations for numerous practical flow situations, including laminar and turbulent boundary layer shock interaction.

The predictor-corrector explicit algorithm is summarized below in general coordinates.

Predictor:

$$\Delta U_{i,j,k}^{n} = -\Delta t \left[\Delta_\xi F_{i,j,k}^{n} + \Delta_\eta G_{i,j,k}^{n} + \Delta_\zeta H_{i,j,k}^{n} \right] \tag{4.2}$$

$$U_{i,j,k}^{\overline{n+1}} = U_{i,j,k}^{n} + \Delta U_{i,j,k}^{n}$$

Corrector:

$$\Delta U_{i,j,k}^{\overline{n+1}} = -\Delta t \left[\nabla_\xi F_{i,j,k}^{\overline{n+1}} + \nabla_\eta G_{i,j,k}^{\overline{n+1}} + \nabla_\zeta H_{i,j,k}^{\overline{n+1}} \right] \tag{4.3}$$

$$U_{i,j,k}^{n+1} = \frac{1}{2} \left[U_{i,j,k}^{n} + U_{i,j,k}^{\overline{n+1}} + \Delta U_{i,j,k}^{\overline{n+1}} \right]$$

where Δ_ξ, Δ_η, Δ_ζ are forward spatial differences, and ∇_ξ, ∇_η, ∇_ζ are backward differences.

The coordinate transformation is chosen such that $\Delta\xi = \Delta\eta = \Delta\zeta = 1.0$. This two step process consists of evaluating spatial derivatives by one-sided differences taken in opposite directions on alternate steps. Although the one-sided differences are first-order accurate, the combined predictor-corrector step gives the second order accuracy.

Because of the complexity of the compressible Navier-Stokes equations, it is not possible to obtain a closed form stability expression for the scheme. The most success-

ful attempt to date has been to linearize the set of differential equations and then study the amplification of the Fourier components of the solution by the difference method applied to the linearized set.

For stability, the time step is restricted by the CFL (Courant, Friedrichs, and Lewy) condition given by

$$CFL = t\lambda_{max}/\Delta_\xi \tag{4.4}$$

$$\Delta t \le \frac{\sigma(CFL)}{1 + 2/Re_\Delta}$$

where λ_{max} is the maximum eigenvalue of the set of Jacobian matrices, σ is the safety factor (≈ 0.9), and Re is the minimum mesh Reynolds number given by:

$$Re_\Delta = \min(Re_{\Delta x}, Re_{\Delta y}, Re_{\Delta z}) \tag{4.5}$$

$$Re_{\Delta x} = \frac{\rho|u|\Delta x}{\mu}$$

$$Re_{\Delta y} = \frac{\rho|v|\Delta y}{\mu}$$

$$Re_{\Delta z} = \frac{\rho|w|\Delta z}{\mu}$$

The linear stability analysis imposes a restriction on the time step in each direction (ξ, η, and ζ).

$$\Delta t_\xi < \min \frac{\Delta\xi}{|u\xi_x + v\xi_y + w\xi_z| + a\sqrt{(\xi_x^2 + \xi_y^2 + \xi_z^2)}} \tag{4.6}$$

$$\Delta t_\eta < \min \frac{\Delta\eta}{|u\eta_x + v\eta_y + w\eta_z| + a\sqrt{(\eta_x^2 + \eta_y^2 + \eta_z^2)}}$$

$$\Delta t_\zeta < \min \frac{\Delta\zeta}{|u\zeta_x + v\zeta_y + w\zeta_z| + a\sqrt{(\zeta_x^2 + \zeta_y^2 + \zeta_z^2)}}$$

The global time step is determined as $\Delta t = \min[\Delta t_\xi, \Delta t_\eta, \Delta t_\zeta]$.

For practical computations, especially in the region of large gradients, such as shocks, strong vortices, and separation, the solution exhibits oscillations. These oscillations sometimes will cause the numerical code to "fail". In order to suppress the oscillations, we add damping terms known as "artificial viscosity" into the differenced governing equation. The fourth order damping term devised by MacCormack and Baldwin [45], is given below:

$$(\Delta x)^4 \frac{\partial}{\partial x} \left\{ \left[\left(\frac{|u|+a}{4p}\right) \varepsilon_p \left|\frac{\partial^2 p}{\partial x^2}\right| + \left(\frac{|u|+a}{4T}\right) \varepsilon_T \left|\frac{\partial^2 T}{\partial x^2}\right| \right] \frac{\partial U}{\partial x} \right\} \qquad (4.7)$$

$$(\Delta y)^4 \frac{\partial}{\partial y} \left\{ \left[\left(\frac{|v|+a}{4p}\right) \varepsilon_p \left|\frac{\partial^2 p}{\partial y^2}\right| + \left(\frac{|v|+a}{4T}\right) \varepsilon_T \left|\frac{\partial^2 T}{\partial y^2}\right| \right] \frac{\partial U}{\partial y} \right\}$$

$$(\Delta z)^4 \frac{\partial}{\partial z} \left\{ \left[\left(\frac{|w|+a}{4p}\right) \varepsilon_p \left|\frac{\partial^2 p}{\partial z^2}\right| + \left(\frac{|w|+a}{4T}\right) \varepsilon_T \left|\frac{\partial^2 T}{\partial z^2}\right| \right] \frac{\partial U}{\partial z} \right\}$$

where $0 < \varepsilon_p < 0.5$ and $0 < \varepsilon_T < 0.5$.

The features of the numerical algorithm have been embodied in a solver written in FORTRAN 200 language using 64-bit arithmetic specifically for the CYBER-205 computer [46]. The vectorization executes in ξ planes. Approximately 3.25 million words of memory is required for grid points. The mean data processing rate is 5×10^6 cpus/time step/grid point on the CYBER-205 computer of NASA Langley Research Center.

4.2 Implicit Upwind, Finite-Volume Scheme (IUFV)

The finite volume discretization is another means of developing difference approximations to partial differential equations. It is in this form that the equations

express rates of change in a finite volume in terms of the resultant fluxes through the boundary of the volume. These equations provide average values of the solution over the volume. The advantage of the integral form is that it remains valid in the presence of discontinuities in the flow, such as a shock or a separation. The integral form (stationary control volume) of the governing equations is

$$\frac{\partial}{\partial t} \int \int \int_V U.dV + \int \int_S \vec{F}.\vec{n}\, ds = 0 \ . \tag{4.8}$$

where $\vec{F} = [(F-F_v), (G-G_v), (H-H_v)]$ and $\vec{n} = n_\xi \vec{\xi} + n_\eta \vec{\eta} + n_\zeta \vec{\zeta}$ is a unit normal vector pointing outward from the surface S, bounding the volume V. We can use the divergence theorem to change the surface integral to a volume integral

$$\int \int \int_V \frac{\partial U}{\partial t}.dV + \int \int \int \nabla.\vec{F}\, dV = 0 \ . \tag{4.9}$$

Assuming continuity of the integrand in the above equation, the differential conservation law form of the governing equations can be written as

$$\frac{\partial}{\partial t} U + \frac{\partial}{\partial \xi}(F - F_v) + \frac{\partial}{\partial \eta}(G - G_v) + \frac{\partial}{\partial \zeta}(H - H_v) = 0 \ . \tag{4.10}$$

For generality, the governing equations are put into nondimensional form. We use the cavity depth as the reference length $\widetilde{L}$

$$\rho = \frac{\tilde{\rho}}{\rho_\infty} \ , \quad p = \frac{\tilde{p}}{\rho_\infty \tilde{a}_\infty^2} \ , \quad a = \frac{\tilde{a}}{a_\infty} \ , \quad e = \frac{\tilde{e}}{\rho_\infty a_\infty^2} \ , \tag{4.11}$$

$$u = \frac{\tilde{u}}{a_\infty} \ , \quad v = \frac{\tilde{v}}{a_\infty} \ , \quad w = \frac{\tilde{w}}{a_\infty} \ , \quad T = \frac{\tilde{T}}{T_\infty} = \frac{\gamma p}{\rho} = a^2 \ .$$

The finite volume method is adopted to handle arbitrary configurations since the method can more easily treat complicated grid structure than finite difference formulations. We can discretize the flow field into a set of ordered hexagonal cells (volumes) and apply governing equations to each volume directly. Thus, a semi-discrete represen-

tation of governing equation can be written as

$$\left[\frac{\partial}{\partial t}\langle U\rangle v\right]_{i,j,k} + \sum_{i=1}^{6}\left[\int\int_s(\vec{F}\cdot\vec{n})ds\right]_{i,j,k} = 0, \tag{4.12}$$

or, in more detail

$$\left(\frac{\partial U}{\partial t}\right)_{i,j,k} + \frac{(F-F_v)_{i+\frac{1}{2},jk} - (F-F_v)_{i-\frac{1}{2},jk}}{\Delta\xi} + \frac{(G-G_v)_{i,j+\frac{1}{2},k} - (G-G_v)_{i,j-\frac{1}{2},k}}{\Delta\eta} \tag{4.13}$$

$$+ \frac{(H-H_v)_{i,j,k+\frac{1}{2}} - (H-H_v)_{i,j,k-\frac{1}{2}}}{\Delta\zeta} = 0$$

where, for convenience

$$\Delta\xi = \xi_{i+\frac{1}{2}} - \xi_{i-\frac{1}{2}} = 1 \quad , \tag{4.14}$$

$$\Delta\eta = \eta_{i+\frac{1}{2}} - \eta_{i-\frac{1}{2}} = 1 \quad ,$$

$$\Delta\zeta = \zeta_{i+\frac{1}{2}} - \zeta_{i-\frac{1}{2}} = 1 \quad .$$

and by virtue of the integral representation,

$$U^a_{i,j,k} = \frac{1}{V}\left[\int\int\int U(\xi,\eta,\zeta,t)\,dV\right]_{i,j,k} \quad . \tag{4.15}$$

U is regarded as a cell average value rather than a pointwise value at the cell center.

For solving the Navier-Stokes equations, the theory of characteristics is crucial in determining the directions of the signal propagation, the information gained from characteristic theory. Recently, much interest has been generated in the development of numerical methods that model the underlying physics, as dictated by characteristic theory, at each point. Some of the methods include flux-vector splitting, and flux-difference splitting. These methods can be classified as upwind methods and have the advantage of being naturally dissipative. The advantages of upwind methods over central difference techniques are 1: enhance stability properties, and 2: eliminate explicitly artificial viscosity or damping terms.

Since the pioneering work of Steger and Warming[48] in the early 1980s, the upwind method has grown rapidly. The schemes used in here are based on the method developed by Beam and Warming [49,50]. The scheme for solving the compressible Navier-Stokes equations belongs to the same class of ADI methods developed by McDonald and Briley [64].

After Euler implicit time integration and linearization, the governing equations can be expressed in difference form as:

$$\left[\frac{I}{J\Delta t}+\partial_\xi\left(\frac{\partial F}{\partial U}-\frac{\partial F_v}{\partial U}\right)+\partial_\eta\left(\frac{\partial G}{\partial U}-\frac{\partial G_v}{\partial U}\right)+\partial_\zeta\left(\frac{\partial H}{\partial U}-\frac{\partial G_v}{\partial U}\right)\right]^a\Delta U$$

$$=-\left[\partial_\xi(F-F_v)+\partial_\eta(G-G_v)+\partial_\zeta(H-H_v)\right]^a=-R^a \tag{4.16}$$

These equations are very difficult to solve due to the large banded matrix. The left hand side requires an inversion of a very large matrix. There are a number of approximate factorizations to split the resulting large banded block matrix equation into a sequence of easily solvable equations. We use a three factor block tridiagonal scheme that is fully vectorizable in which the implicit operator is factored such that each directional factor contains the Jacobians associated with that direction only. The three factor scheme can be written as

$$\left[\frac{I}{J\Delta t}+\partial_\xi\frac{\partial}{\partial U}(F-F_v)\right]^a\left[\frac{I}{J\Delta t}+\partial_\eta\frac{\partial}{\partial U}(G-G_v)\right]^a\left[\frac{I}{J\Delta t}+\partial_\zeta\frac{\partial}{\partial U}(H-H_v)\right]^a\Delta U=-R^a. \tag{4.17}$$

Apply spatially split approximate factorization

$$\left[\frac{I}{J\Delta t}+\partial_\xi\frac{\partial}{\partial U}(F-F_v)\right]^a\Delta U^*=-R^a , \tag{4.18}$$

$$\left[\frac{I}{J\Delta t}+\partial_\eta\frac{\partial}{\partial U}(G-G_v)\right]^a\Delta U^{**}=\left(\frac{I}{J\Delta t}\right)\Delta U^* ,$$

$$\left[\frac{I}{J\Delta t}+\partial_\zeta\frac{\partial}{\partial U}(H-H_v)\right]^a\Delta U=\left(\frac{I}{J\Delta t}\right)\Delta U^{**} .$$

The solution only requires block tri-diagonal inversions and is followed by the update step $U^{n+1} = U^n + \Delta U$.

The essence of flux difference splitting techniques [51] is the solution of local Riemann problems stemming from the consideration of piecewise uniform states between cell interfaces and an initial data line. Roe [52] proposed a method of exploiting the fact that the Riemann solution for any set of linear conservation laws can be easily computed. Roe's idea was to obtain an exact solution of the Riemann problem for the following linear hyperbolic system, rather than using an approximate solution to the exact equation. This system, is approximated by

$$\frac{\partial U}{\partial t} + [A](U_L, U_R)\frac{\partial U}{\partial \xi} = 0 . \tag{4.19}$$

For flux terms, a monotone upstream centered scheme for conservation laws(MUSCL) approach is used. For example, in the ξ direction, the spatial derivatives are written conservatively as a flux balance across a cell as:

$$\left(\frac{\partial F}{\partial U}\right)_i = \left(F_{i+\frac{1}{2}} - F_{i-\frac{1}{2}}\right)\bigg/\left(\xi_{i+\frac{1}{2}} - \xi_{i-\frac{1}{2}}\right) . \tag{4.20}$$

where the interface flux is constructed as.

$$F_{i+\frac{1}{2}} = \frac{1}{2}\left[F\left(q^-\right) + F\left(q^+\right) - \left|\widetilde{A}\right|\left(U^+ - U^-\right)\right]_{i+\frac{1}{2}} . \tag{4.21}$$

q^+, and q^- denotes state variables on cell interfaces determinated from upwind biased interpolations of the primitive variables.

$$q^-_{i+\frac{1}{2}} = q_i + \left\{\frac{1}{4}\left[(1-\kappa)\overline{\Delta}_- + (1+\kappa)\overline{\Delta}_+\right]\right\}_i , \tag{4.22}$$

$$q^+_{i+\frac{1}{2}} = q_i - \left\{\frac{1}{4}\left[(1-\kappa)\overline{\Delta}_+ + (1+\kappa)\overline{\Delta}_-\right]\right\}_{i+1} .$$

where

$$(\Delta_+)_i = q_{i+1} - q_i, \quad (\Delta_-)_i = q_i - q_{i-1}$$

and the slope limiting is used to maintain monotonicity

$$\overline{\Delta}_+ = \max\left[0, \min\left(\Delta_+ \operatorname{sgn}\Delta_-, \beta\Delta_- \operatorname{sgn}\Delta_+\right)\right]\operatorname{sgn}\Delta_+,$$

$$\overline{\Delta}_- = \max\left[0, \min\left(\Delta_- \operatorname{sgn}\Delta_+, \beta\Delta_+ \operatorname{sgn}\Delta_-\right)\right]\operatorname{sgn}\Delta_-.$$

$$\beta = \frac{(3-\kappa)}{(1-\kappa)},$$

(4.23)

where

$$\kappa = \begin{cases} 1 & , \quad \text{central difference} \\ \dfrac{1}{3} & , \quad \text{flux-difference split} \end{cases}$$

rewrite the Jacobian metric

$$A = \frac{\partial F}{\partial U} = T\left(\wedge^+ + \wedge^-\right)T^{-1},$$

(4.24)

where

$$\wedge^{\pm} = \frac{\wedge \pm |\wedge|}{2}.$$

(4.25)

are diagonal matrices formed from the eigenvalues of A, i.e.

$$\Lambda = \operatorname{diag}\left(\lambda_1, \lambda_2, \lambda_3, \lambda_4, \lambda_5\right).$$

(4.26)

$$\lambda_1 = \lambda_2 = \lambda_3 = \frac{\widetilde{U}_1 |\nabla\xi|}{J},$$

$$\lambda_4 = \frac{\left(\widetilde{U}_1 + \widetilde{a}\right)|\nabla\xi|}{J},$$

$$\lambda_5 = \frac{\left(\widetilde{U}_1 - \widetilde{a}\right)|\nabla\xi|}{J}.$$

The contravariant velocity normal to the cell interface is

$$\bar{U}_1 = \left(\xi_x u + \xi_y v + \xi_z w \right) \Big/ |\nabla \xi| \ .$$

(4.27)

and the ' indicates a Roe averaged variable[53]

In order to develop the solution using considerably less computer time, each direction of the spatial factor is approximated separately with a diagonal inversion separately, such as

$$\left[\frac{I}{J\Delta t} + \partial_\xi \frac{\partial F}{\partial U} \right]^n \Delta U^* = T \left[\frac{I}{J\Delta t} + \partial_\xi^- \wedge^+ + \partial_\xi^+ \wedge^- \right] T^{-1} \Delta U^*$$

(4 28)

both side are then multiplied by T^{-1}, and hence the I-sweep then becomes:

$$\left[\frac{I}{J\Delta t} + \partial_\xi^- \wedge^+ + \partial_\xi^+ \wedge^- \right] \left(T^{-1} \Delta U^* \right) = -T^{-1} R \ .$$

(4.29)

Due to the repeated eigenvalues ($\lambda_1 = \lambda_2 = \lambda_3$), only three scalar tridiagonal LU decompositions are required for each line. The tridiagonal matrix can be written as

$$-\wedge^+ \left(M_{i-\frac{1}{2}}, U_{i-1} \right) \left(T^{-1} \Delta U^* \right)_{i-1} + \left[\frac{I}{J\Delta t} \wedge^+ \left(M_{i+\frac{1}{2}}, U_i \right) - \wedge^{-1} \left(M_{i-\frac{1}{2}}, U_i \right) \right] \left(T^{-1} \Delta U \right)_i \quad (4.30)$$

$$+ \wedge^- \left(M_{i+\frac{1}{2}}, U_{i+1} \right) \left(T^{-1} \Delta U^* \right)_{i+1} = -T_i^{-1} R_i \quad .$$

The metric terms M and state variables U are evaluated at cell centers. After the initialization and development of the flow, the diagonal inversions are turned off and more accurate block inversions are turned on.

The Van Leer type flux-vector splitting method [54,55] distinguishes between the influence of forward and backward moving particles in this model, the interaction between particles is done through mixing of a pseudo-particle going in and out of each cell according to a given velocity distribution.

Since the flux vectors are homogeneous functions of degree one in U, they are expressed in terms of their Jacobian matrices. Using a similarity transformation allows Jacobian matrices to be written as [56, 57, 30]:

$$F = [A]U = [T \Lambda T^{-1}]U \quad . \tag{4.31}$$

The matrix is a diagonal matrix composed of the eigenvalues of A and is given by

$$\Lambda = \begin{bmatrix} \lambda_1 & 0 & 0 & 0 & 0 \\ 0 & \lambda_2 & 0 & 0 & 0 \\ 0 & 0 & \lambda_3 & 0 & 0 \\ 0 & 0 & 0 & \lambda_4 & 0 \\ 0 & 0 & 0 & 0 & \lambda_5 \end{bmatrix} \tag{4.32}$$

where

$$\lambda_{1,2,3} = U = \xi_x u + \xi_y v + \xi_z w \quad . \tag{4.33}$$

$$\lambda_4 = U + |\nabla \xi| a \quad .$$

$$\lambda_5 = U - |\nabla \xi| a \quad .$$

The eigenvalues can be decomposed into nonnegative and nonpositive components

$$\lambda_i = \lambda_i^+ + \lambda_i^- \quad . \tag{4.34}$$

where

$$\lambda_i = \frac{\lambda_i \pm |\lambda_i|}{2} \quad . \tag{4.35}$$

Similarly, the eigenvalue matrix can be decomposed into $\Lambda = \Lambda^+ + \Lambda^-$, where Λ^+ is made up of nonnegative contributions of Λ and Λ^- is constructed of the nonpositive contributions of Λ . This splitting of the eigenvalue matrix, combined with equation (4.7) allows the flux vector to be rewritten as:

$$F = T(\Lambda^+ + \Lambda^-)T^{-1}U = (\overline{A}^+ + \overline{A}^-)U = F^+ + F^- \quad . \tag{4.36}$$

The flux vector has three distinct eigenvalues and can therefore be rewritten as a sum of three subvectors, as following:

$$\vec{F} = \vec{F}_1 + \vec{F}_2 + \vec{F}_3$$

The forward and backward flux vectors F^+ and F^- are formed by inserting $\lambda_i = \lambda_i^+$ and $\lambda_i = \lambda_i^-$, respectively.

For the purpose of splitting the flux vector, approximate factorization is used to solve the vector flux split equation, which in delta form, is the following:

$$\left[I + \Delta t \nabla_\xi A_1^+ + \Delta t \Delta_\xi A_1^- - \Delta t \partial_\xi^2 \left(\frac{N_1}{J} \right) \right] \times \left[I + \Delta t \nabla_\eta B_1^+ + \Delta t \Delta_\eta B_1^- - \Delta t \partial_\eta^2 \left(\frac{M_1}{J} \right) \right] \qquad (4.37)$$

$$\times \left[I + \Delta t \nabla_\zeta C_1^+ + \Delta t \Delta_\zeta C_1^- - \Delta t \partial_\zeta^2 \left(\frac{K_1}{J} \right) \right] (\Delta U) = -\Delta t (RHS)$$

where

$$A_1 = J \left(\frac{\partial F}{\partial U} \right), \qquad B_1 = J \left(\frac{\partial G}{\partial U} \right), \qquad C_1 = J \left(\frac{\partial H}{\partial U} \right), \qquad (4.38)$$

$$N_1 = J \left(\frac{\partial F_v}{\partial U} \right), \qquad M_1 = J \left(\frac{\partial G_v}{\partial U} \right), \qquad K_1 = J \left(\frac{\partial H_v}{\partial U} \right),$$

$$\Delta U = U^{n+1} - U^n,$$

$$RHS = \Delta_\xi F^+ + \Delta_\xi F^- + \Delta_\eta G^+ + \Delta_\eta G^- + \Delta_\zeta H^+ + \Delta_\zeta H^- - \left(\partial_\xi^2 F + \partial_\eta^2 G + \partial_\zeta^2 H \right) \Big/ J.$$

The split flux vector in the above equations is implemented as the flux across a cell, corresponding to MUSCL type differencing:

$$\nabla_\xi F^+ + \Delta_\xi F^- = \left[F^+ \left(U^- \right) + F^- \left(U^+ \right) \right]_{i+\frac{1}{2}} - \left[F^+ \left(U^- \right) + F^- \left(U^+ \right) \right]_{i-\frac{1}{2}}. \qquad (4.39)$$

The notation $F^+(U^-)_{i+1/2}$ denotes the forward flux evaluated using the metric terms at the cell interface $(i+\frac{1}{2})$ and the conserved state variables on the upwind side of the

interface, obtained by a fully upwind second-order state variable interpolation:

$$U_{i+1/2} = 1.5U_i - 0.5U_{i-1},$$ (4.40)

$$U_{i+1/2} = 1.5U_{i+1} - 0.5U_{i+2},$$

All the computational cells are advanced at equal time steps (time-accurate calculations require global time stepping) corresponding to a specified CFL number given by:

$$CFL = \Delta t \left\{ |U| + |V| + |W| + a \left[|\,grad\,(\xi)\,| + |\,grad\,(\eta)| + |\,grad\,(\zeta)| \right] \right\}$$ (4.41)

After that, the conserved variables are updated

$$U_{n+1} = U_n + \Delta U$$ (4.42)

The features of the numerical algorithm have been embodied in a solver written using FORTRAN 77 with 64-bit arithmetic specifically for the Cray-2 computer. Approximately 10 million words of memory are required for 150,000 grid points. The mean data processing rate is 6×10^{-6} cpus/time step/grid point on Cray-2 of NASA Langley Research Center.

4.3 Computational Flow Visualization

The visualization of the solution through graphics is an important area in computational fluid dynamics. This is essential since the amount of data generated by solving the equations is in the order of millions. Details of flow visualization have been addressed in [58]. The PLOT3D [59] is a popular graphics application program to create and interactively view flow field solutions. It is an application program in that it deals specially with computational fluid dynamics grid and data. In the current research, this program has been used extensively to represent the large amounts of data pictorially. The contours of pressure, density, temperature, and Mach number have been plotted.

4.4 Time Series Analysis

In the current study two characteristic times have been defined for convenience. The first characteristic time, t_{c1}, is defined as the time required for a fluid particle traveling at free stream velocity to traverse the length of the cavity. This parameter is useful in determining the computational time required to get past the non-physical initialization of the flow in the computational domain.

$$t_{c1} = L/U$$

But the acoustic waves propagate within the cavity at local sound speed, so we can define a second characteristic time as

$$t_{c2} = L/a = M t_{c1}$$

where a is the local sound speed. For reasons of economics, large time steps are desirable for the computations. However, if this time step is larger than t_{c2}, then we cannot capture the pressure fluctuations. Beside the numerical stability, therefore, there is another restriction to the numerical time step. We express that using the frequency

$$f_{CFD} > f_{pressure\ fluctuation}$$

and from the definition $f = 1/T$,

$$=> \quad t_{CFD} < t_{pressure\ fluctuation}$$

$$=> \quad t_{CFD} < min(\ t_{c1},\ t_{c2}\ )$$

A lot of time dependent data (pressure history) is obtained in the time domain. A widely used method is to transform this data from the time domain to the frequency domain using Fourier transforms. Compared with other methods, the frequency domain representation is much easier to understand and contains the information of harmonic resonance frequency directly.

The definition of Fourier transformation [61] is given as following:

$$F(w) = \int_{c}^{\tau} f(t) \exp(-iwt)\,dt \ . \tag{4.43}$$

There are two fluctuation mechanisms that occur in a cavity; a strong periodic fluctuation, and a random fluctuation. Since we cannot predict the period of a random fluctuation, we rewrite equation (4.43) as

$$F(w) = \int_{-}^{\cdot} f(t) \exp(-iwt)\, dt \ .$$
(4.44)

The acoustic pressure distributions are represented as overall sound pressure level, SPL, in decibels which is defined as

$$SPL(t) = 10 \log \left(\frac{\overline{p}^2}{p_r^2} \right).$$
(4.45)

where the value of reference pressure, P_r, is 2x10⁻⁶ Pascals. Then time distributions of SPL are transformed into frequency distributions using Fourier transformations for cyclic but non-periodic oscillations [60],

$$SPL(f) = \int_{t}^{\cdot} SPL(t) \exp(-2\pi f t i)\, dt \ .$$
(4.46)

where f is in Hertz (Hz).

Computed sound pressure levels are corrected by subtracting

$$10 \log_{10}(f_{CFD}/f_{experiment})$$
(4.47)

to account for the disparity between the computational band width increment, and the experimental band width increment.
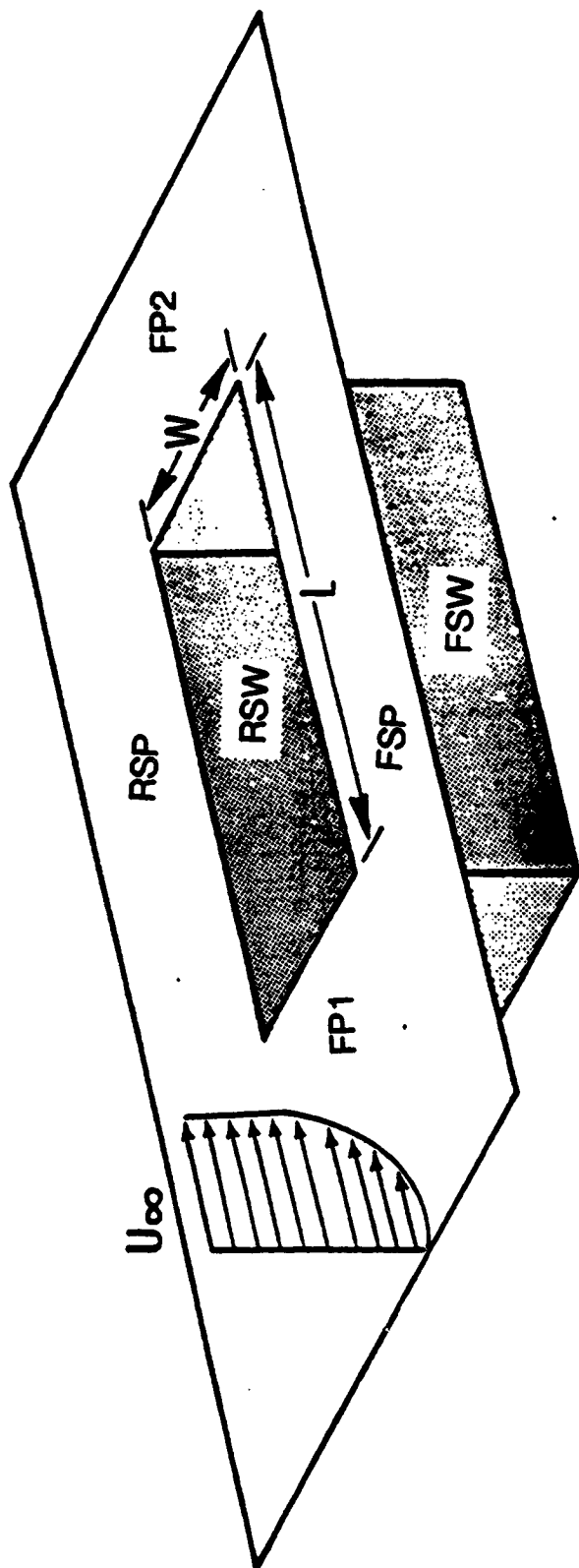
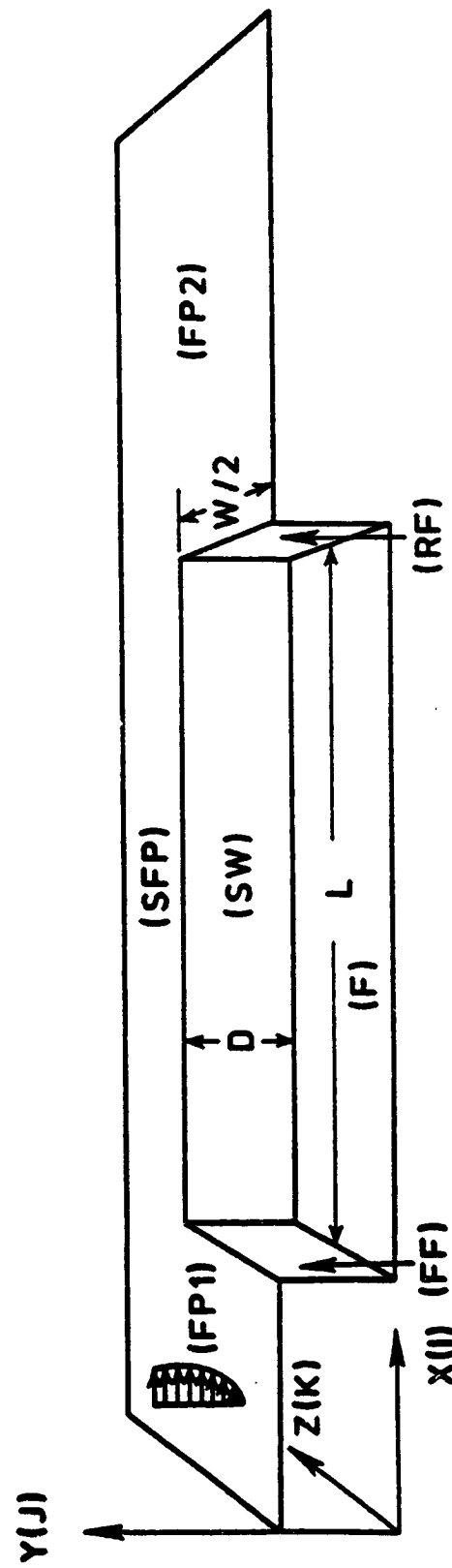4.1a Schematic of a full span rectangular cavity

Fig. 4.1b Schematic of a rectangular half span cavity

Chapter 5

RESULTS AND DISCUSSION

The computational test cases have been chosen in order to compare the flow structures with different flow conditions (with and without yaw angle), and the computational results of different schemes. Four cases have been modeled and analyzed.

Case 1: Mach = 2.16, L/D = 3.0, yaw = 0°, EMFD Scheme;

Case 2: Mach = 2.16, L/D = 3.0, yaw = 45°, EMFD Scheme;

Case 3: Mach = 1.65, L/D = 6.7, yaw = 0°, EMFD Scheme;

Case 4: Mach = 1.65, L/D = 6.7, yaw = 0° IUFV Scheme.

One of the reasons for choosing these test cases has been the availability of experimental data. Also, it is intended to demonstrate the capability of the numerical schemes to model the complicated flow features in different flow regions. The flow conditions and cavity specifications chosen for the four test cases are given in Table 5.1. The grid sizes used to represent a field size enclosing each cavity are shown in Table 5.2. The field dimensions and cavity dimensions are also shown in the X, Y, and Z directions for the test cases.

Since the flows being simulated are unsteady, global time stepping has been used in order to maintain the time accuracy. In order to stabilize the initial numerical transients, the time step has been gradually increased by increasing the Courant number form 0.01 to 0.7. Shown in Table 5.3 are the characteristic time and the computational schemes, the number of characteristic times over which each of the cases has been run, and the amount of CPU (Central Processing Unit) hours used for each case.

Presented in the figures illustrating these cases are the distributions of velocity vectors, density, Mach number, temperature, pressure and skin friction coefficients inside the cavity. In order to show the three-dimensional effects, the flow variables are plotted at different planes. In this study, these quantities are plotted in the streamwise, cross flow, and horizontal planes. Shown in figures 5.1a, b and c are representative diagrams of streamwise, cross flow, and horizontal planes.

The instantaneous streamline plots and the limiting streamline plots, which approximate the oil flow patterns in experiments, are also shown. The limiting streamline plots on the cavity floor have been obtained by limiting the particle traces to a plane just above the floor. In addition, to demonstrate the transient nature of the cavity flow, time series analysis of the pressure histories at certain locations on the floor and lip are displayed. The computational results have been restricted to several characteristic times.

5.1 Case 1: Mach=2.16, L/D=3, yaw=0o, EMFD Scheme

The entire velocity field over the cavity centerplane is shown in Fig. 5.2. Since the flow is time dependent, only a typical instantaneous velocity distribution is presented. The most obvious feature is that the shear layer bridges the cavity opening as expected of deep cavities. The shear layer sometimes dips into the cavity and sometimes it deflects out of the cavity. The flowfield within the cavity is subsonic. Experimental investigations also recorded an identical observation [14]. An attached turbulent boundary layer upstream of the cavity separates at the lip to form a free shear layer over the cavity and finally reattaches downstream of the cavity. Two distinct vortices are seen within the cavity. The interaction of the shear layer with the rear face causes a strong vortex structure close to the rear face. The vortex structure close to the front face is relatively weak. In addition to the main vortex

structures. For clarity, only every other velocity point in the streamwise direction has been plotted in all the velocity vector plots.

In order to demonstrate the unsteady and three-dimensional behavior of the flow, the velocity vectors within the cavity at different spanwise planes have been plotted in Fig.5.3 at two instants of time (t_{ci} = 40.4 and t_{ci} = 55.76). These velocity vectors are presented at four streamwise planes, moving from the plane of symmetry towards this sidewall, (Z/W = 0.1527, 0.2728, 0.3672, and 0.4415). It can be seen that the flow structure changes from one instant to the next. In addition to the variation with time, the spanwise variation is evident. The vortex structures near the front and rear faces appear to be warped as the side wall is approached.

The instantaneous (t_{ci} = 55.76) streamwise density contours at four planes (Z/W = 0.1527, 0.2728, 0.3672, and 0.4415) are displayed in Fig 5.4a. The shear layer is evident from these contours. The value of density at the front face region is low and progressively increases to a high value towards the rear face region. The reason for the increase in density at the rear face region is the interaction of the shear layer with the rear face and the compression of the fluid. This compression causes a free stream shock wave close to the rear face. Also, from Mach number contours, we can see the shear layer deflects out into the rear face region, and causes a shock wave in the freestream. The static temperature within the cavity is slightly higher than the freestream value, and the density in the cavity changes from a low value at the wall and increases progressively towards the cavity opening until it reaches the freestream value. The density decreases in magnitude from the plane of symmetry towards the sidewall. The streamwise pressure and Mach number contours are shown in Fig. 5.4b and 5.4c, respectively. The same trends observed in the density contours are seen in the pressure contours. The pressure contours exhibit shock structure weakening in magnitude from the plane of symmetry towards the sidewall.

The instantaneous streamline plots generated with "numerical dye injection" at different vertical planes, stretching from the floor vertically up to the shear layer region are displayed in Fig. 5.5a. The three-dimensional view of the instantaneous streamline within the cavity are depicted here. The flow inside the cavity consists of a large counterclockwise rotating vortex, and a smaller clockwise rotating vortex. We can get the details of the flow structure from Fig. 5.5a and Fig. 5.5b.

The instantaneous velocity vectors at three cross sectional planes (X/L = 0.0679, 0.6852, 0.9571) and two instants of time (t_{cl} = 40.4, 55.76) are shown in Fig. 5.6. It is seen that the flow structure is not only different at various cross sections but also varying with time. The cross flow velocity vectors (at t_{cl} = 55.76) at X/L = 0.0679, show the flow on the SFP to be towards the cavity forming one bigger clockwise rotating vortex, and a smaller counter rotating vortex. The air flow is from the side flat plate into cavity. The velocity vectors at X/L = 0.6852, and t_{cl} = 55.76 show the fluid is being pumped out from the cavity towards the side flat plate.

The instantaneous limiting streamline patterns on the cavity floor are displayed in Fig. 5.7a. Since the limiting streamline plots do not indicate the direction of the stresses, two components of the shear stress contours on the cavity floor (τ_{zx} and τ_{yz}) are plotted (Fig. 5.7b), and shear stress vectors at the same instant of time as Fig. 5.7c. The main flow interacts at the rear face and reattaches on the floor close to the rear face (Fig. 5.7a). The reattached flow moves in the direction of the front face. Towards the front face of the cavity, the limiting streamlines converge into a line of separation. There are several nodes and saddle points. This is an instantaneous open type separation. In addition to the main separation, there is secondary closed separation on front face. This separated flow is seen to reattach on the floor very close to the front face. In addition to the streamwise reattachment, a cross flow re-attachment of the flow is seen close to the sidewall. Close to the front face the

velocity components are small, therefore, the shear stress vectors are small. Since the shear layer interacts with the rear face, the magnitude of the velocity components are larger and therefore the shear stress vectors are larger. Due to the fluid particles are drawn towards the sidewall in the rear region of cavity, the low pressure region toward the sidewall. The shear stress contours are shown in Fig. 5.7b.

The mean pressure coefficient distribution along the cavity centerline and rear face, obtained computationally and experimentally [13], are shown in Figs. 5.8a through 5.8f. The specific locations are: (a) flat plate ahead of the cavity (FP1), (b) flat plate downstream of the cavity (FP2), (c) front face of the cavity (FF), (d) cavity floor (F), (e) rear face in vertical plane (RF), and (f) rear face in horizontal direction (FP2). In general, good agreement is seen between the computed and experimental data. The computed values of C_p on the rear face are lower than the experimental data. Also, the computed values of C_p on the cavity floor are slightly lower.

Discrepancies in the computational results can be attributed to the following reasons:

(1). turbulence model, (2). coarseness of the grids, (3). numerical truncation error, (4). explicit addition of artificial viscosity.

Shown in Fig. 5.9 are the frequency spectra of the overall sound pressure level at two locations along the cavity centerline, where data has been recorded. The pickup points are located in the cavity floor $X/L = 0.4$, and 0.8. From experimental observations [15], it is known that there are two resonant frequencies. A time series analysis in the frequency domain has been performed for histories of instantaneous pressure. The pressure data have been converted into sound-pressure level (SPL) in decibels (dB). The frequency domain has been plotted up to 1.2 megaHertz and compared with the experimental data. Basically, the computations predict the resonant frequencies, but cannot predict the SPL magnitudes accurately. The discrepancies in

the sound pressure level may be attributed to the relatively short periods of data collection.

5.2 Case 2 : Mach = 2.16, L/D = 3, yaw = 45⁰, EMFD Scheme

Because of the yaw angle, this is not a symmetric flow anymore. So we need to calculate the full cavity. In order to save the time for developing the flow, we used the primitive variables output file of Case 1 as the initial conditions of this case. We can envision the cavity flow with yaw to be a mixed type of two different L/D ratios; L/D=3 in the streamwise direction and W/D=5 in the crossflow direction.

The instantaneous velocity vectors (tc = 28.9) of longitudinal planes at four different spanwise locations, (Z/W = 0.0456, 0.6250, 0.8501, and 0.9783) are shown in Fig.5.10. From this figure, we can see a larger vortex and a smaller vortex within the cavity, which is a basic deep cavity structure. The instantaneous density contours (tc=28.9) at the same four spanwise locations are shown in Fig.5.11. The organized behavior of the shear layer is clearly seen as it bridges the cavity opening. The shear layer interacts at the rear face and causes a reversed flow within the cavity, resulting in a bigger vortex. At this instant, the density contours show that mass is being expelled at the cavity rear face. Due to the expulsion of mass, the shear layer is deflected up. There is a large region of separation on the rear flat plate (FP2). This is caused by the expansion around the sharp corner at the rear face. The variation of properties in the spanwise direction of Case 2 shows similarities to the typical structure of a deep cavity at yaw angle equal to zero.

Presented in Fig.5.12, are the instantaneous (t_{ci} = 28.9) cross flow velocity vector plots at four axial locations (X/D=0.2874, 0.8676, 2.5165, and 2.9391). At the X/D = 0.2874 location, the flow within the cavity is going in the reverse direction to the freestream, and form a smaller counterclockwise vortex close to the front side wall

(FSW, see Fig.4.1a). In the rear side wall, the flow dips into the cavity, and deflects out in the rear side of the cavity. The density contours of the cross flow are shown in Fig. 5.13. The shear layer is very stable near the front of the cavity, but there are a lot of fluctuations in the rear part of the cavity. We still can see the shear layer bridge the cavity. Pressure and Mach number contours are shown in Fig. 5.14 and Fig. 5.15. Both the longitudinal and the cross flow direction figures indicate the characteristics of a deep cavity.

The instantaneous (t_a = 28.9) particle traces limited to four streamwise planes (Z/W = 0.0456, 0.321, 0.85, and 0.3783) are displayed in Fig. 5.16. The formation of a larger vortex and two counter rotating vortices are evident from these figures. The particle traces limited to cross flow planes at five different locations (X/D = 0.2874, 0.8676, 1.7998, 2.5165, and 2.9391) are shown in Fig. 5.17. The particle traces at four different horizontal planes within the cavity (Y/D = 0.0276, 0.2323, 0.5, and 0.8936) are shown in Fig. 5.18. We can observe that shear layer brings in air mass and momentum. The particle traces are shown in Fig. 5.19. The shear layer first impinges on the rear face, then it deflects toward the rear side wall. It bends downward towards the cavity floor. A clockwise rotating vortex is formed within the cavity. From the top view, clockwise vortex is the main vortex direction. That is the most distinctive difference from the zero yaw angle cavity flow. In Case 1, the main vortex is predominantly in the vertical plane of the cavity. But in Case 2, the predominant plane of the main vortex inclines at a certain degree with the vertical plane. It is not only rotating in the streamwise direction but also in the horizontal plane.

The shear stress vectors and contours on the cavity floor are shown in Fig. 5.20a and Fig. 5.20b. As expected, the main concentration of the shear stress is at the downstream corner of the cavity.

5.3 Cases 3 and 4 : Mach=1.65, L/D=6.7, EMFD and IUFV Schemes

In an attempt to compare the solutions of the EMFD and IUFV schemes, Case 3 and Case 4 are discussed together. The major similar features between these cases are as follows: 1. the physical domain and the grid which covers it; 2. the governing equations of the flow; 3. the turbulence model; 4. initial and boundary conditions; 5. the physical elapsed times (up to two significant digits). The major nonsimilar features between these cases are the following: 1. the solution and discretization algorithms; 2. the manner in which the physical domain is mapped on to the computational domain, i.e., the evaluation of the coordinate transformation metrics and Jacobians; 3. the numerical dissipation, i.e., the artificial dissipation of EMFD versus the natural dissipation of IUFV; 4. although the total elapsed times are similar, the computational time steps which add up to the elapsed time are totally different; 5. 32-bit arithmetic (half-precision) of the CYBER-205 computer is used for the EMFD scheme, but 64-bit arithmetic of the CRAY-2 computer is used for the IUFV scheme.

A preliminary numerical study was conducted to determine the effects of eddy viscosity. First, a case was run without any eddy viscosity, i.e. as a laminar flow Then, the eddy viscosity was included in the computations only on the horizontal walls. Both of the test cases, predict the shear layer impinging on the cavity which is incorrect for open cavity flow. When the eddy viscosity is computed as modified as described in chapter 3, then the correct predictions are obtained.

The instantaneous(t_{el}=3.253) velocity vectors at two spanwise planes (Z/W=0.7881, 0.9764) of both cases are shown in Fig.5.21. In both cases, we can see a clockwise rotating vortex which dominates the cavity. The shear layer is clearly seen to bridge the cavity in both cases.

The density contours(t_{el}=3.253) of both cases in various spanwise planes are displayed in Fig.5.22. The density contours show that mass is being expelled at the

rear portion of the cavity. Due to the expulsion of mass, the shear layer is deflected up. We can see a shock generated at the rear face, and there is separation on the rear flat plate (FP2).

The instantaneous($t_{el}=3.253$) Mach number contours of both cases in various spanwise planes are shown in Fig.5.23. When the shear layer is deflected up in the rear portion of the cavity, we can see the vortices generated in the shear layer. The comparison of instantaneous streamlines($t_{el}=3.253$) in various planes of both cases are shown in Fig.5.24. We can see a big vortex within the cavity, and the shear layer is deflected out in the rear portion of the cavity. The instantaneous limiting streamlines($t_{el}=3.253$) on the cavity floor of both cases are shown in Fig.5.25. We can see the flow reattachment in the rear portion of the cavity. Then the flow is in the upstream direction, and finally, it separates on the front portion of the cavity. Also, we can see the three-dimensional separation lines in both cases. In Case 3, there is a very strong separation generated in the middle portion of the cavity.

From above figures we can understand that both schemes produce approximately similar flow structures in the cavity.

The instantaneous($t_{el}=12.875$) velocity vectors of longitudinal planes at two spanwise locations($Z/W=0.4857$, and 0.7881) are displayed in Fig.5.26. Note that these figures are for $t_{el}=12.875$, which is 9.6 characteristic times after the instant of Fig.5.21. The general flow structures are similar. A single vortex dominates the cavity. The shear layer interacts with the rear face and it deflects up. The density contours($t_{el}=12.875$) of the same spanwise locations as Fig.5.26 are shown in Fig.5.27. When the shear layer is deflected up, shock waves are generated in the rear portion of the cavity.

The instantaneous (t_{el} = 12.875) total pressure contours of longit.dinal planes at various spanwise locations (Z/W=0., 0.3486, 0.6027, 0.7327) of both cases are shown in

Fig.5.28. The vortex cells are seen to exist in the shear layer. The discontinuous vortex is distributed from the lip of front face to the rear face. As, we also can see from the density contours at two different instants, that is $t_{ci} = 3.253$ (Fig.5.22) and $t_{ci} = 12.875$ (Fig.5.27), the vortex cells change their positions. Some vortices are above the shear layer towards the rear of the cavity. So, we can conclude that there is vortex shedding phenomena existing in the shear layer in both cases. That is, it dips into the cavity and brings mass with it. Then it bridges the cavity for a few instants with no mass entrainment between the internal and external flows. Finally, when the shear layer deflects up to open the cavity, vortices are shed from the cavity to outside. This phenomenon is confirmed by the solutions of both schemes as evidenced with the total pressure contours and density contours. Hence it is concluded that the vortex shedding phenomenon captured here computationally is a physical one.

The time averaged pressure coefficients from both solutions are shown in Fig.5.29. The plotted Cp distributions are for the cavity floor centerline, the centerline on the rear face, spanwise distributions on the cavity floor and the rear face, and the longitudinal direction on the side wall. Generally they show good agreement with the experimental data. The predictions of the IUFV method are slightly better than those of the EMFD method.

The maximum stable time step for the IUFV code (7.48×10^{-7}) is approximately 1.7 times that of the EMFD code (4.39×10^{-7}). This comparison is for the solutions advanced to the same characteristic time. However, each time step computation with the IUFV code takes significantly more computer time than the EMFD code. Therefore, a better comparison can be made as follows. The EMFD code needs 4 megawords computer memory, and 5.68 CPU hours for each characteristic time. The IUFV code needs approximately 10 megawords computer memory, and 4.31 CPU hours for each characteristic time. That is, the IUFV scheme is approximately 30% faster but it

requires 2.5 times more computer memory. Note that the maximum time step (10^{-4}) is at least one order of magnitude smaller than the characteristic times t_{c1} (1.5×10^{-3}) and t_{c2} (9.1×10^{-4}). This is necessary to capture the physical fluctuations with the numerical time accurate solution advancing.

Table 5.1. Test conditions for the four cases

Case No.	Mach (M) number	T in K static	Re/meter in million	P in Pa static	yaw angle	Depth in m	Width in m	Length in m
1	2.16	168.1	6.56	6430.8	0	.0127	.0635	.0381
2	2.16	168.1	6.56	6430.8	45^0	.0127	.0635	.0381
3	1.65	210.3	6.56	11425	0	.1108	.0727	.7458
4	1.65	210.3	6.56	11425	0	.1108	.0727	.7458

Table 5.2. Cavity dimensions and computational grid size

Case No.	Grid Size			Field Dimensions			Cavity Dimensions			Block
	X	Y	Z	X	Y	Z	X	Y	Z	
1	97	60	36	.1076	.0587	.0512	.0127	.03175	.0381	
2	97	60	71	.1076	.0587	.1024	.0127	.0635	.0381	
3	120	63	28	.1076	.3753	.1163	.7458	.1108	.0727	
4	28	120	27	.1163	1.189	.3753				1
	20	91	37	.0727	.7458	.1108	.0727	.7458	.1108	2

Table 5.3 Computational time requirements

	t_{c1} characteristic time in millisecond	number of tc run	CPU hours	computer
1	.0679	56	24.63	Cyber 205
2	.0679	28.9	25.61	Cyber 205
3	1.5550	12.875	73.12	Cyber 205
4	1.5550	12.875	48.6	Cray 2
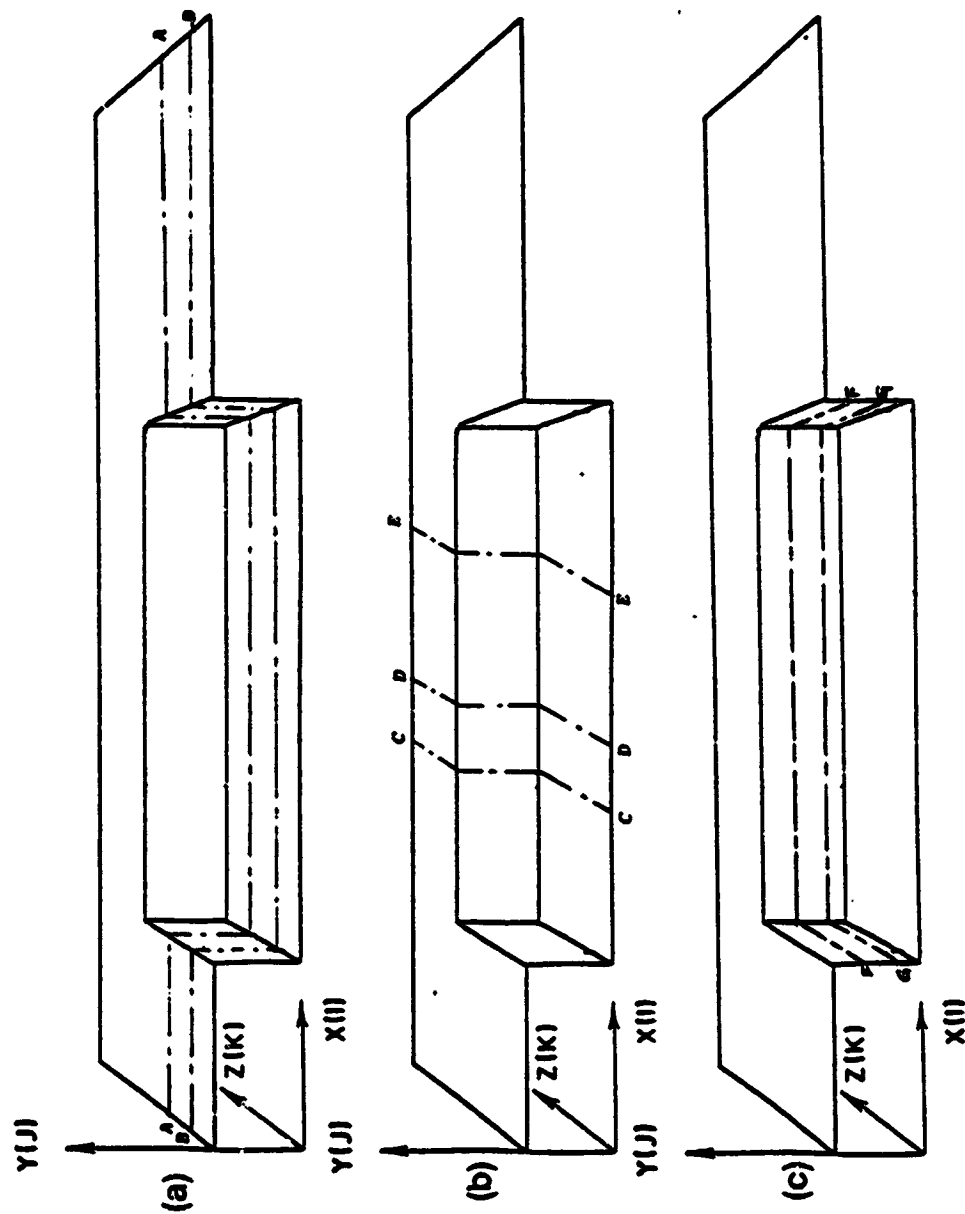
Fig. 5.1 Schematic of a cavity showing the location of (a) streamwise plane cut
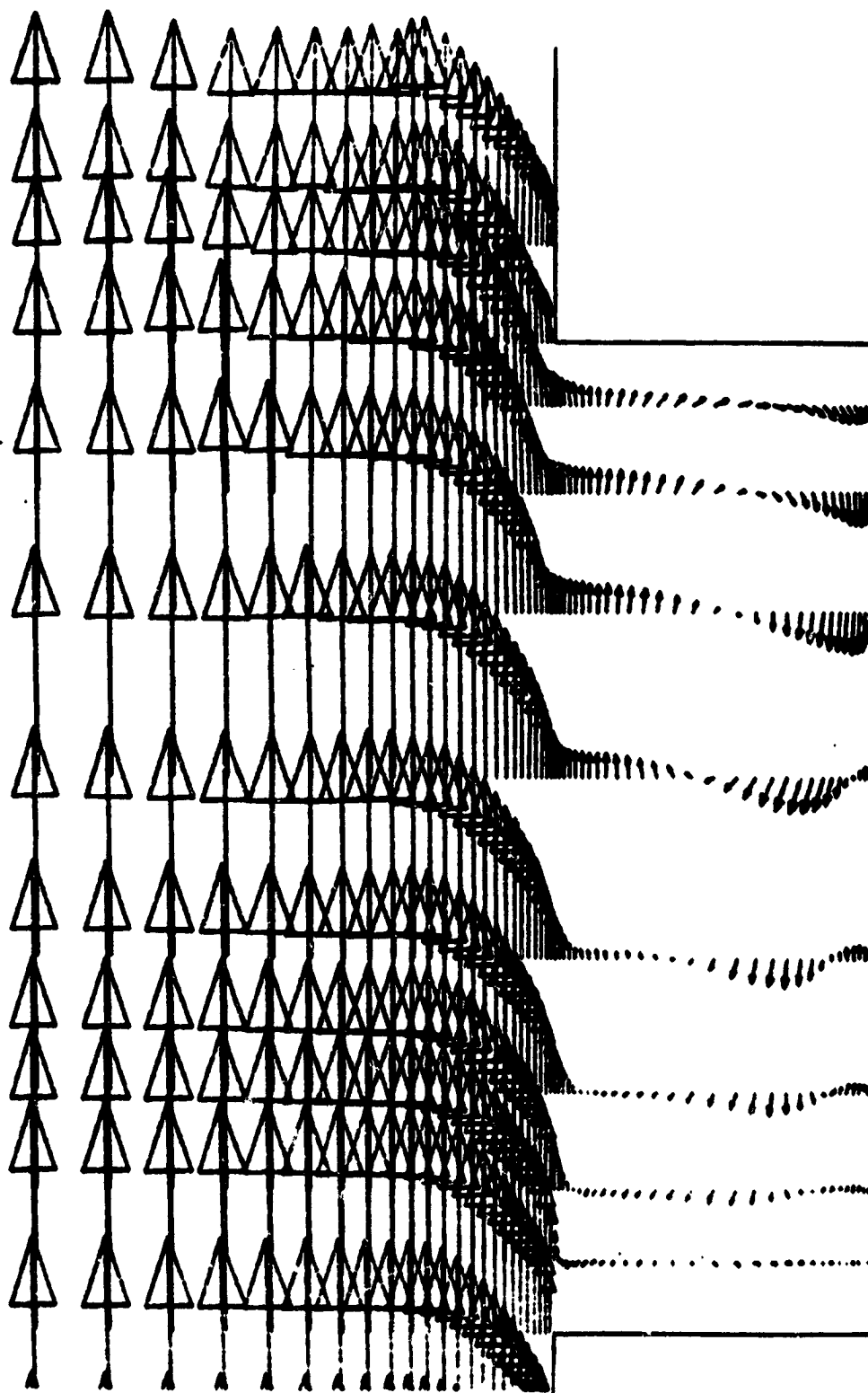
(b) cross flow plane cut (c) horizontal plane cut

62

Fig. 5.2 Instantaneous streamwise velocity vectors along the cavity centerline.
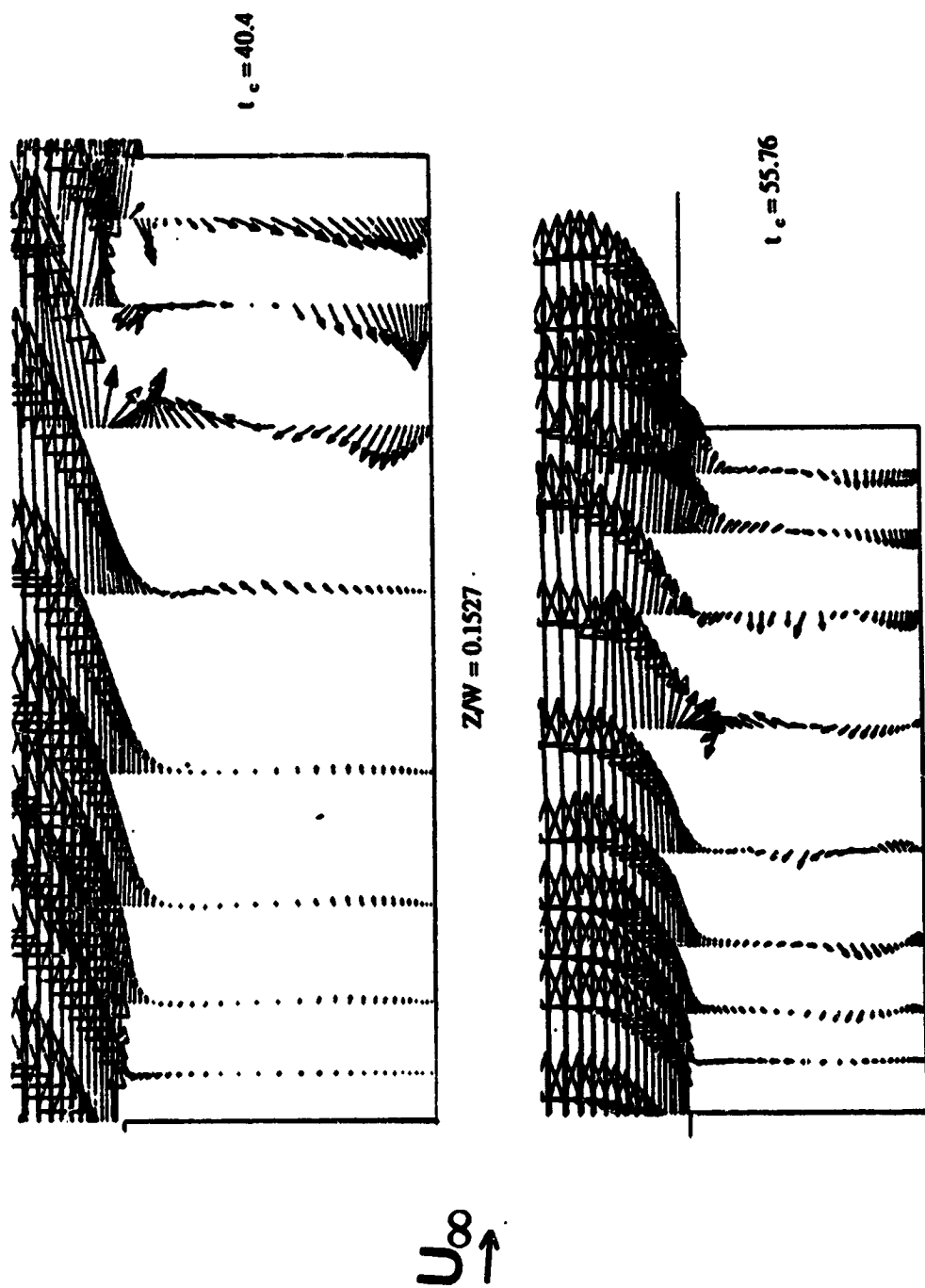
$t_c = 40.4$

$Z/W = 0.1527$

$t_c = 55.76$

U_∞

Fig. 5.3   Instantaneous streamwise velocity vectors at various spanwise planes

$Z/W = 0.2728$

$t_c = 40.4$

$t_c = 55.76$

$U_\infty \uparrow$

Fig.5.3 continued

$Z/W = 0.3672$

$t_c = 40.4$

$t_c = 55.76$

$\bigcup_\infty^0$

Fig.5.3 continued

$t_c = 40.4$

$t_c = 55.76$

$Z/W = 0.4415$

Fig.5.3 concluded

68

U_∞

Z/W = 0.4415

CONTOUR FROM .53570 TO 1.1235
CONTOUR INTERVAL IS .20162E-01

Z/W = 0.3672

CONTOUR FROM .51984 TO 1.1537
CONTOUR INTERVAL IS .30362E-01

Z/W = 0.2728

CONTOUR FROM .51681 TO 1.1187
CONTOUR INTERVAL IS .28673E-01

Z/W = 0.1527

CONTOUR FROM .94338 TO 1.1044
CONTOUR INTERVAL IS .38293E-01
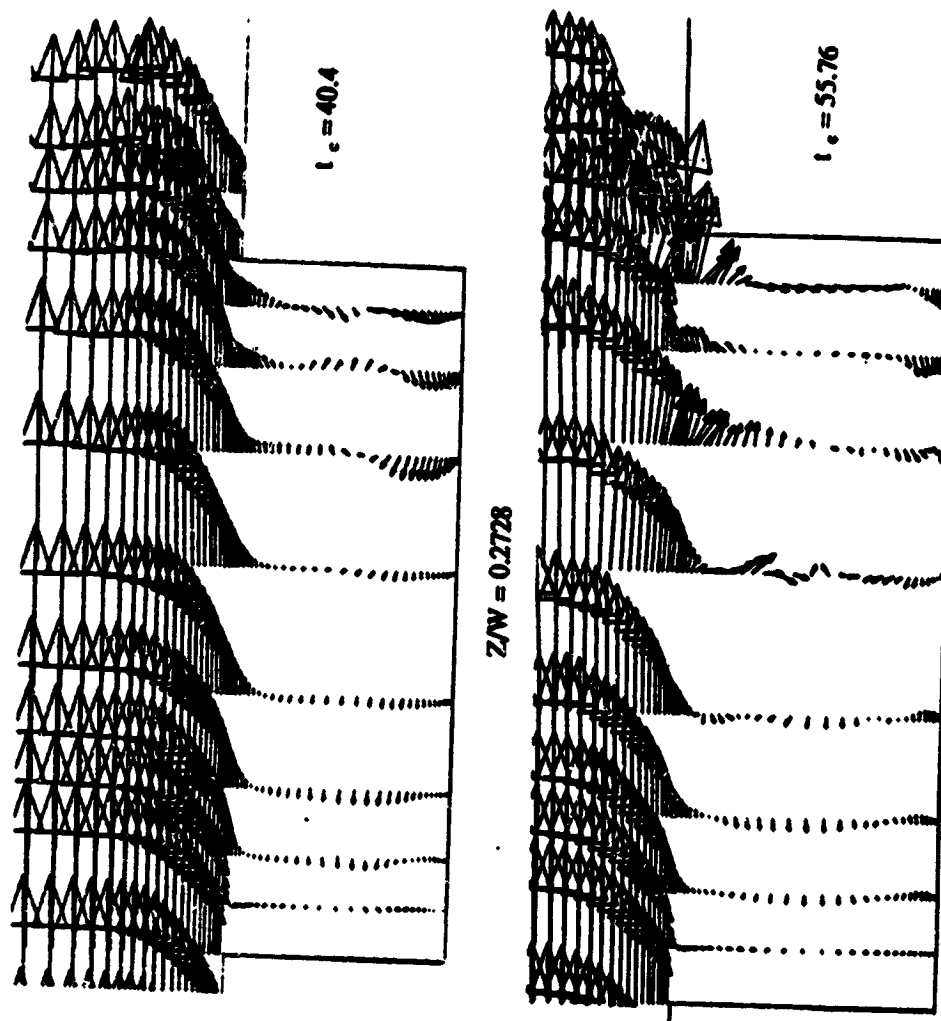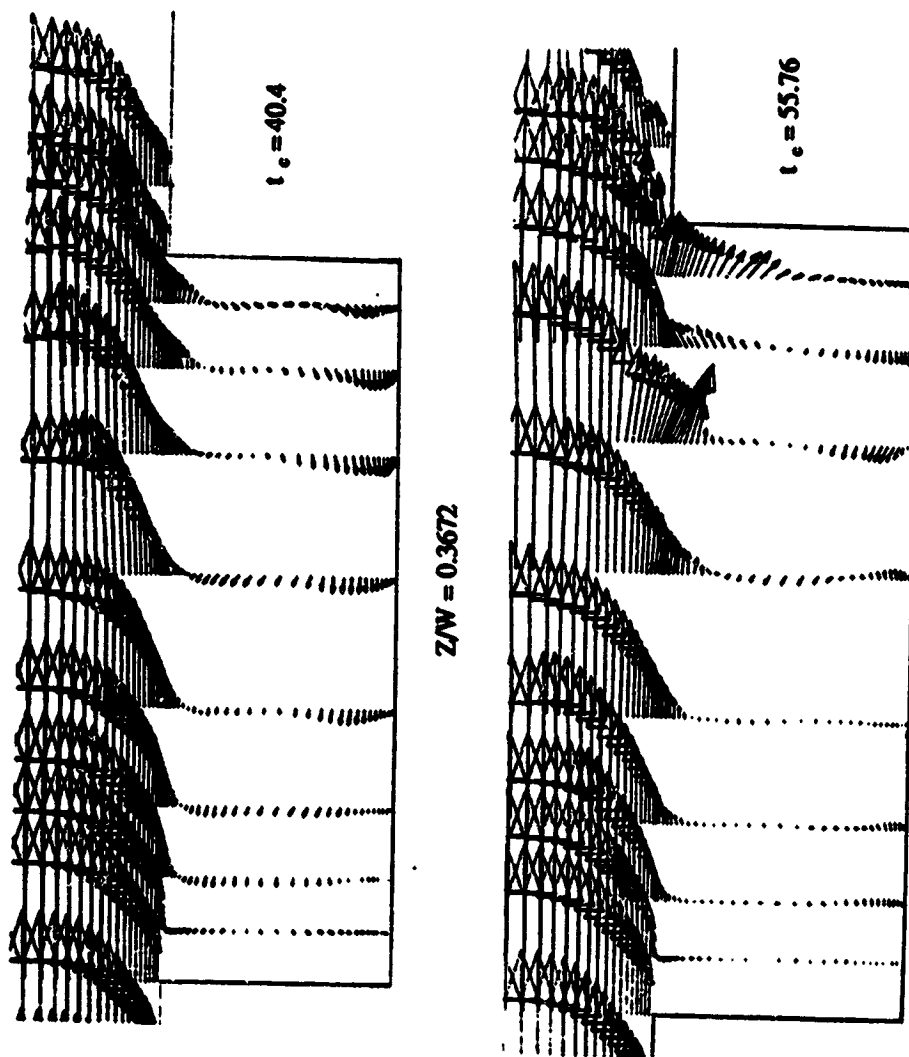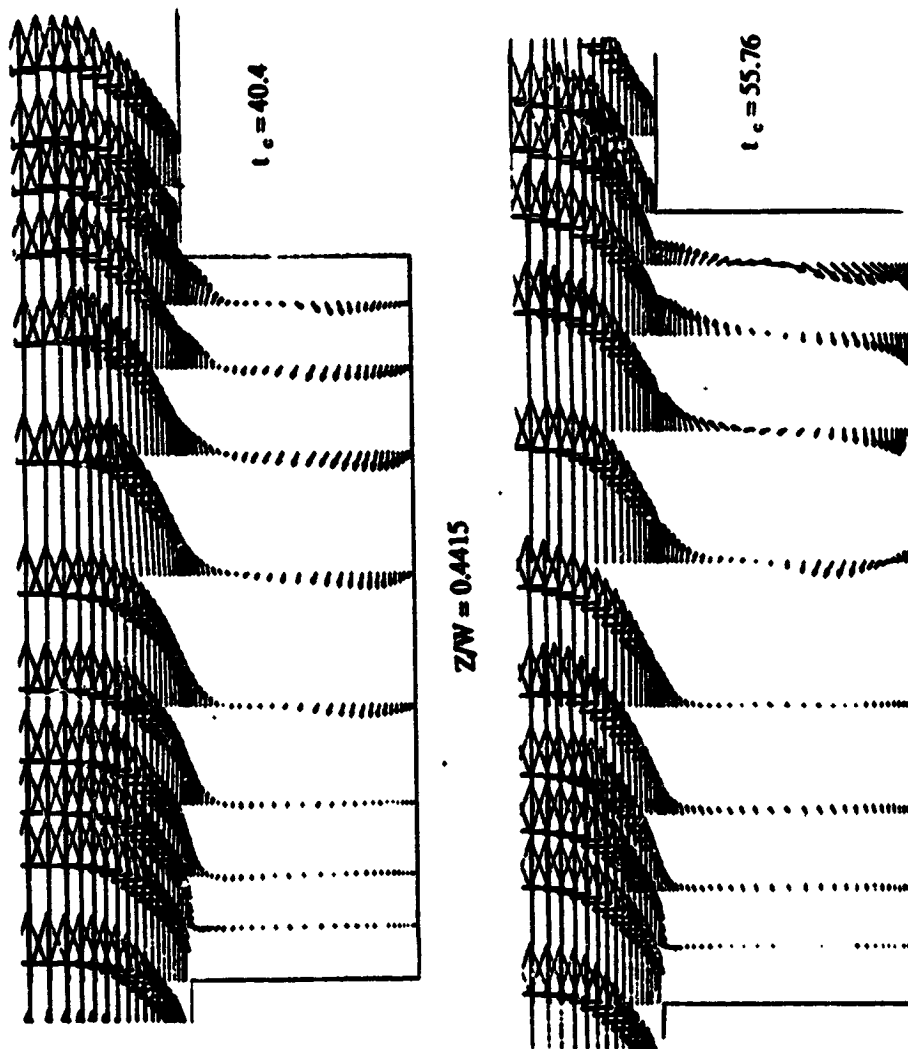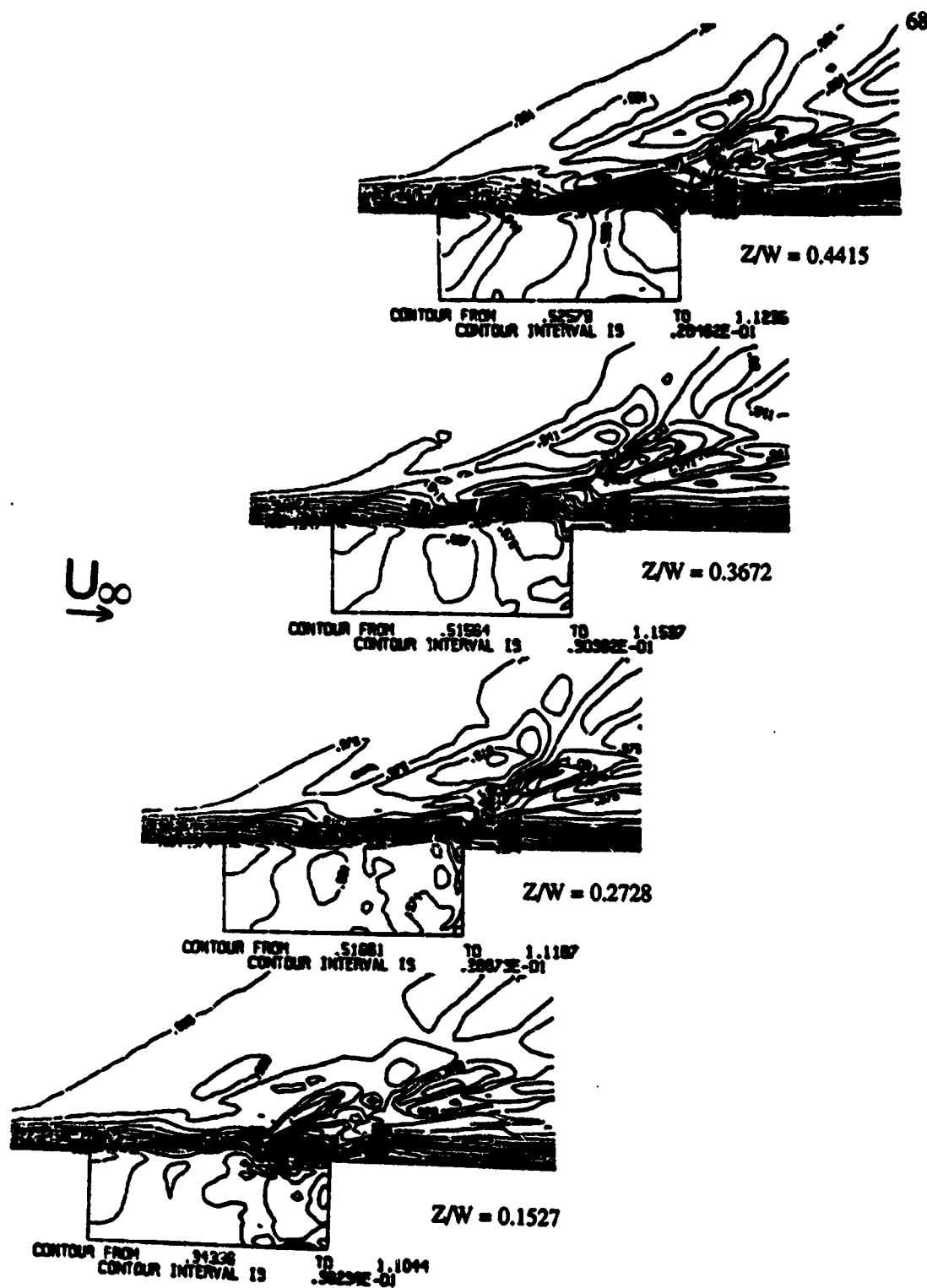
Fig. 5.4a   Instantaneous density contours at various spanwise planes

U_∞
→

Z/W = 0.4415

CONTOUR FROM   .80486   TO   1.3044
   CONTOUR INTERVAL IS   .25216E-01

Z/W = 0.3672

CONTOUR FROM   .82090   TO   1.2220
   CONTOUR INTERVAL IS   .19115E-01

Z/W = 0.2728

CONTOUR FROM   .82438   TO   1.1815
   CONTOUR INTERVAL IS   .17008E-01

Z/W = 0.1527

CONTOUR FROM   .40630   TO   1.5080
   CONTOUR INTERVAL IS   .32511E-01
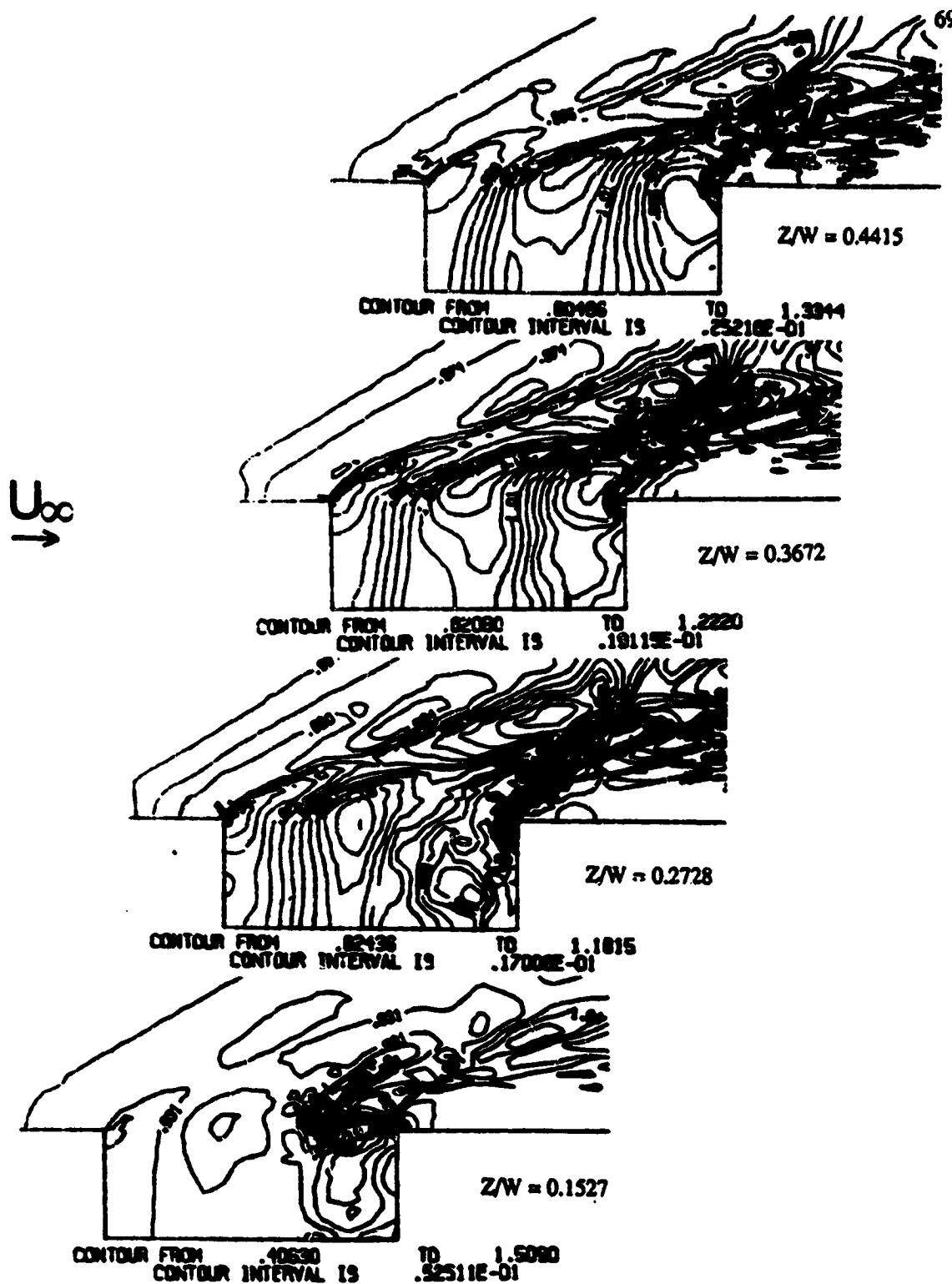
Fig. 5.4b   Instantaneous pressure contours at various spanwise planes

U_∞
$\rightarrow$

Z/W = 0.4415

CONTOUR FROM   0.   TO   2.2030
        CONTOUR INTERVAL IS   .10871

Z/W = 0.3672

CONTOUR FROM   0.   TO   2.2031
        CONTOUR INTERVAL IS   .10900

Z/W = 0.2728

CONTOUR FROM   0.   TO   2.2011
        CONTOUR INTERVAL IS   .10882

Z/W = 0.1527

CONTOUR FROM   0.   TO   2.4530
        CONTOUR INTERVAL IS   .11081
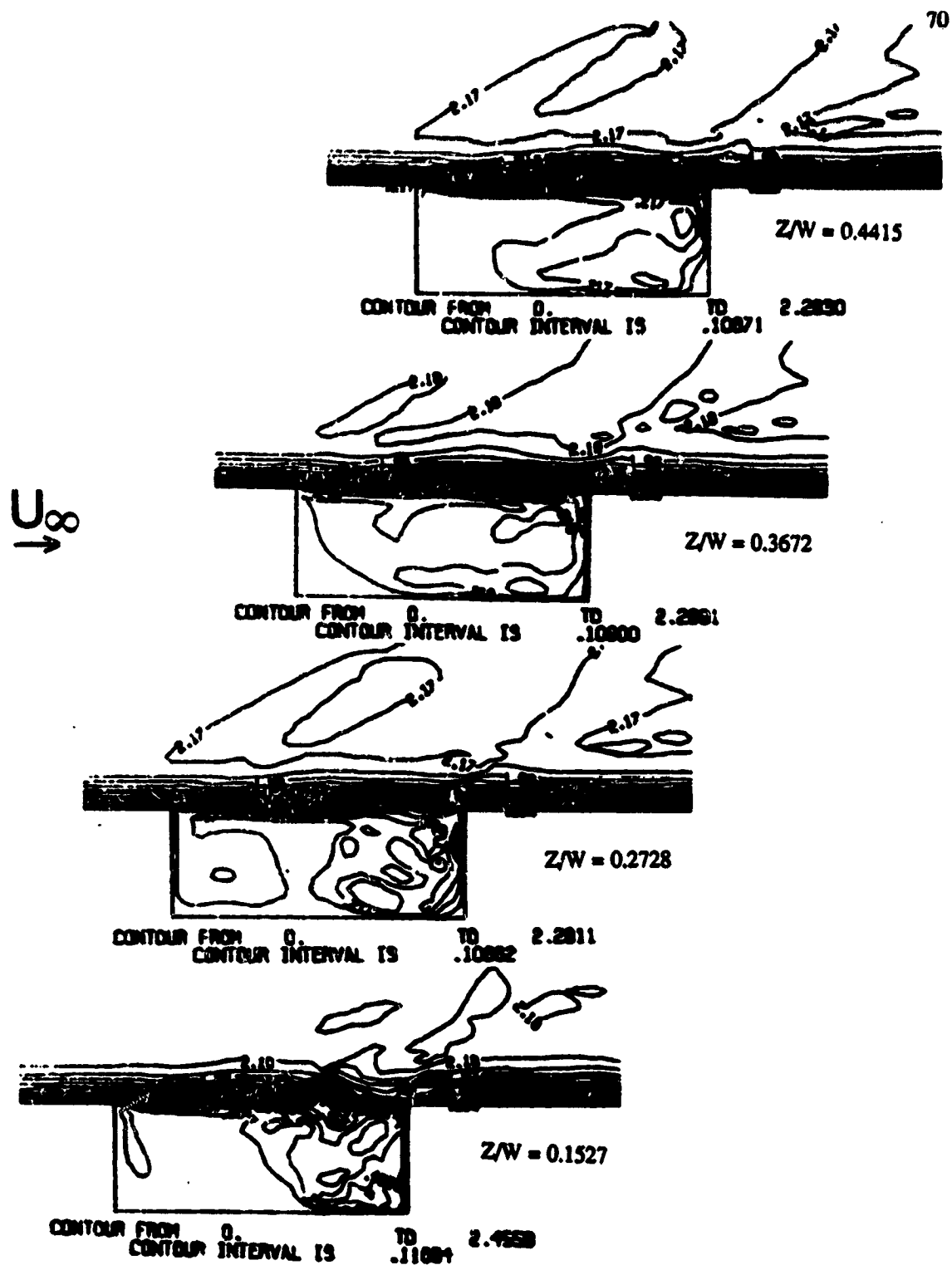
Fig. 5.4c   Instantaneous Mach number contours at various spanwise planes

Z/W = 0.4415

Z/W = 0.3672

Z/W = 0.2728

Z/W = 0.1527

U_∞
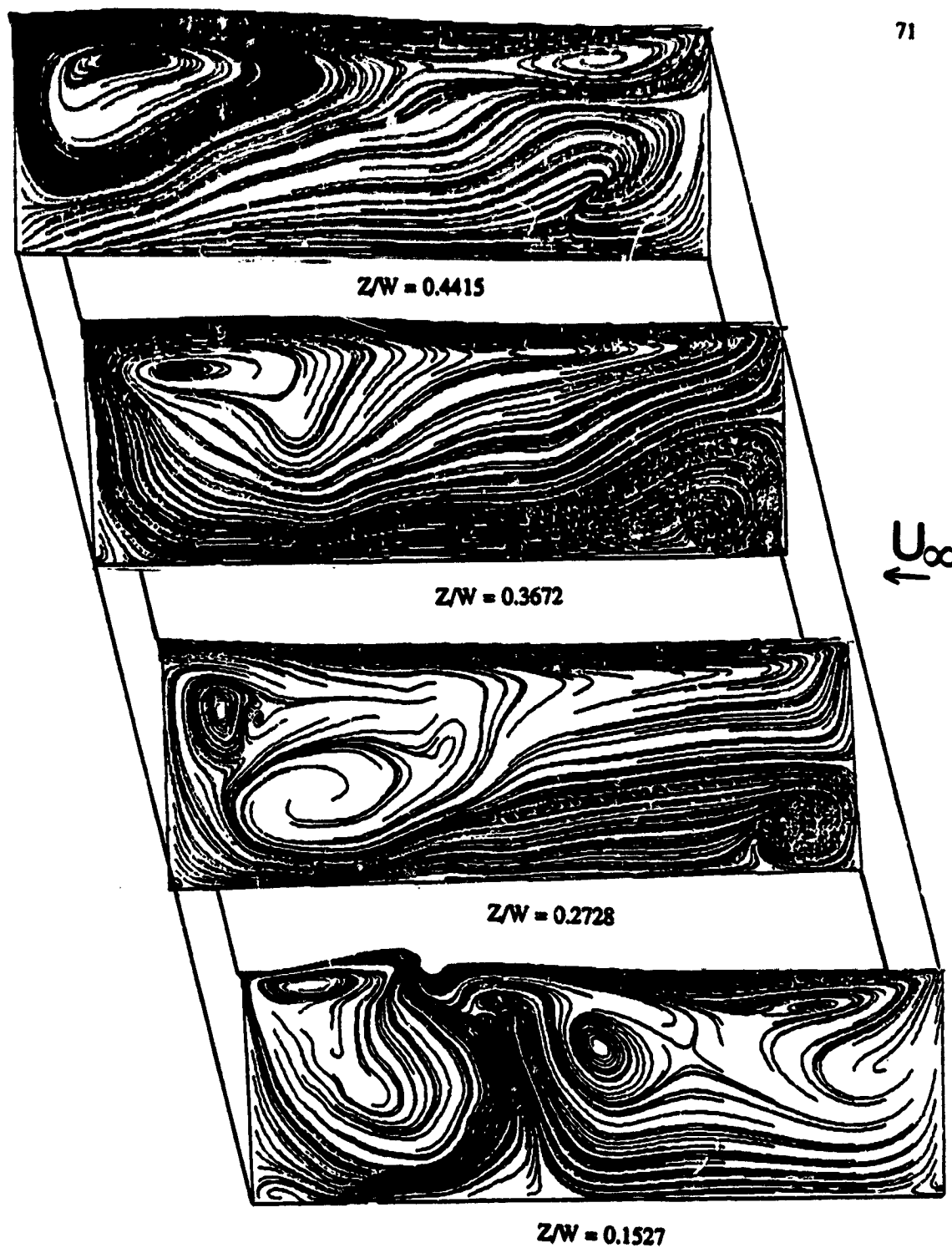
Fig. 5.5a   Instantaneous streamline pattern at various spanwise planes

U∞

FP1

FP2
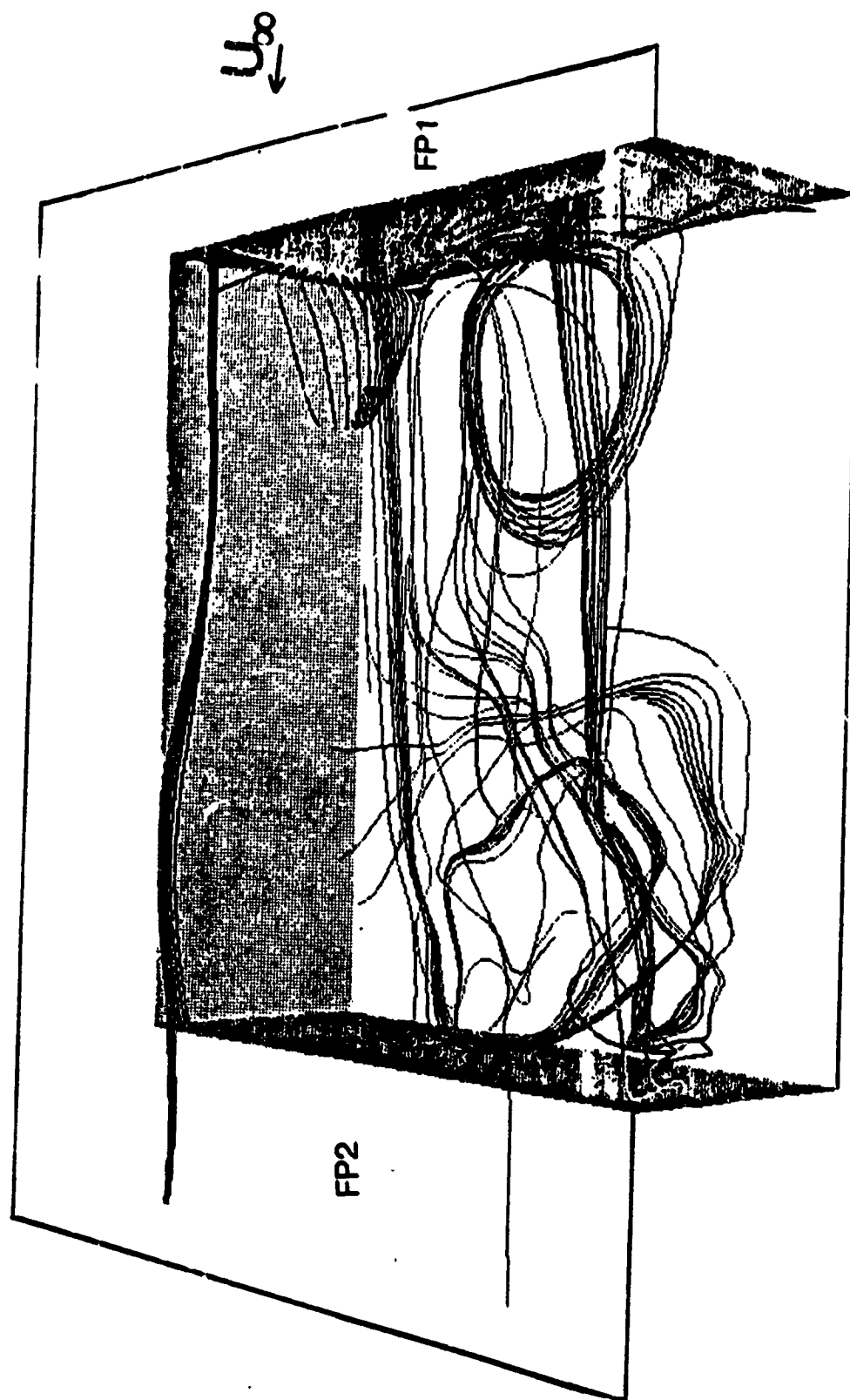
Fig. 5.5b Instantaneous streamline pattern within the cavity
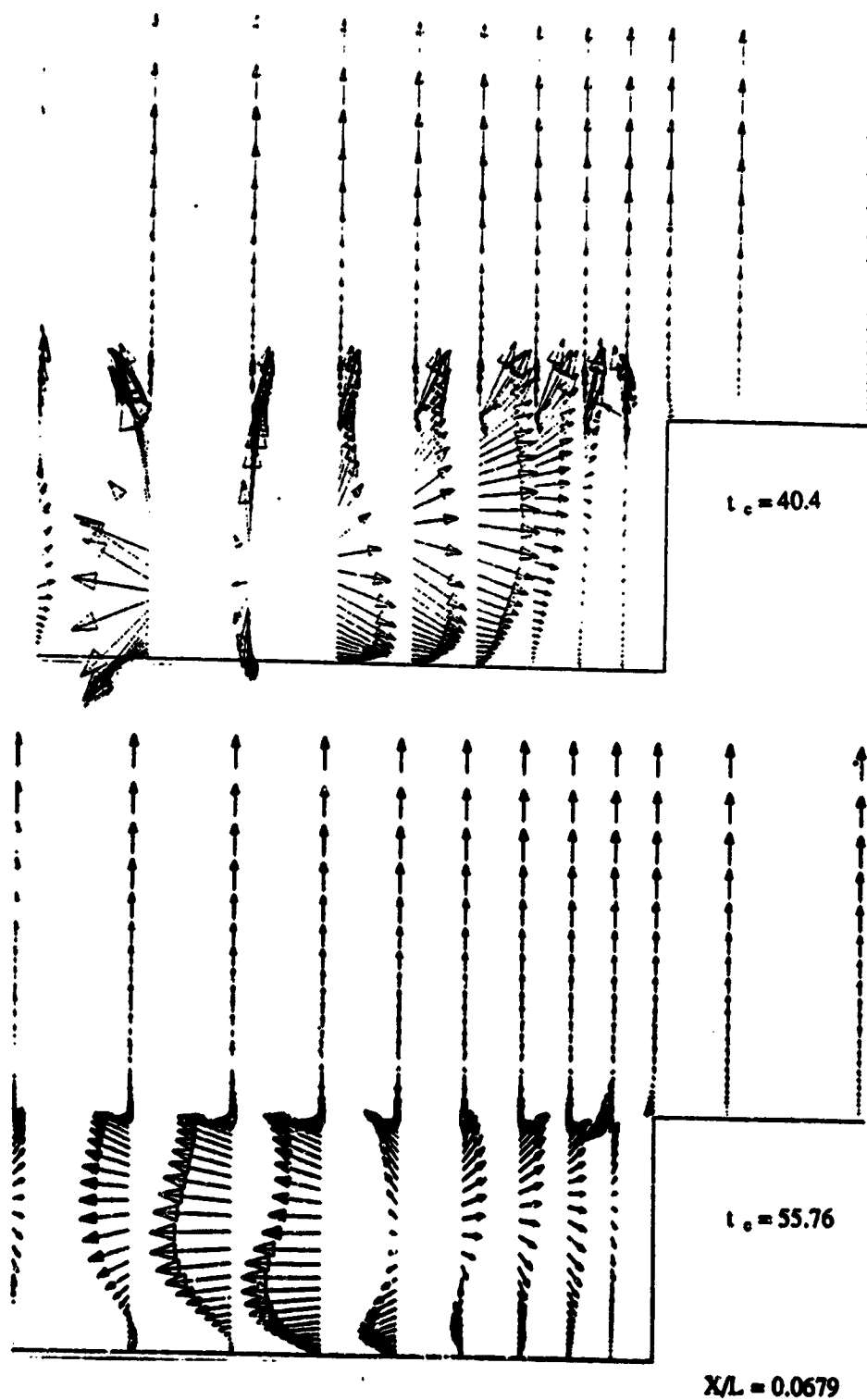
t_c = 40.4

t_c = 55.76

X/L = 0.0679

Fig. 5.6   Instantaneous velocity vectors at various cross flow planes

$t_e = 40.4$

$t_e = 55.76$

$X/L = 0.6852$

Fig.5.6   continued

$t_c = 40.4$

$t_c = 55.76$

X/L = 0.9571

Fig.5.6 concluded

SIDE WALL

(a)

U_∞

(b) U_∞

CONTOUR FROM   0   TO   23.003
        CONTOUR INTERVAL IS   1.2192

STRESS CONTOUR MACH=2.10 RE=0.003

(c) U_∞
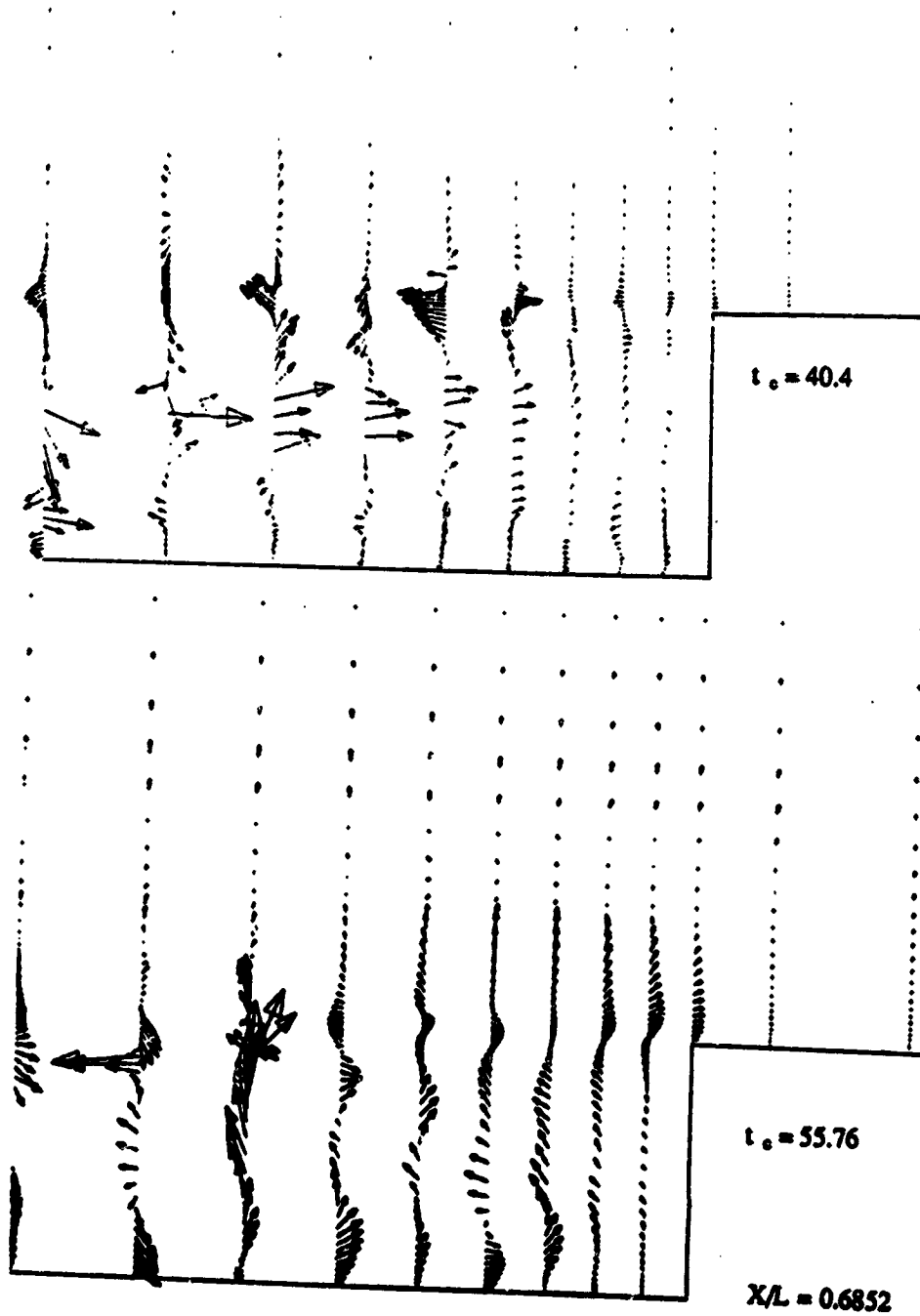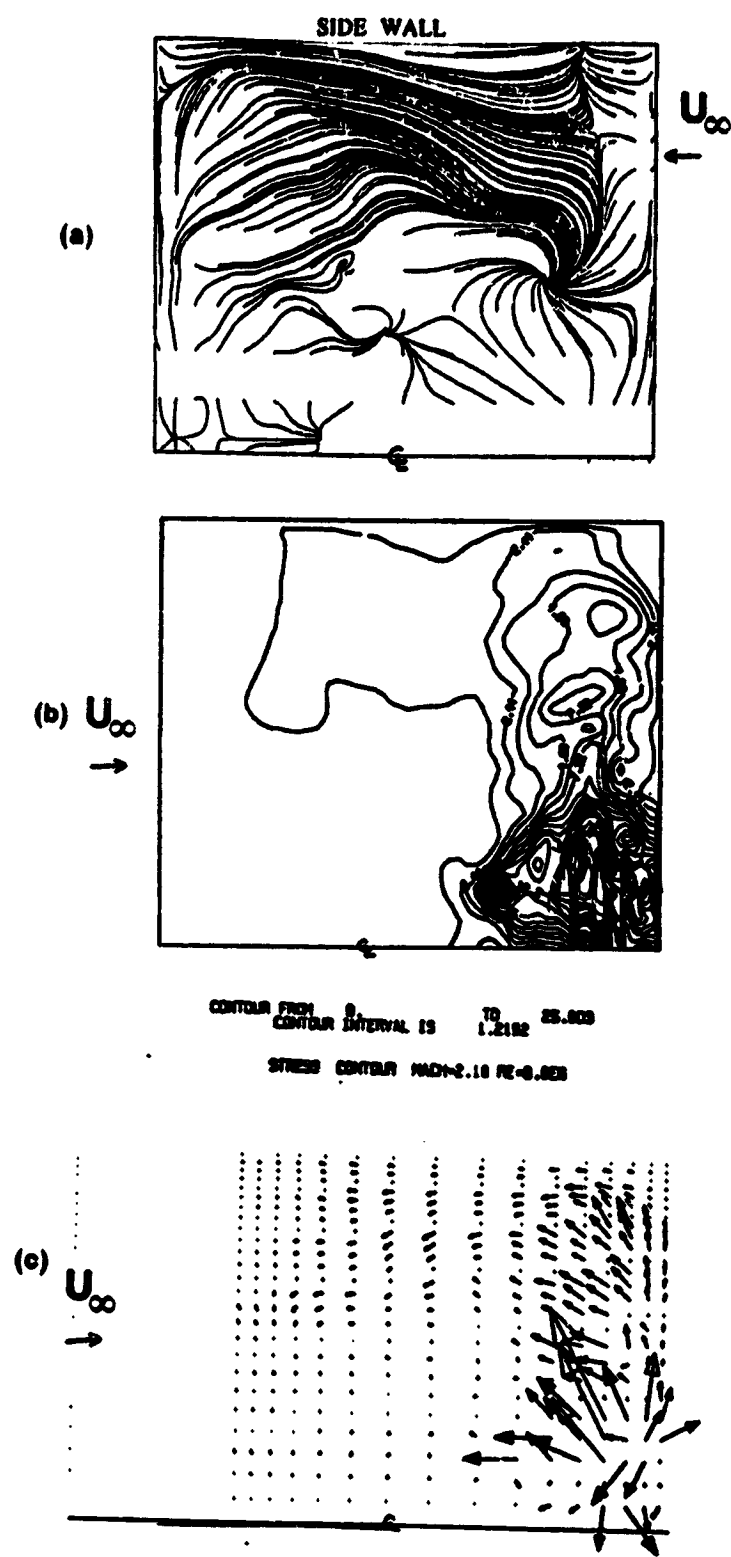
Fig. 5.7 LIMITING STREAMLINES SHEAR STRESS CONTOURS, AND SHEAR STRESS VECTORS ON THE FLOOR OF L/D = 3.0 CAVITY
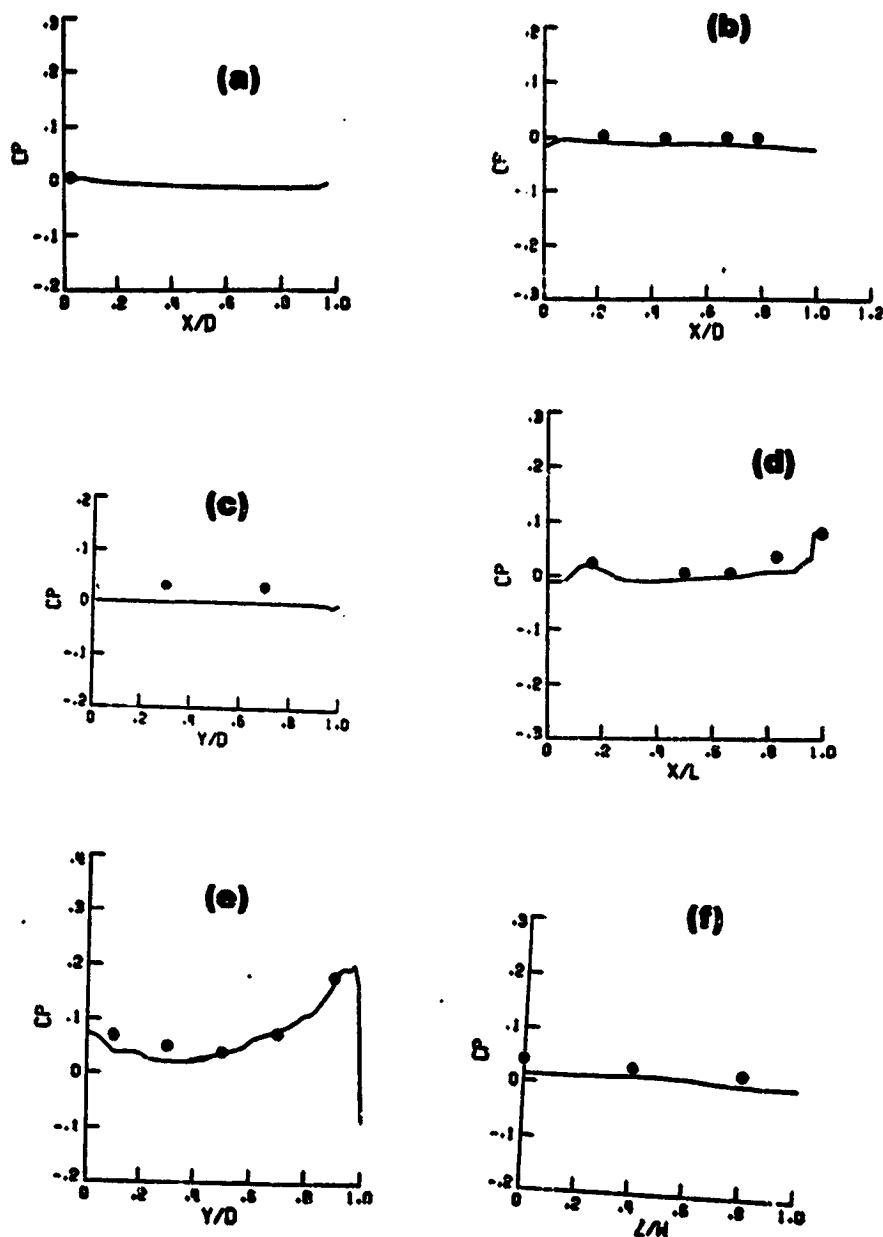
Fig.5.8 Time averaged pressure coefficients on
(a) flat plate 1; (b) flat plate 2;
(c) front face; (d) cavity floor;
(e) rear face in vertical direction;
(f) rear face in horizontal direction.
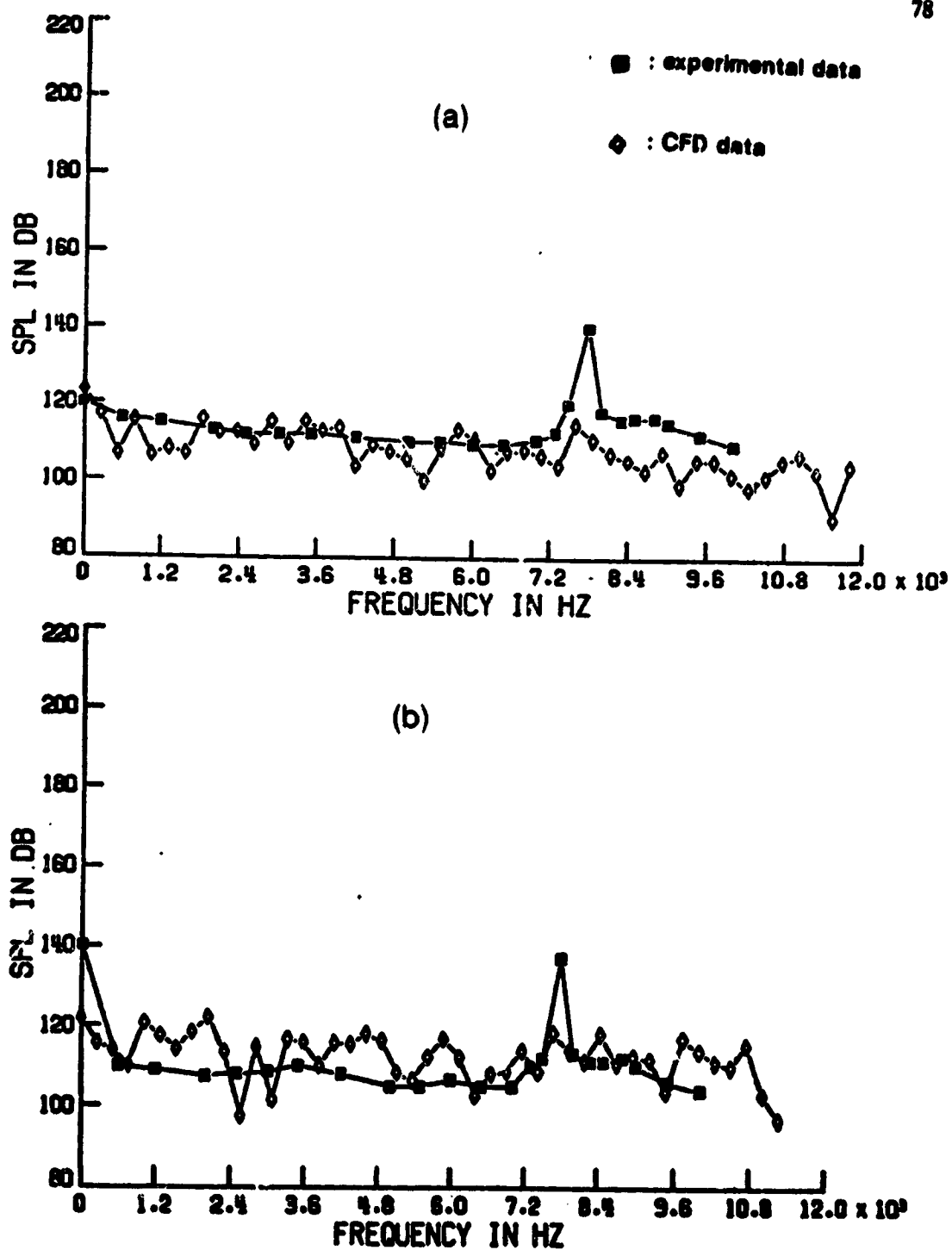
Fig. 5.9 Frequency spectra of sound level on the cavity floor (a). X/L = 0.4, (b). X/L = 0.8 .

Z/W = 0.0456

Z/W = 0.6250
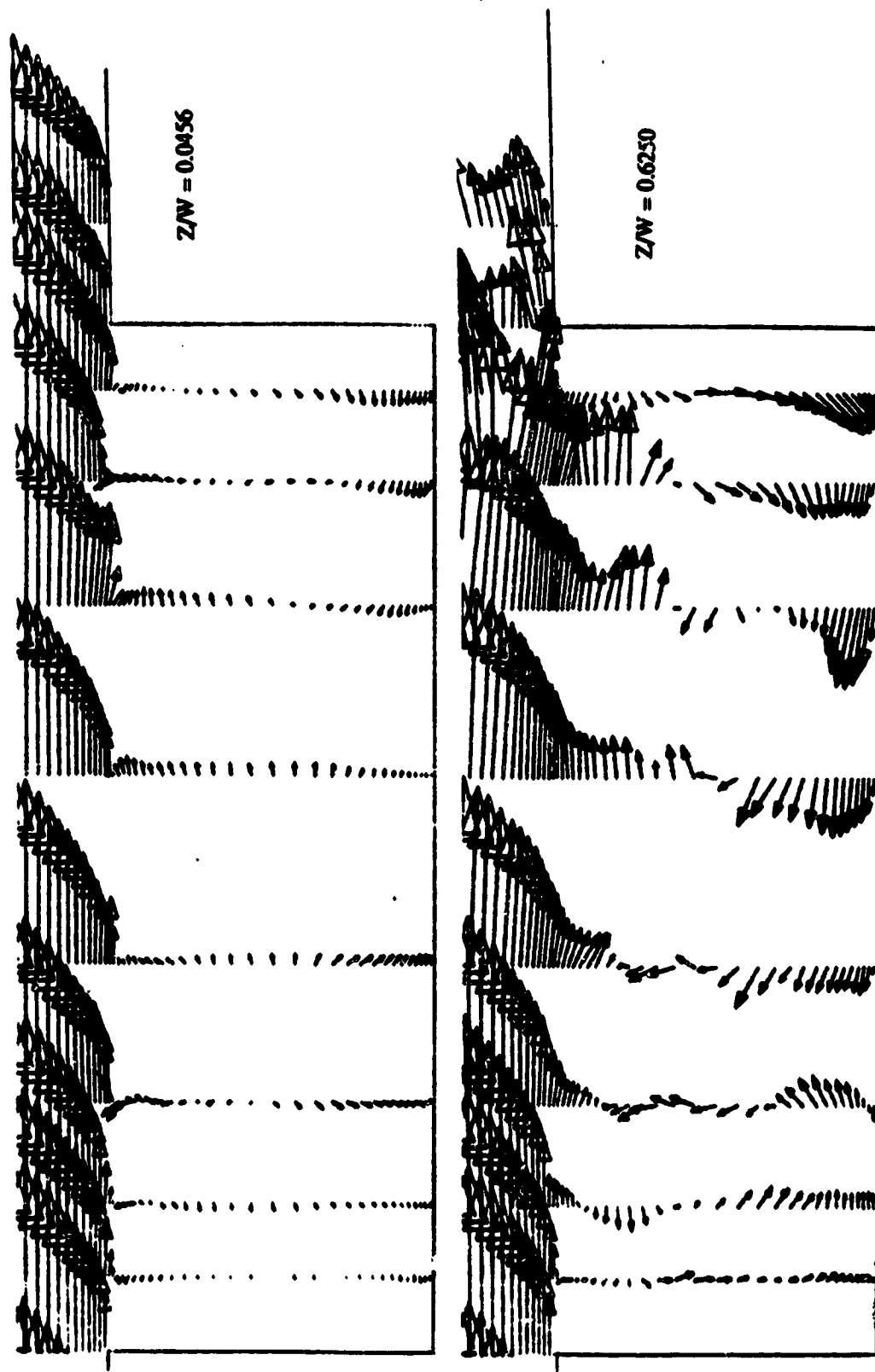
Fig. 5.10 Instantaneous velocity vectors at various spanwise planes

Z/W = 0.8501

Z/W = 0.9783

Fig.5.10 concluded

Z/W=0.9783
Min : .44044 Max : 1.1669 int : 0.025

Z/W=0.8501
Min : .49251 Max : 1.2546 int : .036

Z/W=0.6250
Min : .2884 Max : 1.0669 int : .037

Z/W=0.0456
Min : .53647 Max : 1.0002 int : .022

U_∞ 46°
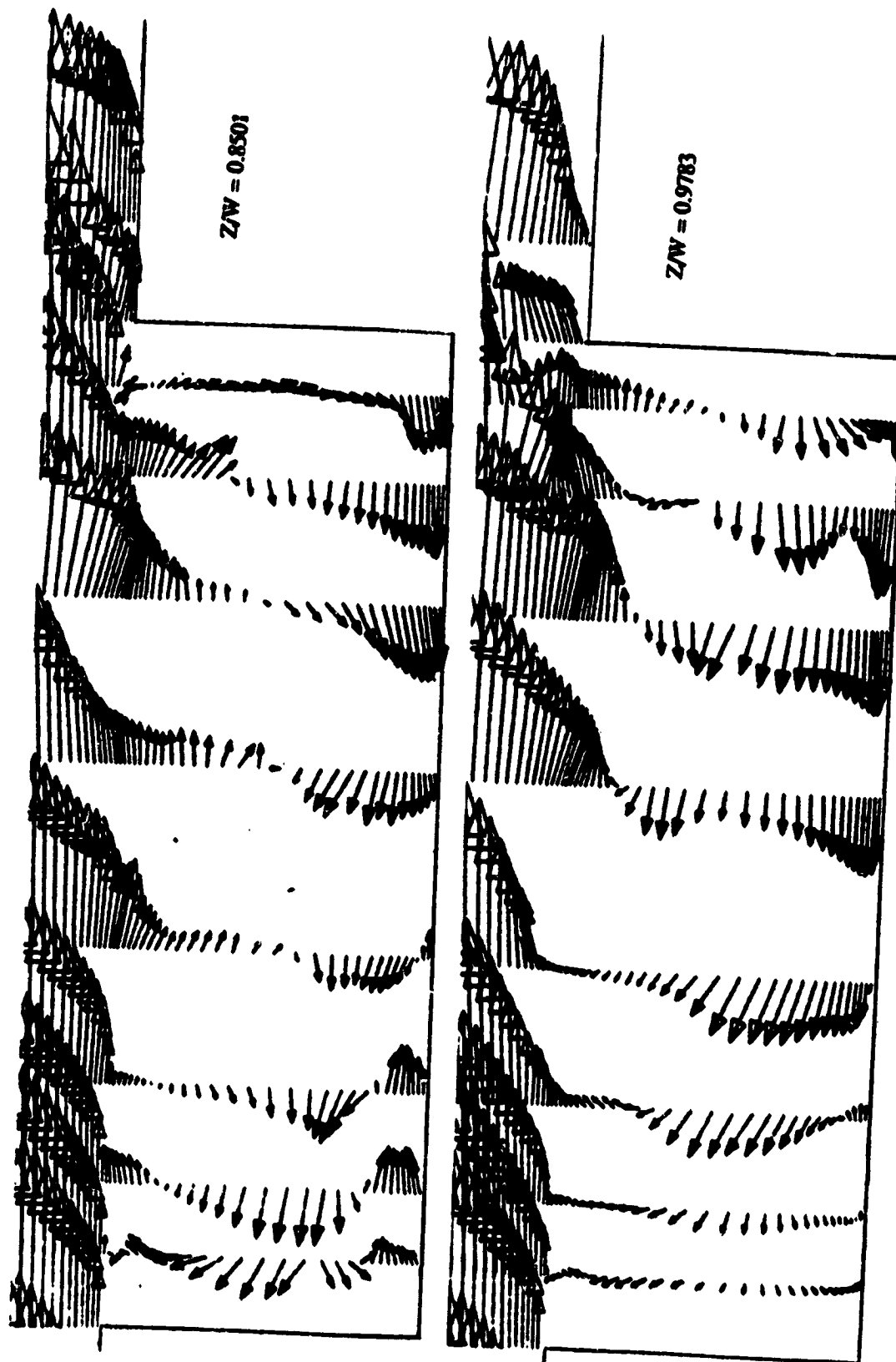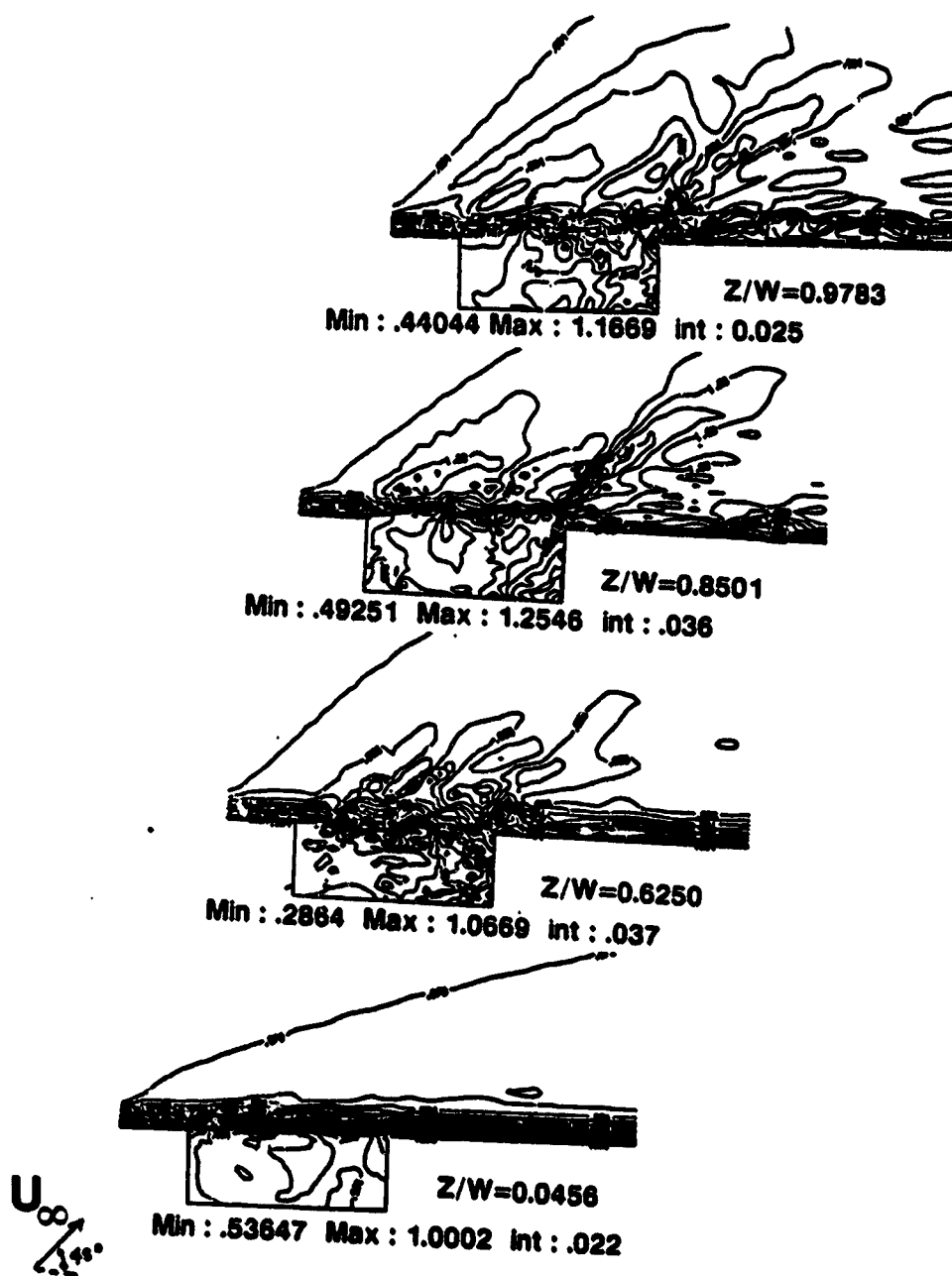
Fig.5.11 Instantaneous contours of density at various spanwise planes

X/D = 0.2874

X/D = 0.8676
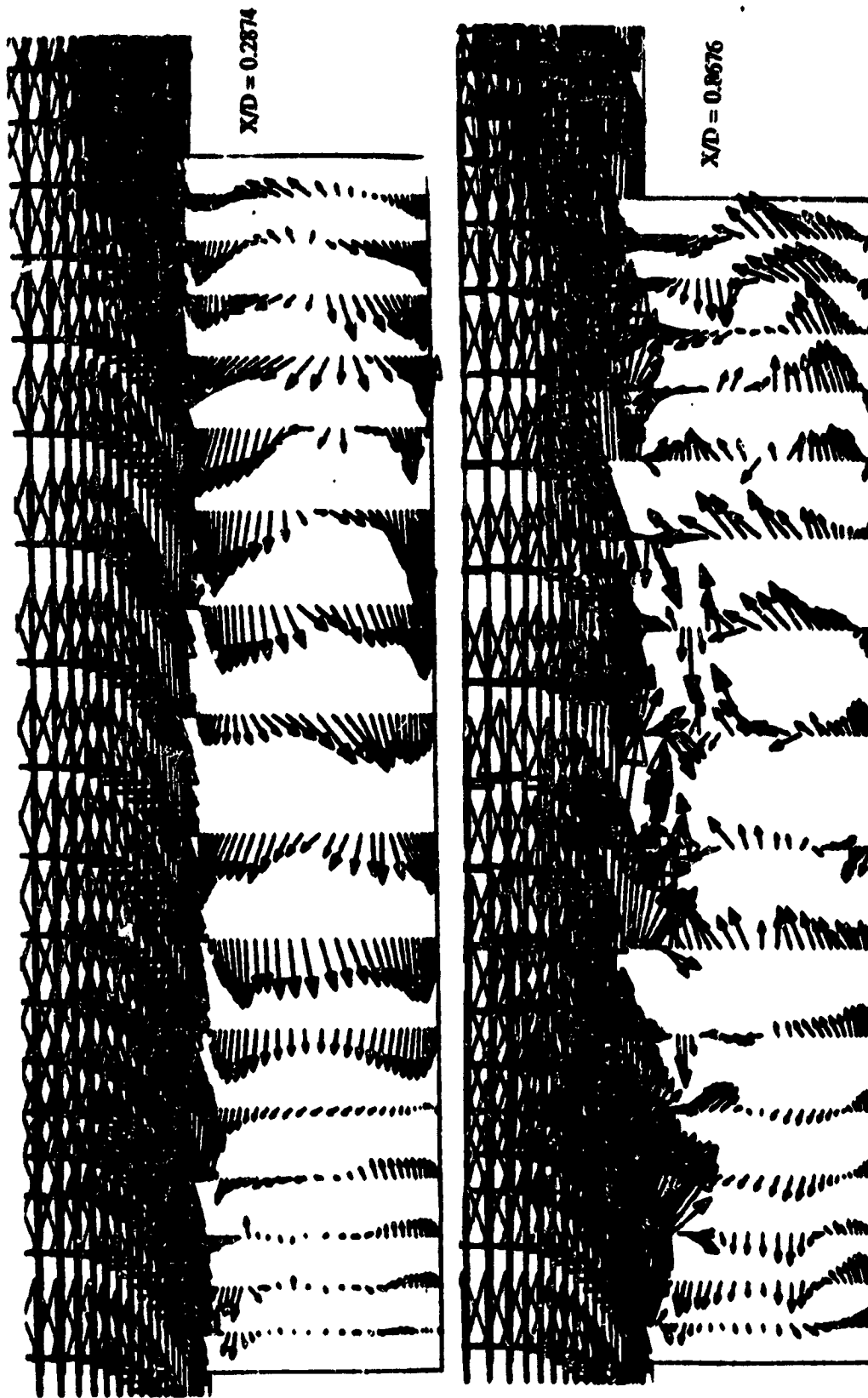
Fig. 5.12 Instantaneous velocity vectors at various cross flow planes
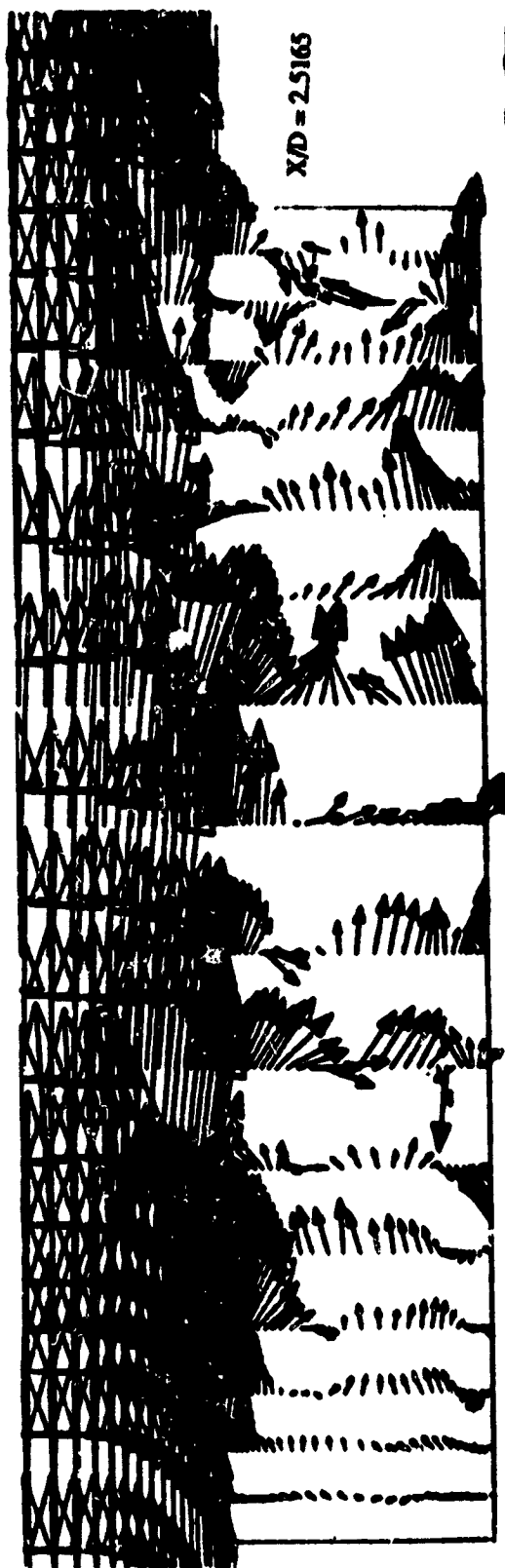
X/D = 2.5165

X/D = 2.9791

Fig.5.12 concluded

83

CONTOUR FROM .41E03 TO 1.0880
CONTOUR INTERVAL IS .50915E-01

X/D = 2.9391

CONTOUR FROM .38E03 TO 1.0882
CONTOUR INTERVAL IS .53392E-01

X/D = 2.5165

U_∞ 45°

CONTOUR FROM .41E03 TO 1.0820
CONTOUR INTERVAL IS .52211E-01

X/D = 0.8676
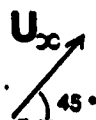
CONTOUR FROM .38E03 TO 1.0881
CONTOUR INTERVAL IS .56915E-01

X/D = 0.2874

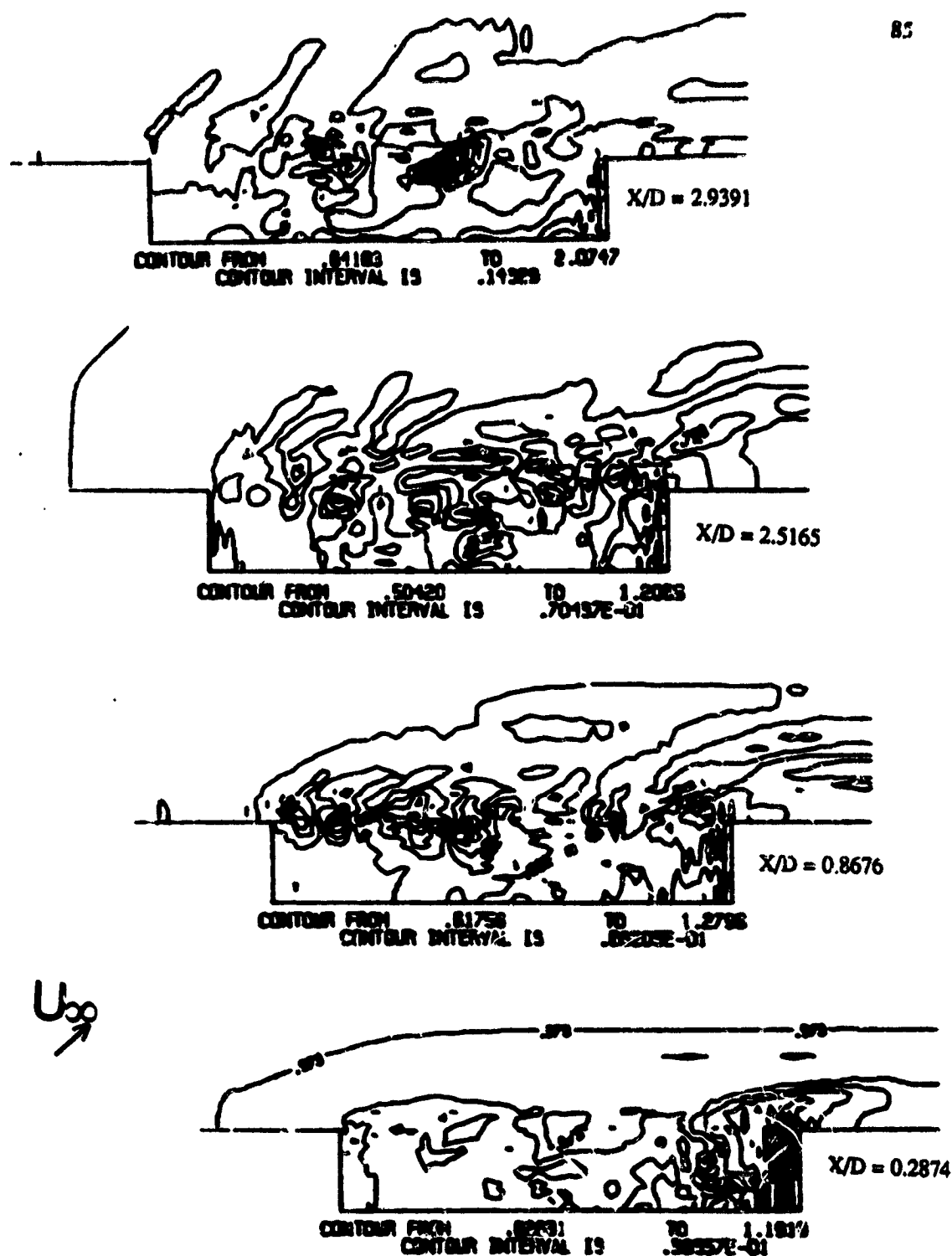Fig.5.13 Instantaneous density contours at various crossflow planes.

85

X/D = 2.9391

CONTOUR FROM .04183 TO 2.0747
CONTOUR INTERVAL IS .14326

X/D = 2.5165

CONTOUR FROM .50420 TO 1.2023
CONTOUR INTERVAL IS .70137E-01

X/D = 0.8676

CONTOUR FROM .61756 TO 1.2796
CONTOUR INTERVAL IS .65205E-01

U_∞

X/D = 0.2874

CONTOUR FROM .62281 TO 1.1919
CONTOUR INTERVAL IS .38537E-01

Fig. 5.14 Instantaneous pressure contours at various cross flow planes

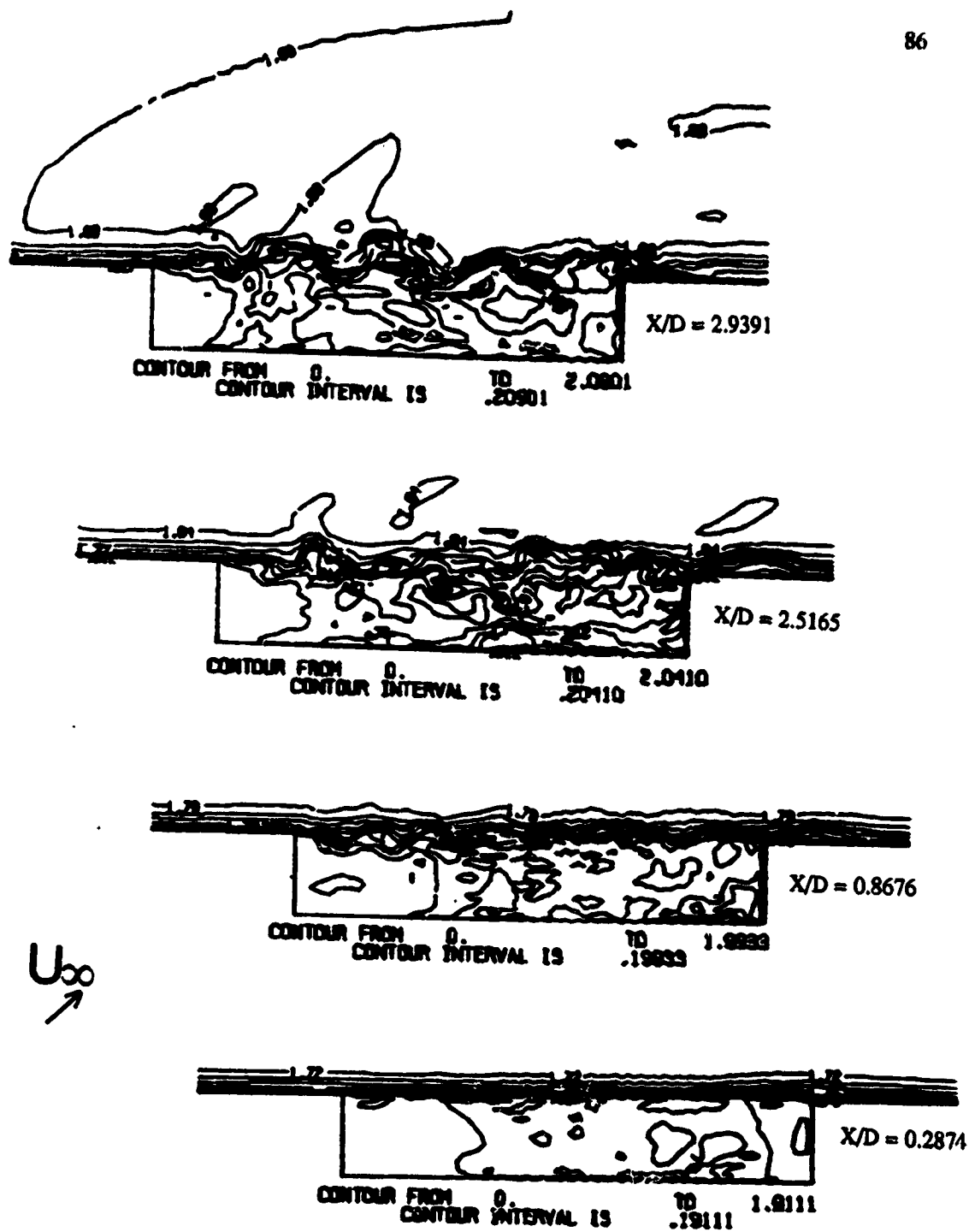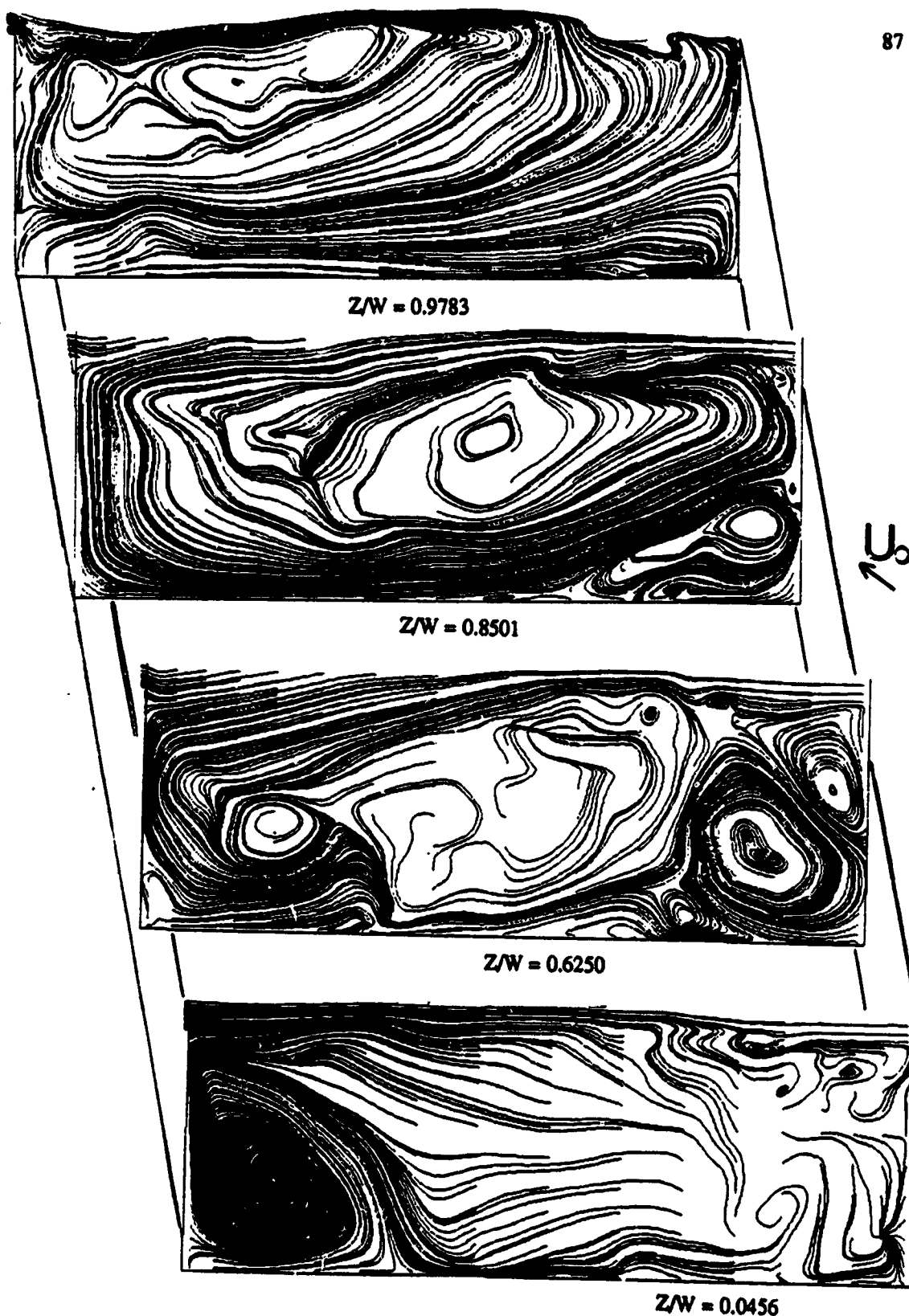Fig. 5.15 Instantaneous Mach number contours at various cross flow planes

Z/W = 0.9783

Z/W = 0.8501

U_∞

Z/W = 0.6250

Z/W = 0.0456

Fig. 5.16 Instantaneous streamlines at various spanwise planes

X/D=2.9391

X/D=2.5165

X/D=1.7998

U_∞

45°

X/D=0.8676

X/D=0.2874
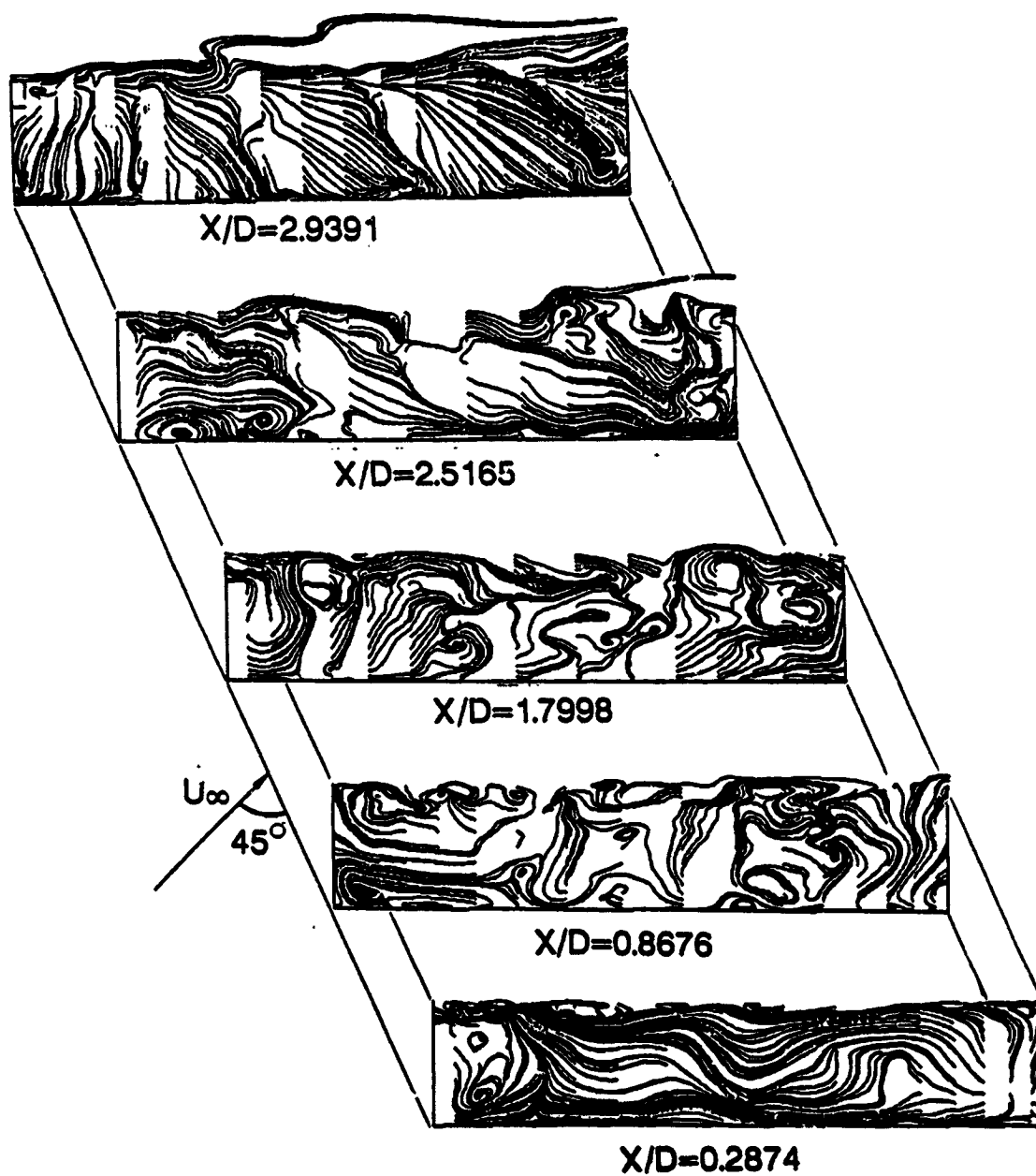
Fig.5.17 Instantaneous streamlines at various crossflow planes
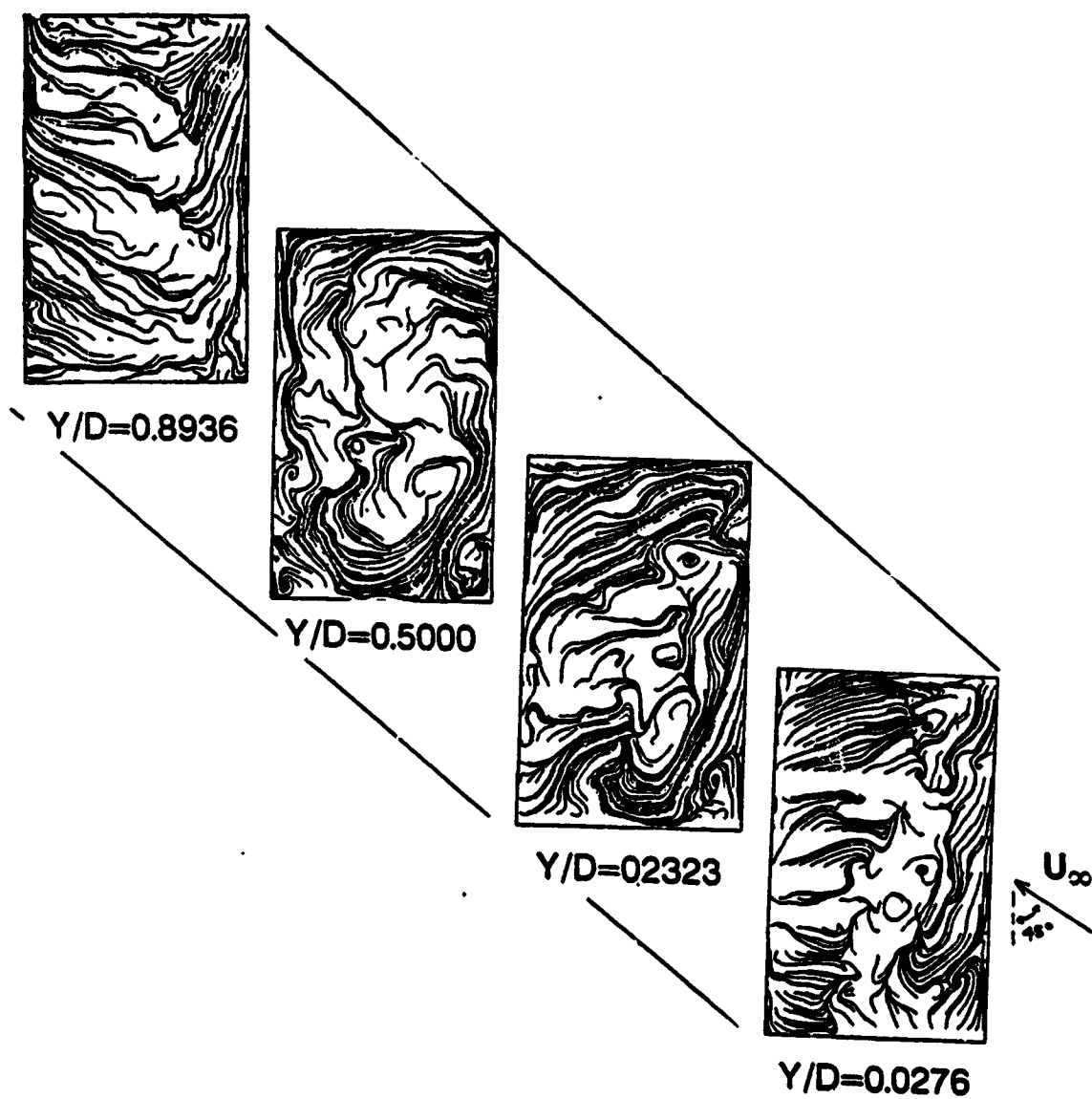
Y/D=0.8936

Y/D=0.5000

Y/D=02323

U_∞

Y/D=0.0276

Fig.5.18 Instantaneous streamlines at various horizontal planes
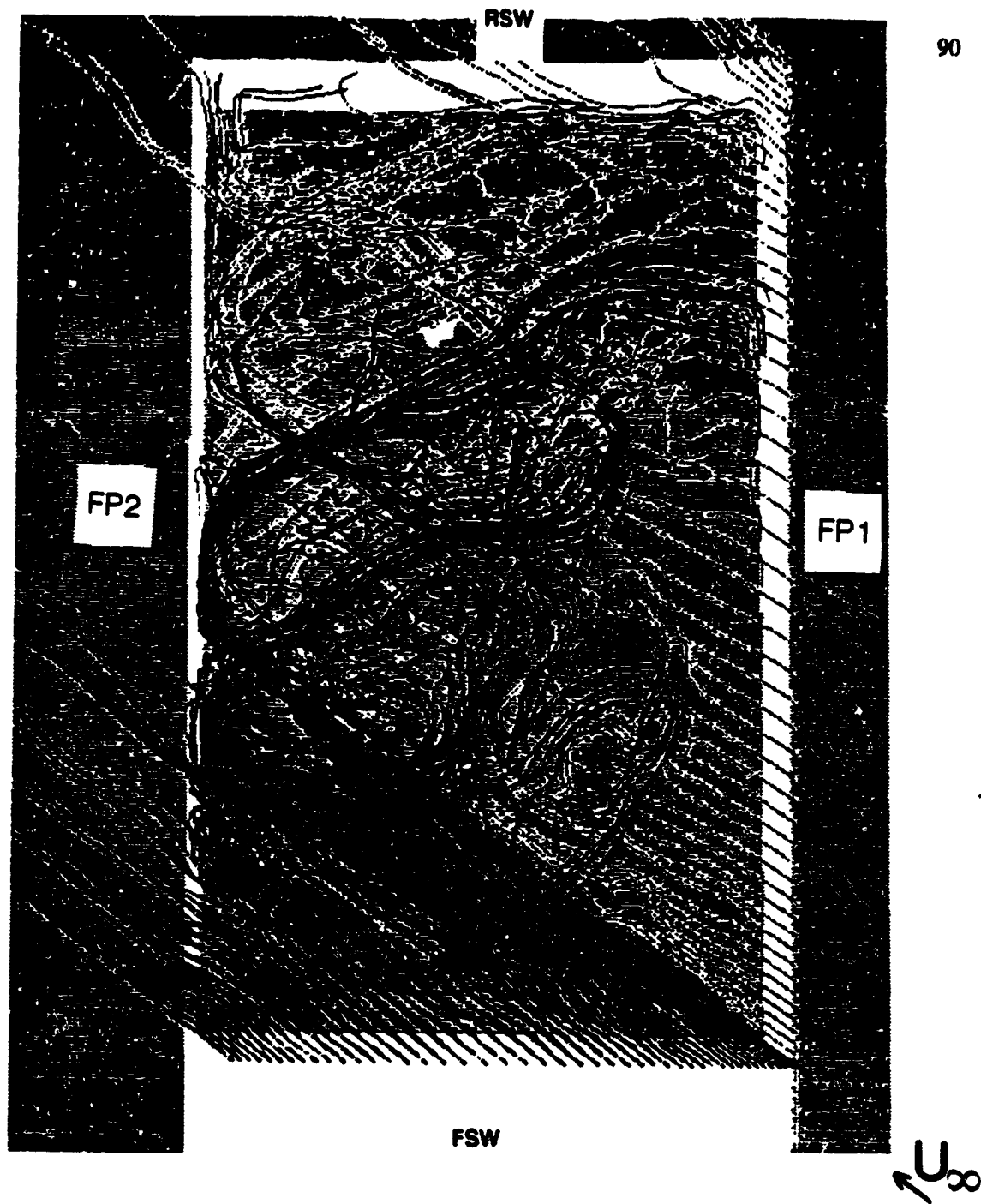
Fig. 5.19 Instantaneous Streamline pattern within the cavity

91
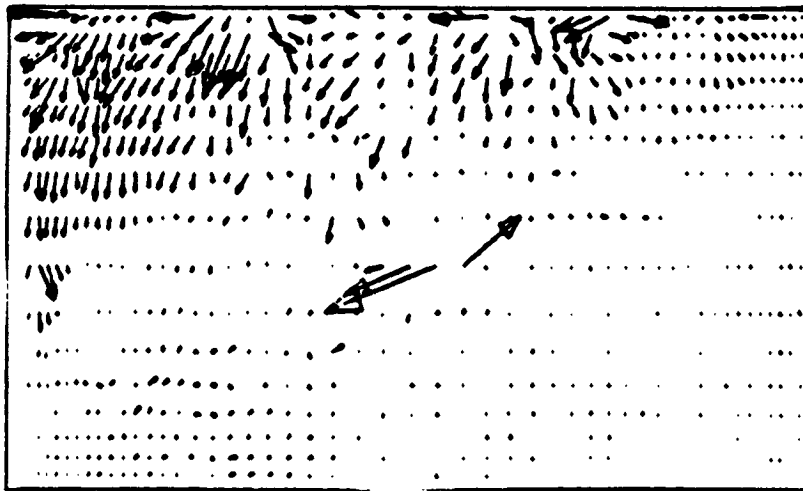
Fig. 5.20a Instantaneous shear stress vectors on the cavity floor.   Fig. 5.20b Instantaneous shear stress contours on the cavity floor.
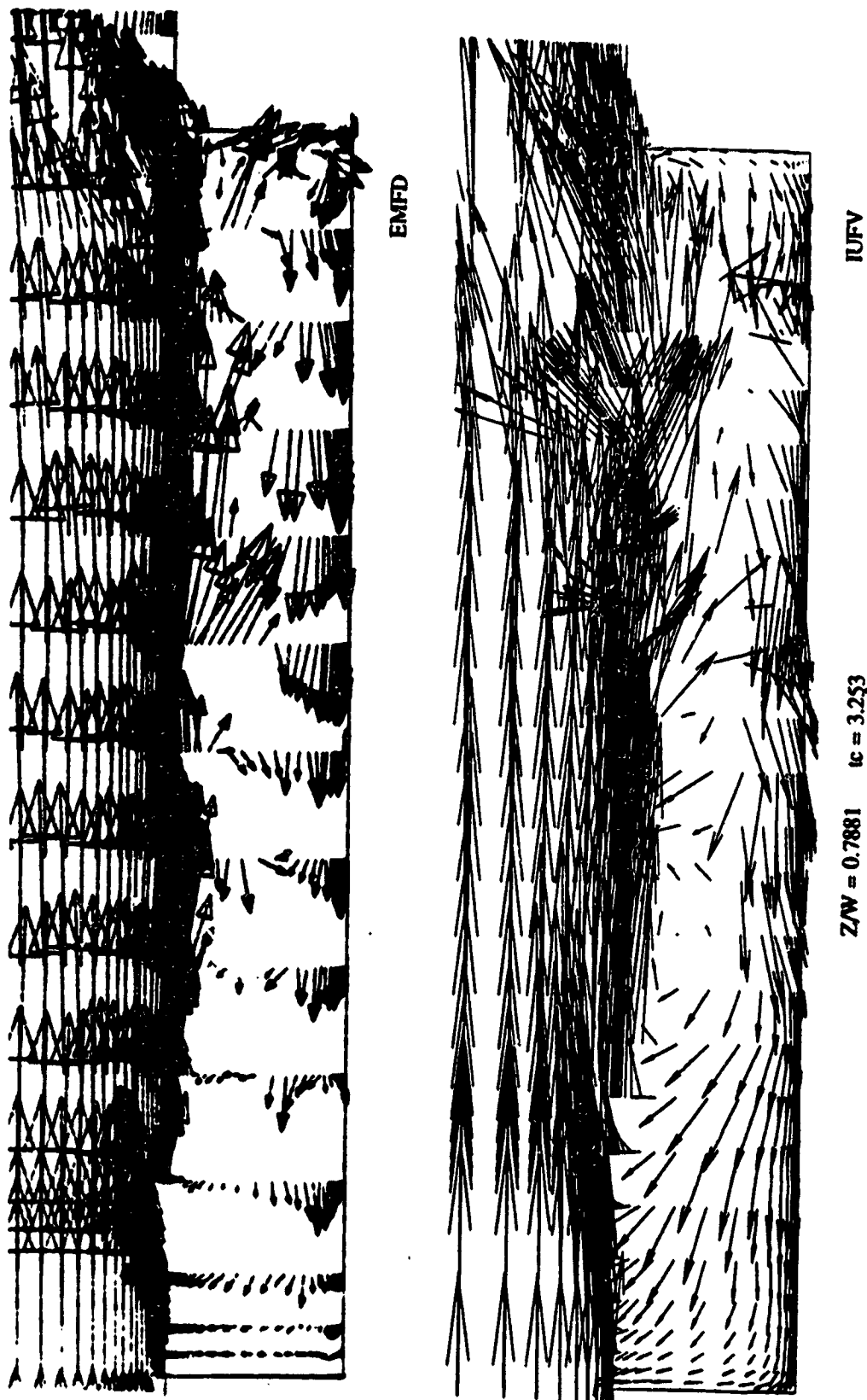
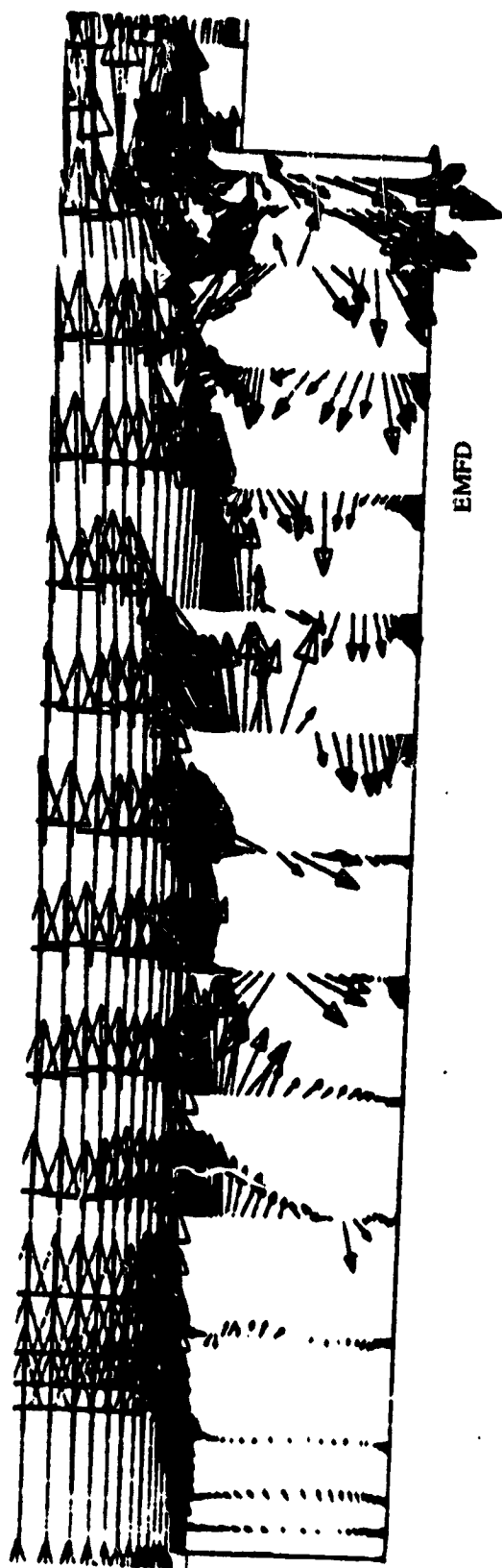EMFD

IUFV

Z/W = 0.7881   tc = 3.253

Fig. 5.21 Instantaneous velocity vectors at various spanwise planes.

EMFD

IUFV

Z/W = 0.9764   tc = 3.253

Fig.5.21 concluded

Fig. 5.22 Instantaneous density contours at various spanwise planes.

$Z/W = 0.7881$

$Z/W = 0.9764$

tc = 3.253

IUFV

EMFD

U_∞

Fig. 5.23 Instantaneous Mach number contours at various spanwise planes

Z/W = 0.7881

Z/W = 0.9764

tc = 3.253

IUFV

EMFD

95

U_∞ ↓

Z/W = 0.9509

Z/W = 0.7327

Z/W = 0.6027

Z/W = 0.3486

t = 3.233

ILFV

EMPD

Fig. 5.24 Instantaneous streamlines at various spanwise planes.

$U_\infty \downarrow$

EMFD

IUFV

Fig.5.25 Limiting streamlines on the cavity fl oor.

EMFD

Z/W = 0.4857   tc = 12.875

Fig. 5.26 Instantaneous velocity vectors at vari... spanwise planes.

EMFD

IUFV
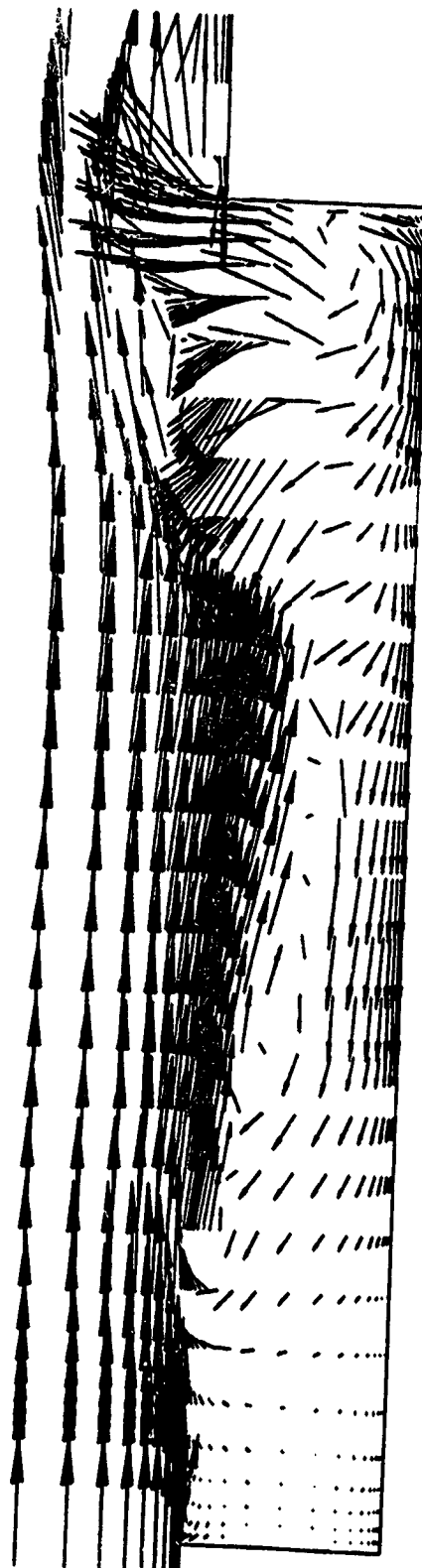
Z/W = 0.7881   tc = 3.253
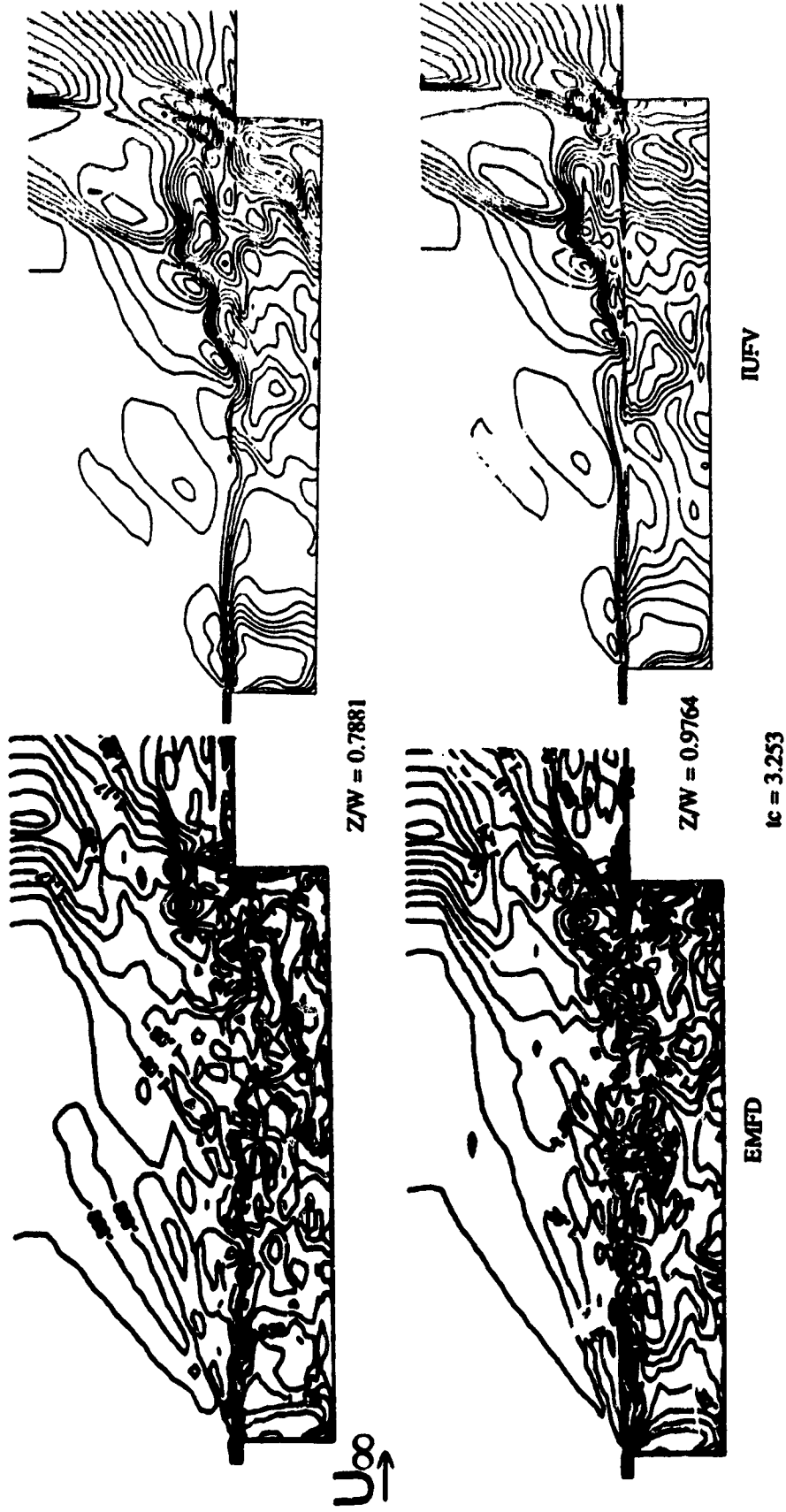
Fig.5.26 concluded
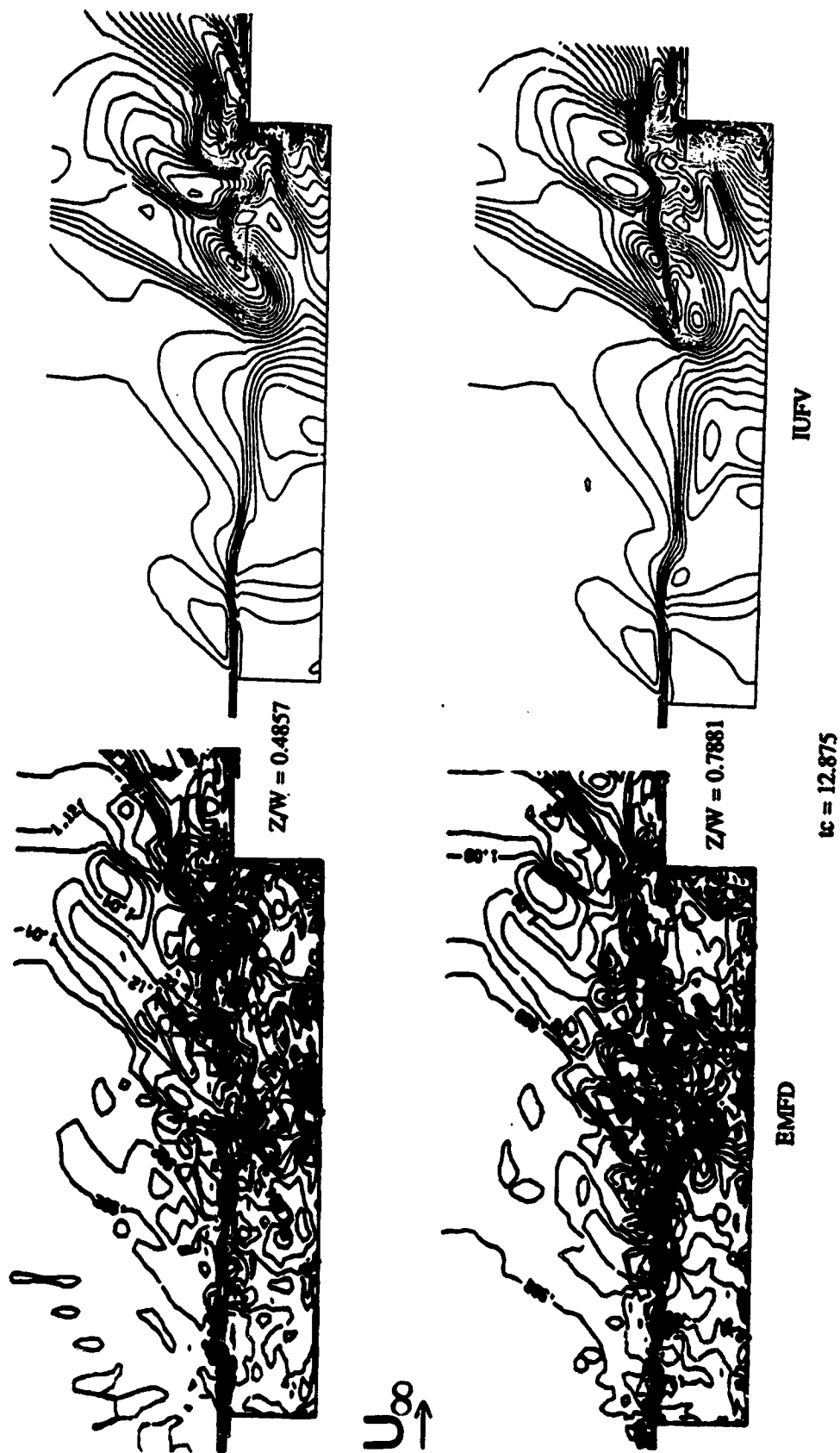
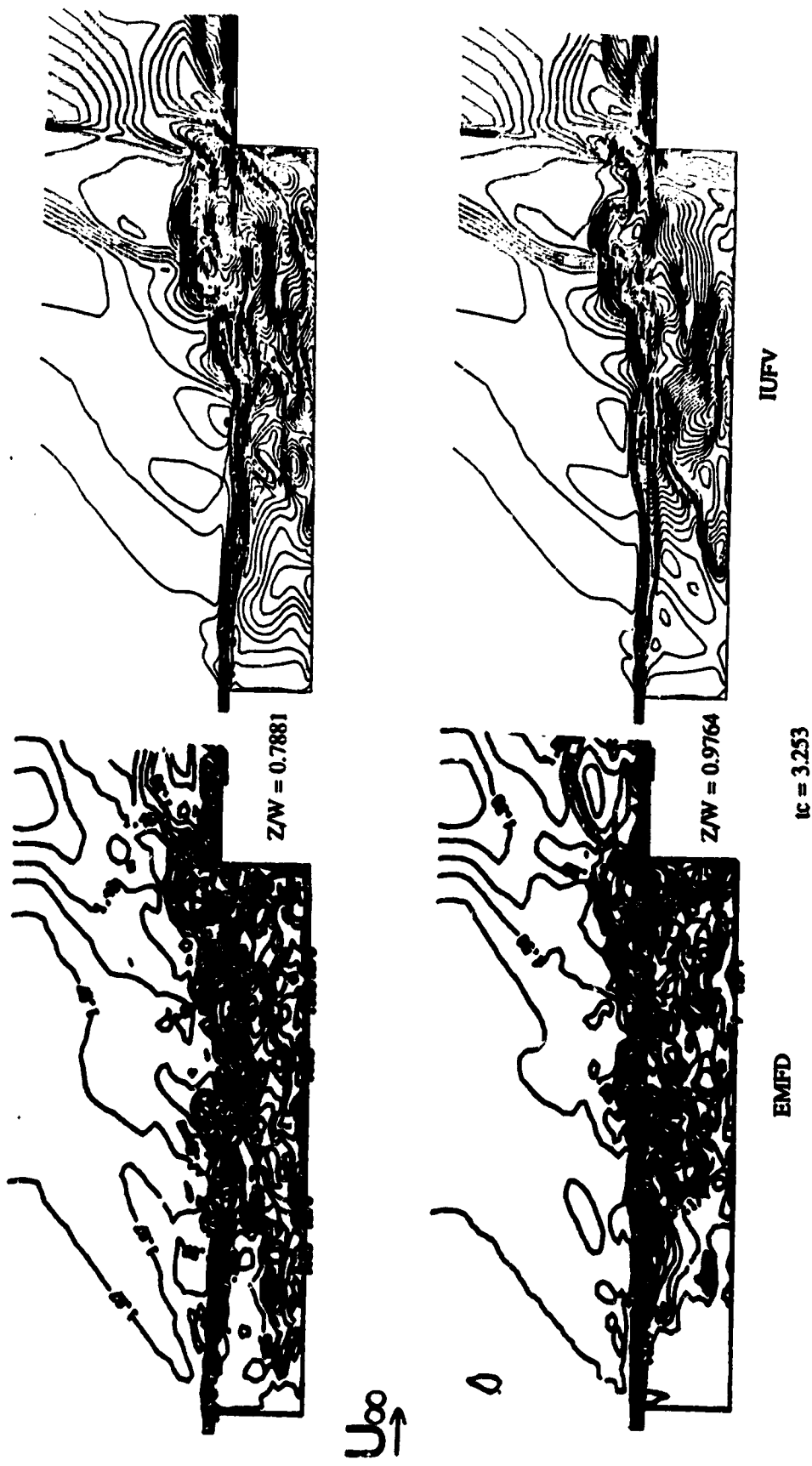Fig. 5.27 Instantaneous density contours at various spanwise planes

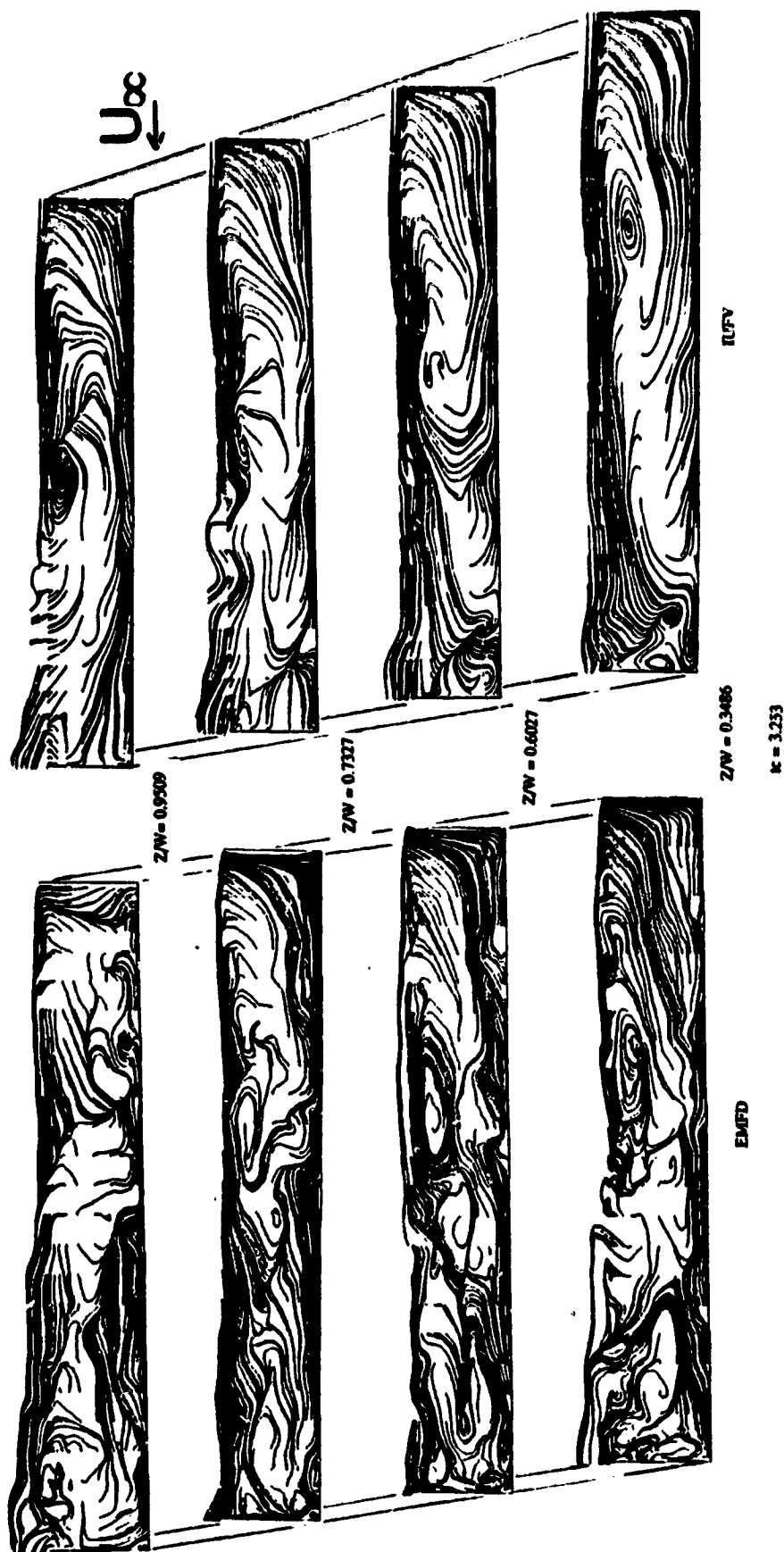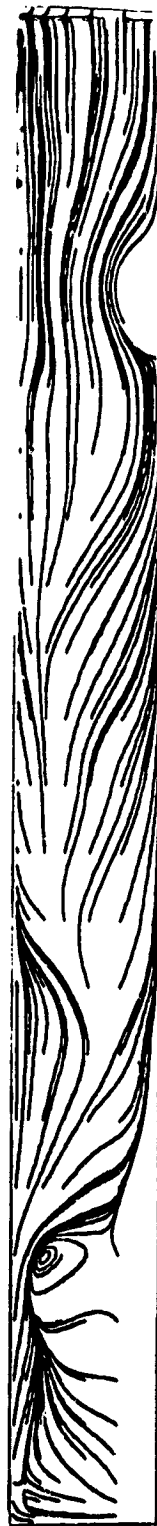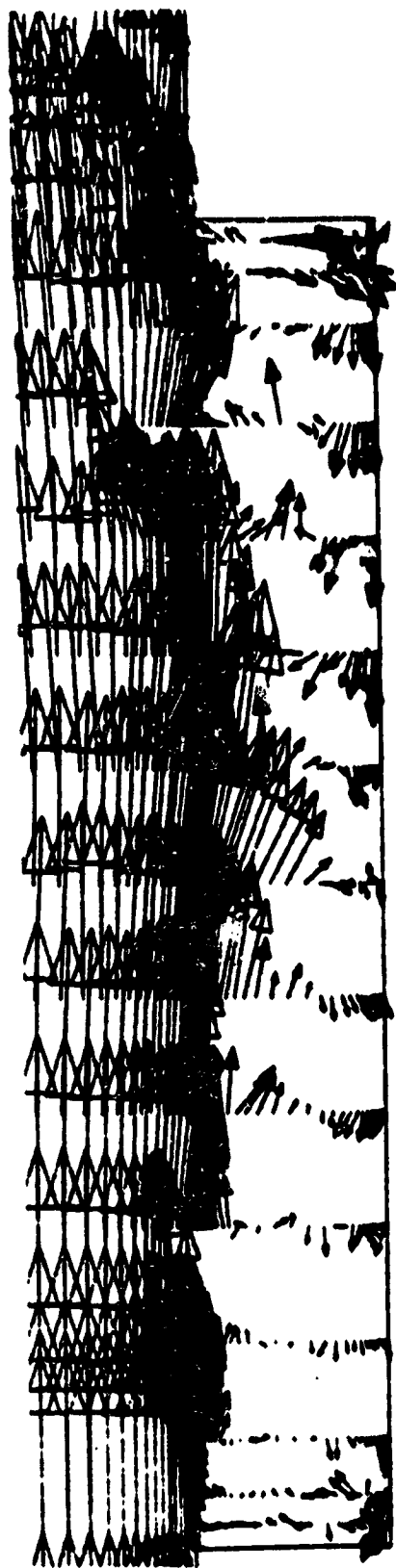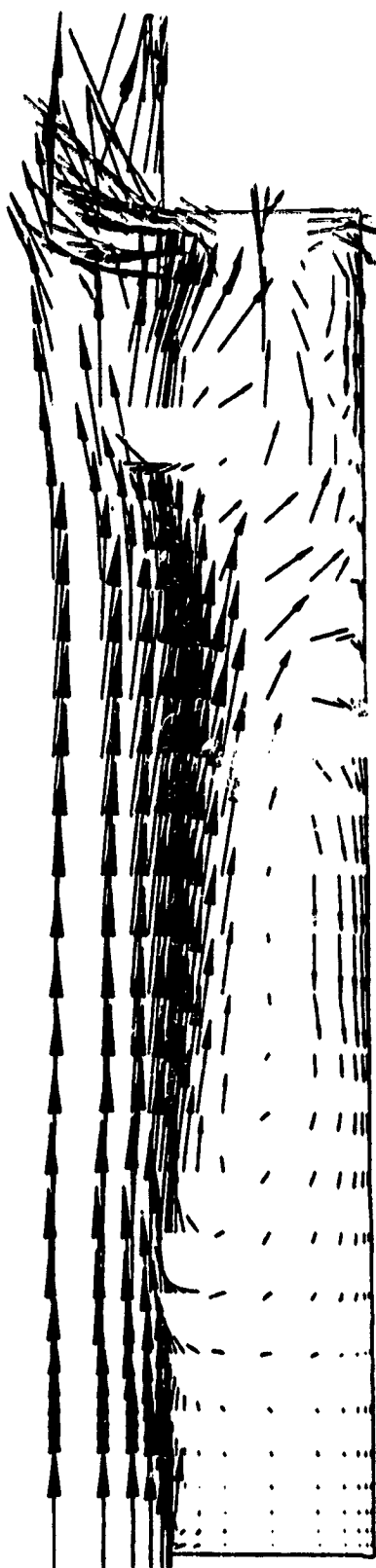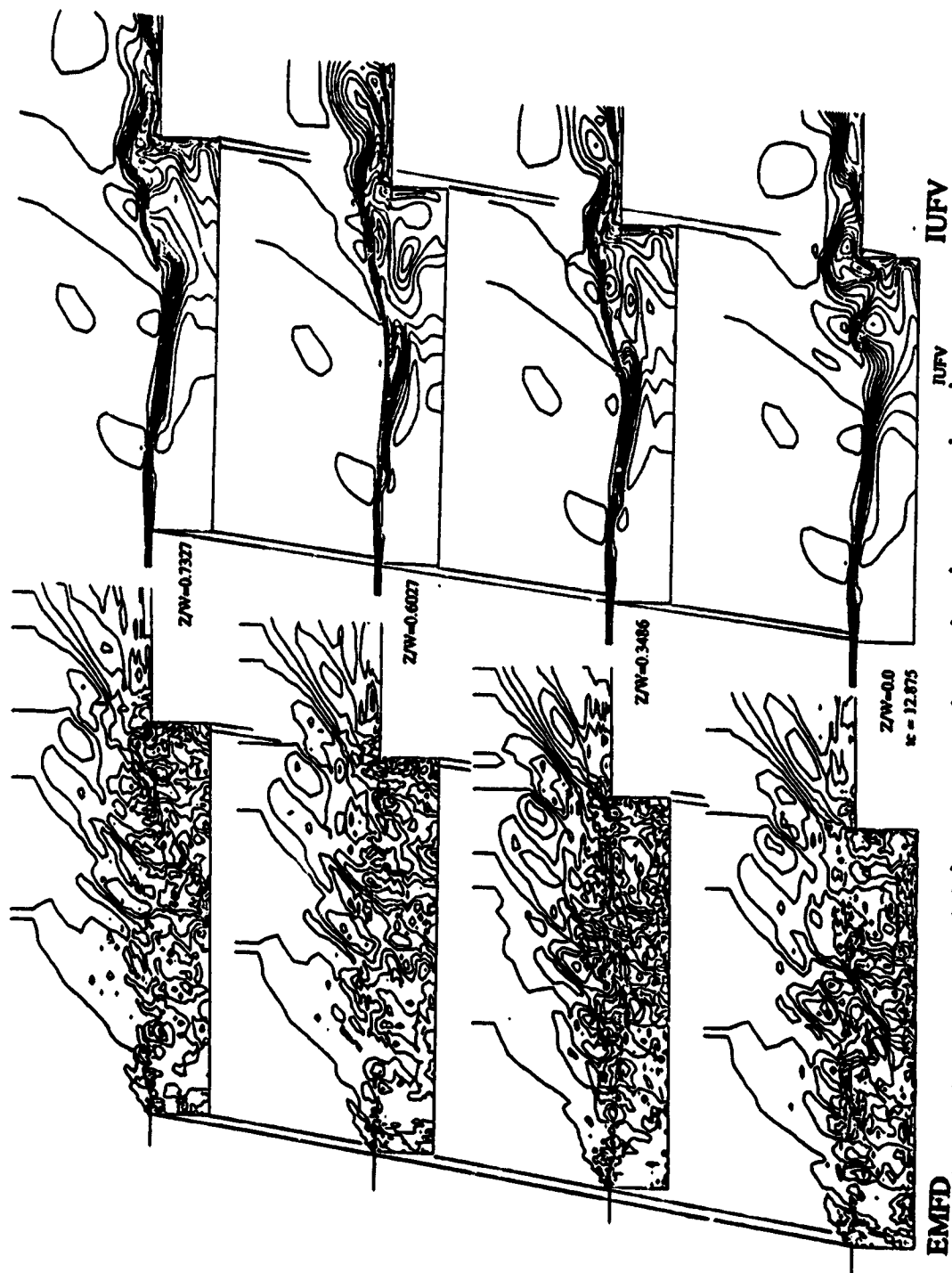Fig.5.26 Instantaneous total pressure contours at various spanwise planes
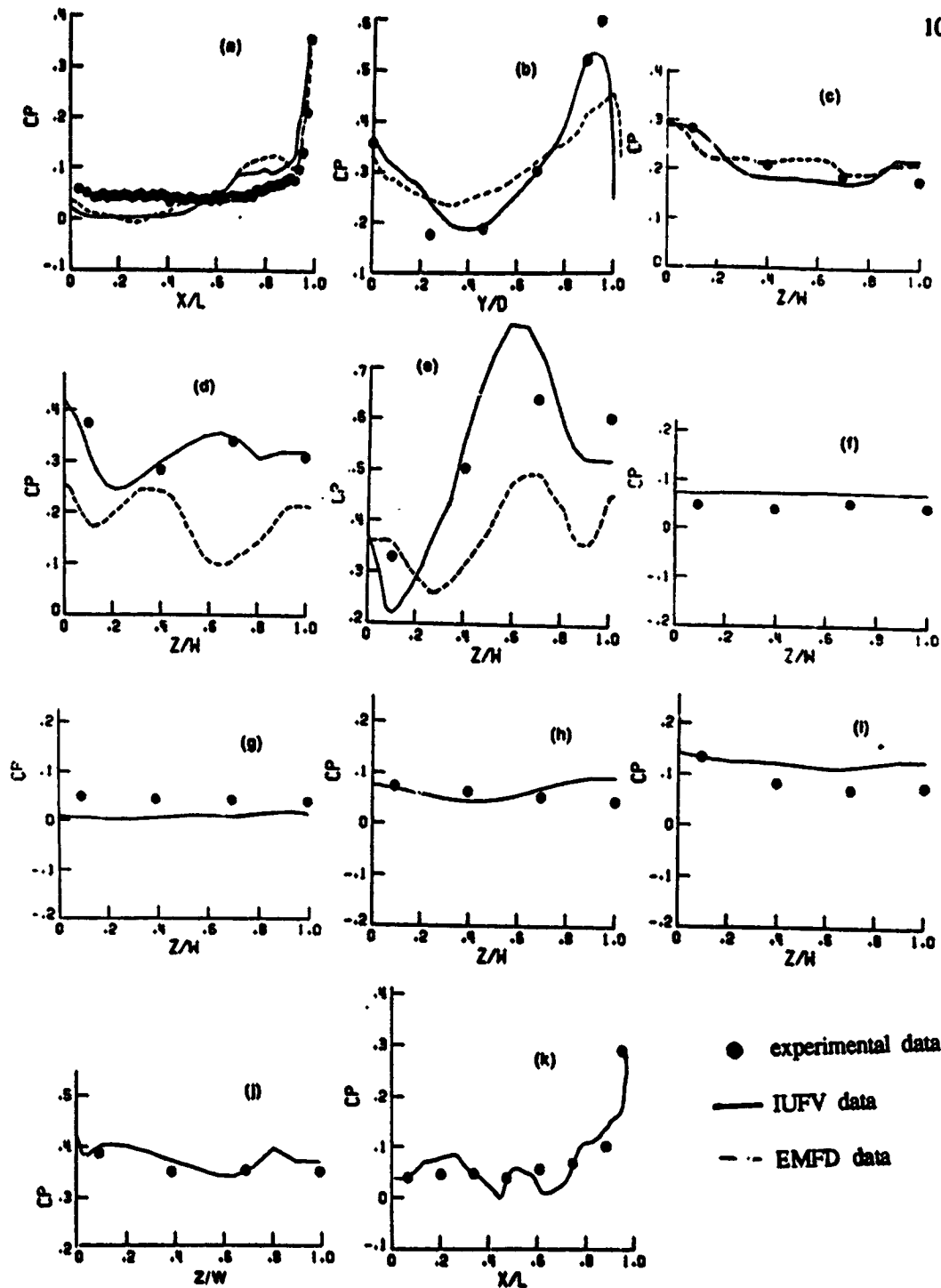
Fig.5.29. Mean pressure coefficient distribution on the cavity along the (a) centerline of cavity floor, (b) centerline of rear face, (c) crossflow line at Y/D = 0.24 on the rear face, (d) crossflow line at Y/D = 0.68 on the rear face, (e) crossflow line at Y/D = 0.94 on the rear face, (f) crossflow line at X/L = 0.204 on the floor, (g) crossflow line at X/L = 0.477 on the floor, (h) crossflow line at X/L = 0.75 on the floor, (i) crossflow line at X/L = 0.885 on the floor, (j) crossflow line at X/L = 0.988 on the floor, (k) longitudinal line at Y/D = 0.683 on the side wall.

Chapter 6

CONCLUSIONS AND RECOMMENDATIONS

Computational simulations of deep cavities in supersonic regimes have been performed. Two three-dimensional numerical models have been used to analyze the unsteady flow characteristics of cavity flows. The validity of the codes have been tested by analyzing turbulent flows past cavities. Computational simulations of the self induced oscillatory flows have been generated through time accurate solutions of the Reynolds averaged full Navier-Stokes equations. These governing equations have been solved by using an explicit, finite-difference method, and an implicit, finite-volume method. The Reynolds stresses have been modeled using the Baldwin-Lomax algebraic model with certain modifications. Time averaged and instantaneous results have been obtained, and quantitative comparisons with experimental data have been made in terms of mean static pressure and frequency spectra within the cavity. Computational simulations of cavity flows are important, because parametric studies on three-dimensional cavity flows can be conducted with relative ease and the time dependent properties as well as time averaged values can be obtained. In addition, the flow structure within the cavity can be visualized computationally. These computational capabilities are meant to complement the experimental work in obtaining a more complete understanding of the flow features within the cavity.

Comparing the flow structures of Case 1 and Case 2, we can see the effect of yaw. When the yaw angle is zero, the length scale which determines the flow structure

103

is length-to-depth ratio. However, when the yaw angle is nonzero, there is no longer a single length scale for the flow. However, the general structure for L/D < 3 and W/D < 5, is still an open cavity flow. The dominant directions and inclinations of the vortices are dramatically different. The number of vortices are also very different from the zero-yaw flow.

The vortex shedding from the cavity opening is captured computationally. This is caused by the motion of the shear layer as it moves in and out of the cavity. Since this shedding is predicted by the numerical solutions from both codes, it is believed to be a physical phenomenon. It is also believed that this shedding influences the cavity acoustics significantly.

For the explicit code, the explicit addition of the artificial viscosity has the tendency to smear out the instantaneous pressure values in the cavity floor region. Therefore, a time accurate numerical scheme that is robust and capable of yielding good results without the addition of artificial viscosity, results in better time dependent results. The implicit upwind scheme, which is naturally dissipative, produces better time dependent data. In addition, clustering the grids near the points where the instantaneous pressures are picked, also yields better results.

Three-dimensional calculations are very expensive, because it takes a long computational time to get the results. Two-dimensional calculations of the cavity centerplane can be used to develop the cavity flow. When the cavity flow is fully developed (about two characteristic time), then the solution data for the centerplane can be treated as the new initial conditions for the three dimensional cavity. In Case 1, such a treatment can save 86% of CPU times and in Case 3 and 4 this treatment can save 80% of CPU seconds to develop the cavity flows.

The acoustic phenomena is a very important topic of cavity flows. The acoustic waves generate an additional 20 dB sound pressure level jump in the harmonic frequen-

cies. Although we attempted the acoustic analyses of our results for Cases 2-4, they have not been completed. An extension of this work should complete this analysis.

Quantitative comparison with experimental data have been made in terms of mean static pressure and acoustic frequency spectra within the cavity. While most of this comparison is favorable, the numerical solution of Case 1 appears to underpredict the amplitude of the harmonic frequencies. This may be attributed to "too much viscosity" due to numerical damping and the eddy viscosity, that alters the pressure oscillations. A further study using improved numerical damping and eddy viscosity is needed.

It is also recommended that the temperature distributions, which are computed herein, are evaluated to show the heat transfer characteristics in a cavity. This is particularly important for high speed flows.

It is realized that a better comparison of the two schemes can be obtained if both codes were run on the same computers. A further study should be conducted with this consideration.

REFERENCES

1. Karamcheti, K., "Sound Radiation from Rectangular Cutouts," NACA-TN-3487, Aug. 1955.

2. Roshko, A., "Some Measurements of Flow in a Rectangular Cutout," NACA-TN-3488, Aug. 1955.

3. Suhs, N. E., "Computations of 3-D Cavity Flow at Subsonic and Supersonic Mach Numbers," AIAA Paper 87-1208, June 1987.

4. Baysal, O., Srinivasan, S., Stallings, R. L., Jr., "Unsteady Viscous Calculations of Supersonic Flows Past Deep and Shallow 3-D Cavities," AIAA Paper 88-0101, Jan. 1988.

5. Gorski, J. J., Ota, D. K., Chakravarthy, S. R., "Calculation of 3-D Cavity Flow Field," AIAA Paper No. 87-0117, Jan. 1987.

6. MacDearmon, R. W., "Investigation of the Flow in a Rectangular Cavity in a Flat Plate at a Mach Number of 3.55," NASA TN D-523, Sept. 1960.

7. Plumblee, H. E., Gibson, J. S., Lassiter, L. W., "A Theoretical and Experimen tal Investigation of the Acoustic Response of Cavities in a Aerodynamic Flow," WADD-TR-61-75, March 1962.

8. East, L. F., "Aerodynamically Induced Resonance in Rectangular Cavities," Journal of Sound and Vibration, 3(3), pp. 277-287, 1966.

9. Rossiter, J. E., " Wind Tunnel Experiments on the Flow over Rectangular Cavities at Subsonic and Transonic Speeds," Royal Aircraft Establishment ARC R&M 3438, 1966.

10. Spee, B. M., "Wind Tunnel Experiments on Unsteady Cavity Flows at High Subsonic Speeds," AGARD CP No. 4, pp. 947-974, May 1966.

11. McGregor, O. W. and White, R. A., "Drag of Rectangular Cavities in Supersonic and Transonic Flow Including the Effects of Cavity Resonance," AIAA Journal, Vol. 8, No. 11, Nov. 1970.

12. Heller, H. H., Holmes, D. G., Covert, E. E., "Flow-Induced Pressure Oscillations in Shallow Cavities," Journal of Sound and Vibration, 18(4), pp. 545-553, 1971.

13. Stalling, R. L. and Wilcox, F. J., "Experimental Cavity Pressure Distributions at Supersonic Speeds," NASA-TP-2683.

14. Heller, H. H. and Bliss, D. B., "Aerodynamically Induced Pressure Oscillations in Cavities-Physical Mechanisms and Suppression Concepts," AFFDL-TR-74-133, Feb. 1975.

15. Shaw, L. L., "Supersonic Flow Induced Cavity Acoustics," Shock and Vibration Bulletin, Part 2, Aug. 1986.

16. Weiss, R. F. and Florsheim, B. H., "Flow in a Cavity at low Reynolds Number," Physics of Fluids, Vol. 8, No. 9, Sept. 1965.

17. Pan, F. and Acrivos, A., "Steady Flows in Rectangular Cavities," Journal of Fluid Mechanics, Vol. 28, Part 4, pp. 643-655, 1967.

18. Mehta, U. B. and Lavan, Z., "Flow in a 2-D Channel with a Rectangular Cavity," NASA-CR-1245, Jan. 1969.

19. O'Brien, V., "Closed Streamlines Associated with Channel Flow over a Cavity," Physics of Fluids, Vol. 15, No. 12, Dec. 1972.

20. Nallaswamy, M. and Krishnaprasad, K., "On Cavity Flows at High Reynolds Number," Journal of Fluid Mechanics, Vol. 79, No. 2, pp. 391-414, Feb. 1977.

21. Bilanin, A. J. and Covert, E. E., "Estimation of Possible Excitation Frequencies for Shallow Rectangular Cavities," AIAA Journal, Vol. 11, No. 3, March 1973.

22. Smith, D. L. and Shaw, L. L., "Prediction of the Pressure Oscillations in Cavities Exposed to Aerodynamic Flow," AFFDL-TR-75-34, Oct. 1975.

23. Block, P. J. W., "Noise Response of Cavities of Varying Dimensions at Subsonic Speeds," NASA TN-D-8351, Dec. 1976.

24. Hardin, J. C. and Mason, J. P., "Broad Band Noise Generation by a Vortex Model of a Cavity Flow," AIAA Journal, Vol. 15, No. 5, pp. 632-637, May 1977.

25. Borland, C. J., "Numerical Prediction of the Unsteady Flowfield in an Open Cavity," AIAA Paper No. 77-673, 1977.

26. Hankey, W. L. and Shang, J. S., "Analyses of Pressure Oscillations in an Open Cavity," AIAA Journal, Vol. 18, No. 8, pp. 892-898, Aug. 1980.

27. Brandeis, J., "Flow Separation in Shear-Layer-Driven Cavities," AIAA Journal, Vol. 20, No. 7, pp. 908-914, July 1982.

28. Shaw, L. L., Bartel, and McAvoy, "Prediction and Suppression of the Acoustic Environment in Large Enclosures with Small Openings," AIAA Paper No. 82-0121, Jan. 1982.

29. Parthasarathy, S. P., Cho, Y. I., and Back, L. H., "Aerodynamic Sound Generation Induced by Flow over Small Cylindrical Cavities," AIAA Paper No. 84-2258, Oct. 1984.

30. Baysal, O. and Stallings, R. L., Jr., "Computational and Experimental Investigations of Cavity Flowfields," AIAA Paper 87-0114, Jan. 1987.

31. Rizzeta, D. P., "Numerical Simulation of Supersonic Flow over a Three-Dimensional Cavity," AIAA Paper 87-1288, June 1987.

32. Baysal, O., Srinivasan, S., and Stalling, R. ., Jr., "Unsteady Viscous Calculations of Supersonic Flows Past Deep and Shallow 3-D Cavities," AIAA-88-0101, Jan 1988.

33. Suhs, N. E. and Jordan, J. K., "Three-Dimensional Cavity Flow Computations at Transonic Mach Numbers," AEDC-TR-88-30, Feb. 1989.

34. Baysal, O. and Srinivasan, S., "Navier-Stokes Calculations of Transonic Flows Past Cavities," NASA-CR-4210, Jan. 1989.

35. Deepak Om, "Navier-Stokes Simulation for Flow Past an Open Cavity," Journal of Aircraft, Vol. 25, No. 9, pp. 842-848, Sep. 1988.

36. Baysal, O. and Srinivasan, S., "Calculation of Wall and Free Turbulent-Shear Flows at Supersonic Speeds," ASME-FED, Vol. 51, June 1987.

37. Komerath, N. M., Ahuja, K. K., Chambers, F. W., "Prediction and Measurement of Flows over Cavities - A Survey," AIAA-87-0166, Jan. 1987.

38. Anderson, D. A., Tannehill, J. C., Pletcher, R. H., Computational Fluid Mechanics and Heat Transfer, pp. 255, McGraw-Hill Book Company, New York, 1984.

39. Cebeci, T., "Calculation of Turbulent Boundary Layers with Heat and Mass Transfer," AIAA Paper 70-741, Jan. 1970.

40. Baldwin, B. S. and Lomax, H., "Thin-Layer Approximation and Algebraic Model for Separated Turbulent Flows," AIAA Paper 78-257, Jan. 1978.

41. Degani, D. and Schiff, L. B., "Computation of Turbulent Supersonic Flows around Pointed Bodies Having Crossflow Separation," Journal of Computational Physics, No. 1, Sept. 1986.

42. Waskiewicz, J. D., Shang, J. S., and Hankey, W. L., "Numerical Simulation of Near Wakes Utilizing a Relaxation Turbulence Model," AIAA Journal, Vol. 18, No. 12.

43. Julius, E. H. and Blanchard, D. K., "Computer Program for Solving Laminar, Transitional, or Turbulent Compressible Boundary Layer Equations for Two-Dimensional and Axisymmetric Flow," NASA-TM-83207, 1982.

44. MacCormack, R. W., "Numerical Solution of the Interaction of a Shock Wave with a Laminar Boundary Layer," Proceedings of the Second International Conference on Numerical Methods in Fluid Dynamics, May 1970.

45. MacCormack, R. W. and Baldwin, B. S., "An Numerical Method for Solving the Navier-Stokes Equations with Application to Shock Boundary Layer Interactions," AIAA Paper 75-1, July 1975.

46. Kumar, A., "A Numerical Method for Solving the Equations of Compressible Viscous Flow," AIAA Paper 81-0100, Jan. 1981.

47. Block, P. J. W., "Noise Response of Cavities of Varying Dimensions at Subsonic Speeds," NASA-TN-D-8351, Dec. 1976.

48. Steger, J. L. and Warming, R. F., "Flux-Vector Splitting of the inviscid Gasdynamic Equations with Application to Finite-Difference Methods", Journal of Computational Physics Vol. 40, No. 2, April 1981.

49. Beam, R. M. and Warming, R. F., "An Implicit Finite-Difference Algorithm for Hyperbolic System in Conservation-Law Form", Journal of Computational Physics, Vol. 22, No. 1, Sep 1976.

50. Warming, R. F. and Beam, R. M., "On the Construction and Application of Implicit Factored Schemes For Conservation Laws", SIAM-AMS Proceedings, Vol. 11, 1978.

51. Roe, P. L., "Characteristic-Based Scheme for The Euler Equations", Annual Review, Fluid Mechanics, Vol. 18, pp. 337-365, 1986.

52. Roe, P. L., "Approximate Riemann Solvers, Parameter Vectors, and Difference Schemes", Journal of Computational Physics 43, 1981.

53. Vatsa, V. N., Thomas, J. L., Wedan, B. W., "Navier-Stokes Computations of Prolate Spheroids at Angle of Attack", AIAA paper 87-2627-cp, Aug. 1987.

54. Van Leer, B., "Flux-Vector Splitting For the Euler Equation", ICASE Report, No.82-30, Sep. 1982.

55. Anderson, W. K., Thomas, J. L., Van Leer, B., "A Comparison of Finite Volume Flux Vector Splitting for the Euler Equations", AIAA Paper No.85-0122, 1985.

56. Anderson, W. K., Thomas, J. L., and Whitfield D. L., "Three-Dimensional Multigrid Algorithms for the Flux-Split Euler Equations", NASA TP 2829, Nov 1988.

57. Rumsey, C. L., Thomas, J. L., Warren, G. P., Liu, G. C., "Upwind Navier-Stokes Solutions for Separated Periodic Flows", AIAA-86-0247, Jan. 1986.

58. Thomas, J. L., Buning, P. G., Choi, D., Rogers, S. E., Bancroft, G., and Merrit, F. J., " Flow Visualization of CFL Using Graphics Workstations", AIAA Paper 87-1180, July 1987.

59. Buning, P. G. and Steger, J. L., "Graphics and Visualization Computational Fluid Dynamics", AIAA Paper 85-1507, June 1985.

60. Hardin, J. C., "Introduction to Time Series Analysis", NASA-RP-1145, March 1986.

61. Temkin, S., "Elements of Acoustics", pp. 58-64, McGraw Hill, New York, 1981.

62. Beranek, L. L., "Noise and Vibration Control", McGraw Hill, New York, 1971, pp.42-43.

63. Shivakumar Srinivasan, "Numerical Simulation of Turbulent Flows Past three Dimensional Cavities", Ph. D. dissertation, pp.29, Old Dominion University, Aug. 1988.

64. McDonald, H. and Briley, W. R., "Three-Dimensional Supersonic Flow of a Viscous or Inviscid Gas", J. Comp. Phys., vol. 19, pp. 150-178, 1975.

BIOGRAPHY

This author was born on February 20, 1961 in Taipei, Taiwan. He received his Bachelor's degree in Aeronautical Engineering from National Cheng Kung University, Taiwan, in June, 1984. He came to the United States of America in August, 1984 to pursue higher education. He began his graduate study in Mechanical Engineering Department of Old Dominion University. The author was involved in research work pertaining to applied CFD, at NASA Langley Research Center.